Solids, liquids, and gases under high pressure

Ho-Kwang Mao

Center for High Pressure Science and Technology Advanced Research, Shanghai 201203, China
and Geophysical Laboratory, Carnegie Institution, Washington, D.C. 20015, USA

Xiao-Jia Chen and Yang Ding

Center for High Pressure Science and Technology Advanced Research, Shanghai 201203, China

Bing Li[*]

Center for the Study of Matter at Extreme Conditions, Florida International University, Miami, Florida 33199, USA
and Department of Mechanical and Materials Engineering, Florida International University, Miami, Florida 33199, USA

Lin Wang[†]

Center for High Pressure Science and Technology Advanced Research, Shanghai 201203, China

(published 20 March 2018)

Pressure has long been recognized as a fundamental thermodynamic variable but its application was previously limited by the available pressure vessels and probes. The development of megabar diamond anvil cells and a battery of associated in-laboratory and synchrotron techniques at the turn of the century have opened a vast new window of opportunities. With the addition of the pressure dimension, we are facing a new world with an order of magnitude more materials to be discovered than all that have been explored at ambient pressure. Pressure drastically and categorically alters all elastic, electronic, magnetic, structural, and chemical properties, and pushes materials across conventional barriers between insulators and superconductors, amorphous and crystalline solids, ionic and covalent compounds, vigorously reactive and inert chemicals, etc. In the process, it reveals surprising high-pressure physics and chemistry and creates novel materials. This review describes the principles and methodology used to reach ultrahigh static pressure: the *in situ* probes, the physical phenomena to be investigated, the long-pursued goals, the surprising discoveries, and the vast potential opportunities. Exciting examples include the quest for metallic hydrogen, the record-breaking superconducting temperature of 203 K in H_nS, the complication of "free-electron gas" alkali metals, the magnetic collapse in 3*d* transition elements, the pressure-induced superconductivity from topological insulators, the novel stoichiometry in simple compounds, the interaction of nanoscience, the accomplishment of 750 GPa pressure, etc. These highlights are the integral results of technological achievements, specific measurements, and theoretical advancement; therefore, the same highlights will appear in different sections corresponding to these different aspects. Overall, this review demonstrates that high-pressure research is a new dimension in condensed-matter physics.

DOI: 10.1103/RevModPhys.90.015007

CONTENTS

[*]bingli.001@gmail.com
[†]wanglin@hpstar.ac.cn

I. INTRODUCTION

Pressure *P* categorically alters all states of matter, but for years our knowledge of *P* lagged behind other variables such as temperature *T*. This was due to two constraints: a static megabar (100 GPa) *P* range was unattainable, and the properties of the compressed sample could not be measured inside the high-*P* vessels. The invention of the beveled diamond anvil cell (DAC) (Mao and Bell, 1978; Jayaraman, 1983) coupled with modern micronano probing technology (Wang, Ding *et al.*, 2010; Yang *et al.*, 2013) has overcome these constraints and enabled unequivocal characterization of dense matters beyond three megabar *P* (Mao *et al.*, 1989; Dubrovinsky *et al.*, 2012, 2015; Zha *et al.*, 2014)—an order of magnitude higher than the previous maximum set by the pioneering high-*P* work of Nobel Physics Laureate, Percy W. Bridgman (1935).

Breaking the megabar *P* barrier is often compared with reaching the liquid helium *T*, except the impacts of *P* are conceivably greater than *T* on three counts. First, all materials undergo changes at high *P*, while low-*T* phenomena such as superconductivity, superfluidity, and Bose-Einstein condensation are limited to specific materials. Second, low *T* is limited by the absolute zero, while high *P* is boundless. Third, adding *P* to the *T* dimension results in the multiplication of *P* and *T* which greatly expands the materials base and novel phenomena. For instance, the three phases of H_2O in the *T* dimension expand to >30 phases of stable and metastable ices in the multimegabar *P-T* space, and each phase has its uniquely interesting properties (see, for example, Goncharov *et al.*, 1996; Struzhkin, Goncharov *et al.*, 1997; Chou *et al.*, 1998;

Cai *et al.*, 2005; Y. Wang *et al.*, 2011). Such multiplicities have been observed in many simple systems, e.g., H_2, Li, C, N_2, O_2, Na, Ca, Si, S, Ge, Se, and Te, covering the entire Periodic Table's elements and their compounds. At every P interval, moving from the ordinary condensed-matter to dense-matter physics, the wholesale properties of material change, unexpected physical phenomena occur, and a new physical world emerges. After all, the majority of substances in the Universe are actually under high P, and high-P discoveries are crucial for understanding the geophysics and astrophysics (Lobanov *et al.*, 2013) deep inside celestial bodies.

In this sense, high P should not be viewed as an extreme condition, but as an unexplored dimension. Consequently, our "ordinary" P world should be regarded as a special condition in the P dimension. The science and technology that have been developed for this "special condition" can now be used to explore the unknown physics in the vast overall P dimension and new knowledge gained at each segment of P advances the generalized rule of physics.

Although high P is a relatively new dimension, research is growing at an astonishing rate in multidisciplinary directions. In fact, it is fair to say that the high-P research domain may encompass all physical sciences at different P conditions. It is no longer feasible for the present review to cover the entire scope of static high-P physics. Instead, we will use examples of many recent exciting breakthroughs as common threads through different sections of high-P probes, materials properties, and novel phenomena to demonstrate the interplay of high-P science and technology and the great research opportunities available.

II. REACHING ULTRAHIGH P

A. Diamond anvil cell or diamond window cell

1. The principle of the DAC

The DAC is a unique apparatus capable of generating hundreds of GPa of ultrahigh static P and conducting a full range of *in situ* measurements. All DACs are the common key component of two opposing diamond anvils that generate P and provide transparent windows for optical and x-ray access.

Since the invention of the DAC in the 1950s (Bassett, 2009), numerous modifications and improvements have been applied to the diamond anvils (Mao and Bell, 1978), anvil-supporting seats (Boehler and De Hantsetters, 2004), sample-containing gaskets (Zou *et al.*, 2001; Funamori and Sato, 2008), DAC body (Bassett, 1979; Boehler, 2006; Boehler *et al.*, 2013), and compression mechanisms (Sinogeikin *et al.*, 2015) to optimize the P range, T range, P homogeneity, sample size, and accessibility for a great variety of diagnostic probes. The DAC has evolved to become the most powerful tool among all static high-P research apparatuses. It holds the highest static P record with the most versatile physical measurement capabilities.

The principle of the DAC design is simple: two opposing diamond anvils with small culets point to each other (Fig. 1). As P is defined by a force per unit area, using the hardest known material diamond as the anvils allow ultrahigh P generation on the sample, which is squeezed in between two small culets at the tip of the anvils.

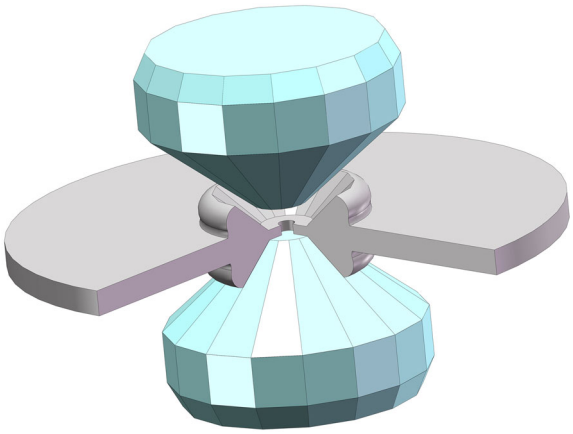

FIG. 1. Configuration of a pair of opposed diamond anvils squeezing the sample chamber to generate ultrahigh P. The sample chamber is a hole in the gasket that contains the sample and a P medium.

2. Diamond anvils

A single-crystal diamond is the chosen anvil material because of its many superior properties, including its unmatched extreme hardness to support high P, transparency to infrared, visible, and ultraviolet radiations (< 5 eV) for optical spectroscopy, transparency to x ray (> 10 keV) for x-ray diffraction, spectroscopy and imaging, chemical inertness, and compatibility for electrical and magnetic transport measurements. Because of the exponential increase in cost and a decrease in the availability of large, perfect, single-crystal diamonds, the anvil size is practically limited to ~0.5 carats. The diamond anvils are skillfully cut from gem-quality stones with a small culet, preferably parallel to the (100) plane of the diamond. The culet size varies from tens of μm to a few mm depending on the target P and experimental requirements. Simple flat culets [Fig. 2(a), top] have been used to generate a maximum P of 120 GPa (Yagi, Suzuki, and Akimoto, 1985).

In order to reach higher P, beveled anvils, which can be viewed as second-stage anvils on top of the flat culet [Fig. 2(a), middle], were invented (Mao and Bell, 1978). The culet diameters and bevel angle have since been fine-tuned and optimized for generating up to 300–400 GPa (Mao *et al.*, 1989;

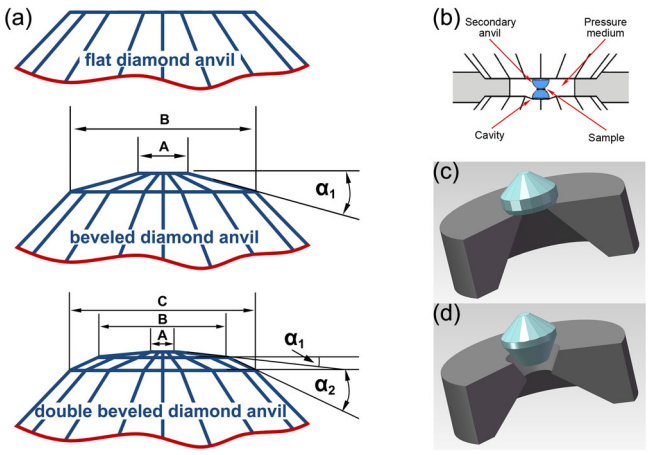

FIG. 2. Various culet designs and types of seats.

Mao, Wu, Hemley *et al.*, 1990). Further extension of this technique, using double-beveled anvils [Fig. 2(a), bottom], has not showed significant advantages. Very recently, a detached hemispherical second-stage anvil design (Dubrovinsky *et al.*, 2012, 2015; Dubrovinskaia *et al.*, 2016) reportedly generated a very high P up to 750 GPa [Fig. 2(b)] and offered exciting potentials, but has not yet been developed into a robust, reproducible high-P technique for studies of real samples.

Initially, the diamond anvil was simply a commercial brilliant-cut gem diamond (Bassett, 2009) with a critical modification of a culet facet at the pinnacle of the pavilion facets and thus named the "modified brilliant design." Later, when the anvil was manufactured from a rough stone rather than from a ready-made brilliant, a simplified "standard cut" was used. In the standard cut, the girdle diameter was reduced to increase its thickness, and all diamond-shaped cross-cut facets that were in the brilliant design for aesthetic purposes were omitted (Fig. 1). Both the modified brilliant and standard designs function similarly and are supported by their large flat-bottom tables. A substantial improvement on the anvil design [Fig. 2(d), the Boehler design] cuts a precise 60° conical crown to provide better lateral support and a much larger axial opening for optical and x-ray access (Boehler and De Hantsetters, 2004).

3. Anvil-supporting seats

The disk-shaped seat that supports the diamond anvil has a tapered opening for viewing and measurements [Figs. 2(a) and 2(d)]. The seat transmits the applied force from the DAC body to the anvil. The seat design must balance two contradictory requirements, namely, providing maximum support to the anvil, which prefers a thick, solid seat, and providing maximum accessibility for the diamond window, which prefers a thin seat with a wide angular opening. The Boehler seat, which has a conical hole matching the 60° conical crown of the Boehler anvil perfectly [Fig. 2(d)], has resolved this dilemma (Boehler and De Hantsetters, 2004). It has the distinctive advantage of leaving a large opening for the entire table to access optical and x-ray probes, while simultaneously providing additional hoop support to the anvils for a higher loading capability.

Tungsten carbide is generally used as a seat material because of its great strength which supports the diamond anvils. Other materials are chosen for special purposes. For instance, x-ray transparent Be (Merrill and Bassett, 1974) or cBN (Kantor *et al.*, 2012) seats are used for single-crystal x-ray diffraction (XRD) that requires maximum access to the reciprocal space. Re seats are used in hydrothermal DACs for high strength at high T. Nonmagnetic Cu-Be or Cr-Al-Cr (Uwatoko *et al.*, 2002) seats are used to minimize background in high-P magnetic measurements.

4. DAC body and compression mechanism

Numerous types of DACs have been developed and used by different researchers, such as the Bassett cell (Bassett, Takahashi, and Stook, 1967), the NBS cell (Piermarini and Block, 1975), the Mao-Bell cell, the Merrill-Bassett cell (Merrill and Bassett, 1974), the panoramic cell (Mao *et al.*, 1998), the BX90 cell (Kantor *et al.*, 2012), the Boehler plate cell (Boehler, 2006), the X cell (Liu *et al.*, 2014), the Letoullec design (Letoullec, Pinceaux, and Loubeyre, 1988), the Chervin design (Chervin *et al.*, 1995), etc. They share common considerations of alignment precision, reproducibility, and stability.

To reach high P and prevent premature failure, the diamond anvils must be aligned perfectly coaxially with the culets parallel to each other. Set screws for translational seat adjustments are often used to center the pair of anvils. Parallelism is achieved by a rocking hemispherical seat (Piermarini and Block, 1975) or a pair of semicylindrical seats (Bassett, Takahashi, and Stook, 1967) that provide the adjustment of 2 degrees of tilting freedom. It is also possible to premachine the anvils, seats, and DAC to sub-mrad precision so that the parallelism does not need to be adjusted.

The alignment must be reproducible and stable under compression. The alignment must remain unchanged during the operations of opening the DAC, loading the sample and P medium, and compression to the maximum P and T. Guidance features such as a piston-cylinder and pin-slot designs are commonly used to ensure stability of the alignment. The design of the plate DAC (Boehler, 2006) uses a very different principle by elastically deflecting the plates, but accomplishes the same results of reproducible and stable alignment.

Mechanically tightening the screws to compress spring washers is the most robust and versatile method for applying force to DACs. It has the advantage of extreme simplicity and stability; the P can even be kept constant for decades if necessary. It can be further augmented by the lever-arm mechanism, motor-driven gear box, pneumatic membrane, or piezoelectric (dynamic) driven attachment (Evans *et al.*, 2007) for higher loads, high-precision load change, precise loading rate, remote control, and rapid ramping. Piezoelectrically driven and membrane-driven controls are used for fast compression and decompression in order to study the phase transition and elastic or plastic properties of the materials under well-controlled compression and decompression rates (Evans *et al.*, 2007; Lee, Evans, and Yoo, 2007; J.-Y. Chen *et al.*, 2014; Smith *et al.*, 2015), bridging the gap in the time domain between static and dynamic compressions.

5. The limit and tradeoff of P and culet or sample size

The maximum achievable P depends on the optimization of multiple factors, including the culet size, shape, gasket materials, sample, quality of the DAC, etc. These factors are further obscured by numerous uncontrolled variables, such as the defects in the diamond anvils and the operator's skill, which may cause premature anvil breakage. Nevertheless, a clear trend of anticorrelation between the maximum P and culet size is shown in Table I and Fig. 3 from a compilation of studies by different research groups (Mao and Bell, 1978; Mao *et al.*, 1989; Ruoff *et al.*, 1990; Fujihisa and Takemura, 1995; Akahama, Kawamura, and Bihan, 2001; Loubeyre, Occelli, and LeToullec, 2002; Akahama and Kawamura, 2007, 2010; Sakata *et al.*, 2011; Dubrovinsky *et al.*, 2012; Boehler *et al.*, 2013). To reach Mbar P, usually an anvil-on-top-of-anvil configuration is recommended, i.e., either a single- or double-beveled culet [Fig. 2(a)] or a detached anvil [Fig. 2(b)].

The practical limit of routine experiments using the current DAC technology is ~400 GPa. In general, to reach higher P

TABLE I. Details of selected multimegabar experiments with different culet sizes in Fig. 3; A, B, C, $\alpha_1°$, and $\alpha_2°$ are the culet sizes and bevel angles, respectively, as shown in Fig. 2.

C (μm)	B (μm)	A (μm)	$\alpha_1°$	$\alpha_2°$	P_{max} (GPa)	Sample	Gasket	Reference
		< 4			640	Re	Re	Dubrovinsky *et al.* (2012)
350	250	20	15	8.5	408	Mo	Re	Akahama and Kawamura (2010)
	350	22		8.5	364	W	Steel	Ruoff *et al.* (1990)
		25		8	320	H	Re	Loubeyre, Occelli, and LeToullec (2002)
	300	30		8.5	384	Ir	W	Present unpublished result
450	250	35	15	7	297	Sc	Re	Akahama and Kawamura (2007)
	300	40		8.5	300	Fe	Steel	Mao, Wu, Chen *et al.* (1990)
	300	50		8.5	302	CsI	Steel	Mao and Hemley (1989)
	300	75		8	220	Ti	Re	Akahama, Kawamura, and Bihan (2001)
	300	100		8	241	Ca	cBN,Re	Sakata *et al.* (2011)
	300	150			190	Mn	Steel	Fujihisa and Takemura (1995)
	300	180		1.5	172	Steel	Steel	Mao and Bell (1978)
	660	230		2	155	Steel	Steel	Mao and Bell (1978)
		1000			94	H_2O	Steel	Boehler *et al.* (2013)

requires the use of a smaller culet size but when the culet size becomes diminishingly small, the precision and stability of the alignment become increasingly critical, and μm to sub-μm probing capability becomes essential.

Some measurements, such as neutron scattering, nuclear magnetic resonance, or ultrasonic interferometry, require a sample size greater than several hundreds of μm, thus a correspondingly large diamond culet and loading force are needed. Reaching megabar P becomes a challenge to support the diamond anvils and seats under very high loads on the DAC. Using prestressed, supported conical tungsten carbide seats or sintered diamond seats for beveled anvils, Boehler *et al.* (2013) reached 90 GPa with a culet size of 1 mm and a record large disk-shaped sample size of 500 μm diameter and 50 μm thickness.

B. Sample containment and stress environment

1. The sample, sample chamber, and sample loading

The sample chamber is formed by a hole in the gasket compressed between two culets (Fig. 4). The two opposing anvils squeeze the gasket and seal the rim around the chamber, which contains the P medium, sample, and P calibrant. Further compression of the gasket causes it to close in and apply P to contents in the chamber.

Solid or liquid samples and P markers are loaded into the gasket hole under a microscope with a micromanipulator or simply by skillfully using a needle. Depending on the inertness of the sample, the operation can be conducted in a glove box or air. Gaseous samples or P media can be loaded by condensing them cryogenically (Sharma, Mao, and Bell, 1980) or compressing them into the sample chamber at several hundred MPa (Mills *et al.*, 1980) and remotely closing the DAC to seal the chamber.

2. The gasket

The gasket between opposing culets sustains a large P gradient by anvil-gasket friction and confines samples in the sample chamber. Under very high P, the cupping effect of the culet further helps to encapsulate the sample and gasket materials from extrusion. The part of the gasket outside the anvils forms a thick ring supporting the tip of the anvils like a belt (Fig. 4). Preindentation is necessary before the experiment to avoid significant deformation and blowout of contents in the gasket hole.

The gasket hole that acts as the sample chamber can be drilled using a minidrilling machine, electrical discharge machining, a

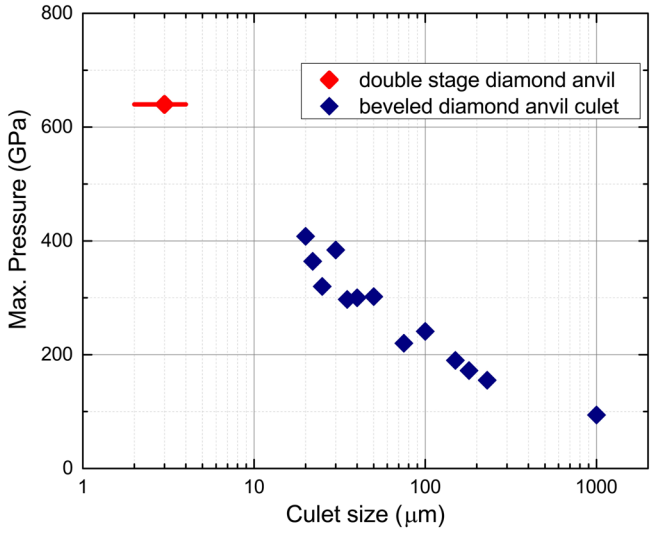

FIG. 3. Maximum P as a function of culet size from various groups together with our unpublished results.

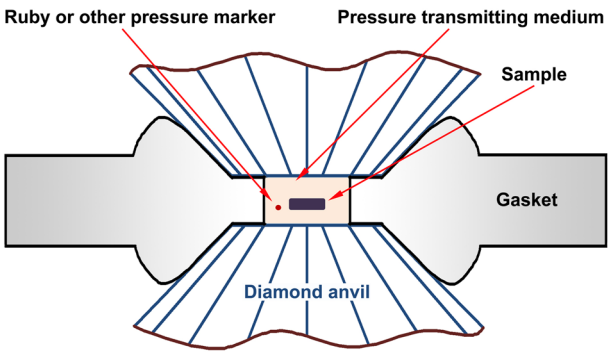

FIG. 4. Sample chamber configuration with the gasket, P transmitting medium, P marker, and opposing anvils.

laser, or a focused ion beam (FIB) (Orloff, Narayana, and Ruoff, 2000). It is recommended that the diameter of the gasket hole is less than one-third of the culet diameter to provide sufficient room for sealing the sample chamber.

Gasket materials are selected for their strength, inertness, and compatibility with the experiment. Work-hardened T301 stainless steel is an all-purpose gasket material. Rhenium or tungsten gaskets are used for ultrahigh P experiments. Because of their superior high-T strength, inconel and Re are used for resistance-heated DACs. Composite gaskets are designed with a Re gasket outside the culet area to optimize the tensile strength and a cBN insert inside the culet area to optimize the compressional strength. X-ray transparent gasket materials such as beryllium, boron, cBN (Funamori and Sato, 2008), diamond powder (Zou *et al.*, 2001), and Kapton (Merkel and Yagi, 2005) are used for radial access of the sample. Amorphous boron (Lin *et al.*, 2003) and bulk metallic glass (He *et al.*, 2003) are used to eliminate x-ray diffraction peaks from the gasket. For electrical transport studies, insulated gasket materials such as cBN, MgO, or Al_2O_3 are used (Solli and Jeanloz, 2001), while a nonmagnetic Cu-Be gasket (Ishizuka, 2005) is often used for magnetic measurements.

3. The quasihydrostatic P media

The hydrostatic state, in which the stresses at any given point are equal in all directions, provides a well-defined value for the P variable and is usually the preferred condition for high-P experiments. Such a state can be achieved only in a fluid with zero shear strength but in reality almost all fluids solidify and possess finite strength at high P. It is desirable to choose materials with a low strength to be used as the P transmitting media (Fig. 4), in order to keep the sample under a quasihydrostatic environment with minimal deviatoric stress.

P-transmitting media are selected based on their inertness to the sample, compatibility with the experiment, operational convenience, and the degree of quasihydrostaticity in the experimental P-T range. For example, a 4 : 1 methanol/ethanol mixture and silicon oil are fluid P media for experiments below 10 GPa but harden at higher P. Soft solids such as NaCl are easy to handle with moderately low deviatoric stress. Inert-gas solids, such as He and Ne, are considered the best P transmitting media, but require a special gas loading facility. H_2, O_2, N_2, and H_2O are convenient P media when such chemical environments are desired.

Klotz *et al.* (2009) and Tateiwa and Haga (2009) systematically studied the commonly used P transmitting media at room and low T, using ruby as an indicator. Klotz *et al.* (2009) studied the P distribution in the sample chamber to obtain the P deviation at high P and room T, while Tateiwa and Haga (2009) studied the full width at half maximum (FWHM) of the ruby $R1$ line revealing the nonhydrostatic effect in different P transmitting media under high P and low T. Two studies indicated that helium is the best P transmitting medium at both room and low T (Bell and Mao, 1981; Dewaele and Loubeyre, 2007).

4. The uniaxial compression condition

With the application of a uniaxial load, a sample without a P medium is expected to have a uniaxial stress component. A well-constrained uniaxial compression condition contains a wealth of information on the stress-strain relations, elastic anisotropy, plastic anisotropy, strength anisotropy, grain rotation, and the preferred orientation under stress. The shear strength is considered a key issue of high-P phase transitions, and nonhydrostatic data are important in their own right in rheological studies (Mao *et al.*, 1998; Wenk *et al.*, 2000; Merkel *et al.*, 2006). Studies of the stress-strain relationship in uniaxially compressed DAC samples have made a major impact on geophysics (Mao *et al.*, 1998; Wenk *et al.*, 2000; Merkel *et al.*, 2006) and nanomechanics (Chen *et al.*, 2012; B. Chen *et al.*, 2014). Additional developments of the rotational DAC (Ma *et al.*, 2006) with increasing shear stress have proven valuable for studying materials under a high-stress state.

C. P calibration

1. The applied force and P on the sample

The force applied to a DAC is transmitted to the anvil culets and generates a P distribution which can be probed and mapped by internal calibrants. The total integration of P over the area equals the applied force (Goettel, Mao, and Bell, 1985; Hemley *et al.*, 1997). The peak P on the sample at the center of the culet area increases with increasing load; the relation is nonlinear but follows an S shape that can be divided into three distinct stages, as shown in Figs. 5(a) and 5(b). During the initial stage I with a small loading force, P is uniformly distributed on the gasket and sample, causing elastic deformation of the gasket and plastic flow when the strength limit of the gasket is reached. The P gradient on the gasket is flat, and the P of the sample

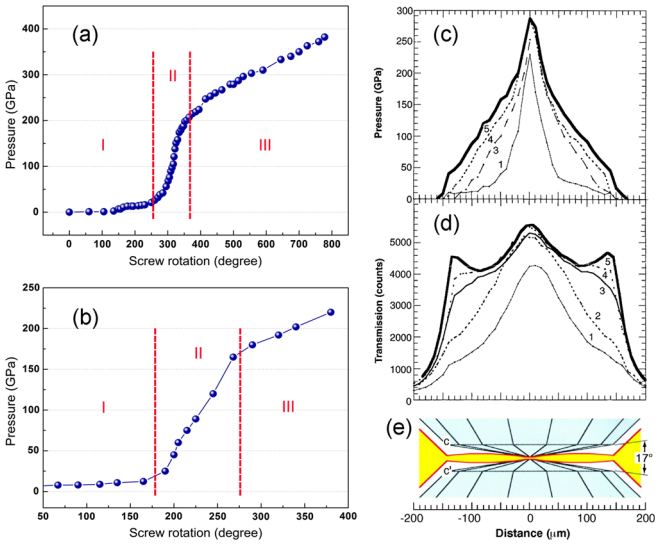

FIG. 5. (a) Characteristic S-shaped loading curves of the peak sample P up to 400 GPa at the culet center of the beveled diamond anvils as a function of the screw rotation (load), which is proportional to the force applied to the DAC; culet size, 30 μm diameter, beveled at 8.5° to 300 μm; P calibrant, Pt. (b) An experiment up to 220 GPa. (c)–(e) Culet sizes of 10 μm diameter beveled at 8° and 9° to 300 μm; (c) the P distribution, (d) thickness mapped by the x-ray absorption of the Re gasket, and (e) the cupping of the diamond anvils flattens the original 17° combined bevel angles. (c)–(e) From Hemley *et al.*, 1997.

increases very slowly. After the gasket has thinned down to a finite thickness and the plastic flow has essentially ceased, it enters stage II. The gasket becomes "locked in," and the increasing load concentrates on building up a sharp P gradient toward the pinnacle at the center, where the peak P increases rapidly and lineally with the applied load.

When the peak P reaches above 200 GPa, the extremely high P causes the rigid diamond culets to deform elastically [Fig. 5(d), curves 3–5], and "to cup" extensively. Eventually the bevel angle is flattened [Fig. 5(e)]. Further loading increases the P around the rim rather than the center, where the rate of P increase slows down to $<$ 1/3 of that in stage II. The experiment finally ends when P ceases to rise with the increasing load [Fig. 5(c), curves 3–5], or the anvil breaks abruptly.

Such S-shaped behavior is universally reproduced in all DAC experiments with beveled anvils if 250 GPa is reached. The unavoidable cupping limits the beveled diamond anvil design to a maximum P of no higher than ~400 GPa [see, e.g., Fig. 5(a)].

2. Selection of internal *P* calibrants

P of the sample is determined from a P calibrant in the sample chamber. Commonly used P scales are based on materials properties that are well-determined functions of P. These properties need to be easily measurable in the laboratory, with high resolution, sensitivity, reproducibility, accuracy, and P-T stability (i.e., no phase transition).

The primary P scale is a function determined from the *ab initio* definition of P, such as the applied force on an area. However, experiments based on the primary scales are often difficult to conduct. Once we calibrate any P dependent function against a primary scale, the function becomes a secondary P scale. For instance, optical spectroscopy-based secondary P scales are easily accessible and widely used in laboratories, and XRD-based secondary P scales are conveniently used in synchrotron x-ray experiments.

3. Secondary *P* scales based on optical spectroscopy

The ruby florescence shift has many advantages as a P scale, including its very intense and sharp florescence line, sensitivity to P changes, and chemical and structural stabilities with many samples and P transmitting media. Since its establishment (Forman *et al.*, 1972) and subsequent calibration to megabar (Mao and Bell, 1976), it has become the most popular scale for the DAC community.

At room T, the ruby P scale has a slightly superlinear relation (Fig. 6). The 1986 quasihydrostatic ruby scale to 80 GPa (Mao, Xu, and Bell, 1986) is still widely used up to 100 GPa. Revisions by Holzapfel (2003) and others (Chijioke *et al.*, 2005; Dorogokupets and Oganov, 2007) are consistent (Fig. 6, red curve) with ±2% at 150 GPa (Syassen, 2008). The ruby peak broadens and weakens at very high P and ceases to be a usable P scale above 200 GPa.

Below room T, the ruby P scale has been calibrated with consideration of T corrections (Vos and Schouten, 1991). At high T, the R1 line broadens dramatically and ceases to be a useful P scale above 400 °C, and other luminescence sensors have also been proposed for high-P calibration. The advantage of rare-earth (RE) f-fluorescence dopants, such as Sm or Eu

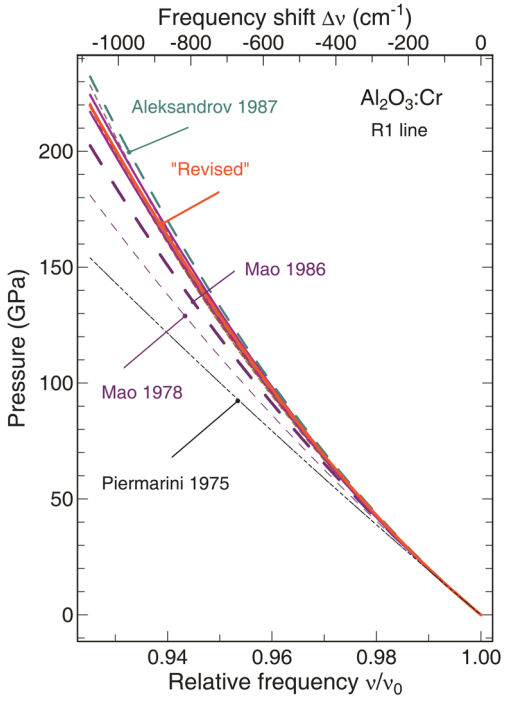

FIG. 6. Ruby P calibration as a function of the relative frequency shift of the $R1$ line. From Syassen, 2008.

(Shen, Gregorian, and Holzapfel, 1991), over the Cr d fluorescence in ruby, is their small T broadening. $SrB_4O_7:Sm^{2+}$ has been used successfully as a high-T P scale up to 1000 K (Datchi *et al.*, 2007).

Raman spectra based sensors, such as diamond, cBN, and SiC (Zhuravlev *et al.*, 2013), have also been used to calibrate P. Raman peaks do not broaden significantly at high T and can be used as excellent P scales (Datchi *et al.*, 2007). Isotopically pure ^{12}C or ^{13}C diamonds are used as calibrants because their Raman signals are different from those from the diamond anvils with natural C isotopic abundance.

At ultrahigh P above 200 GPa, where all other optical calibrants become too weak to use, Raman scattering from the tip region of the diamond anvil next to the sample chamber has been used for P calibration. The strong first-order diamond Raman peak shifts to a higher frequency with increasing pressure and this shift can be calibrated for P determination. The tip region of the culet is an integral part of the overall diamond anvil, and its Raman spectrum is inseparable from the continuum plateau of the Raman spectra that originates from the stress gradient of the entire diamond. Therefore, in practice, unless the measured diamond is detached from the anvil (Occelli, Loubeyre, and LeToullec, 2003), the calibration is taken from the high-frequency edge of the plateau, which shows a distinctive peak in the differentials. At room T, this method has been calibrated up to 410 GPa (Akahama and Kawamura, 2010) and offers a valuable backup in case other P sensors are unavailable, although it carries significant uncertainty of ~15%.

4. Primary *P* scales based on *P*-*V* equations of state

Similar to force and area determination, the primary P scale can be determined experimentally by two independent variables of the state functions. For instance, using the volume

of MgO determined by XRD and bulk sound velocity determined by Brillouin spectroscopy, an MgO primary scale was generated (Zha, Mao, and Hemley, 2000). Shock-wave experiments that determine wave velocity and particle velocity independently have generated a full database of *P-V* equations of state (EOSs) of elements and simple compounds that can be used as primary *P* scales. High-*P* XRD is performed to find the high-precision unit cell parameters of standard materials from which *P* can be derived from their EOSs. Inert, high-symmetry, crystalline materials with a strong XRD signal, such as Pt, Au, MgO, are used as *P* calibrants. The EOSs of *P* media, such as NaCl, Ne, Ar, and the gasket materials, such as W and Re, can also be used as a backup *P* calibrant. Using an EOS for *P* calibration is particularly popular in synchrotron x-ray studies, where the XRD data of calibrants are a convenient by-product.

D. Temperature change at high *P*

The development of heating and cooling techniques has further extended multimegabar studies into the *T* regime up to 6000 K (Shen *et al.*, 2010; Tateno *et al.*, 2010) and down to 27 mK (Eremets *et al.*, 2000). A combination of *T* and *P* in the same experiment greatly widens the research scope and provides crucial tests to theories. Figure 7 shows the *P-T* range achievable in a DAC using various heating and cooling techniques.

1. Electrical resistance heating

Electrical resistance heating can be conducted inside the region between the anvils or outside the anvil, thus called internal and external resistance heatings, respectively.

External resistance heating can generate a very steady and homogeneous *T* field in the sample. The disadvantage is that it heats a large region including the gasket, anvils, seats, and possibly the whole DAC. The external resistive heater heats the sample by heat conduction and radiation. Electrical conductive metal wire (Dubrovinskaia and Dubrovinsky, 2003) or a graphite ring (Du *et al.*, 2013; Miyagi *et al.*, 2013) is used as a heating element. High-*T* refractory materials are required to make the DAC body and all critical components affected by heating. To avoid the oxidation of the anvils and DAC components above 900 K, they must be enclosed in a vacuum chamber or an inert atmosphere. Problems of *T*-induced oxidation and graphitization of the diamond anvils, the deformation of the cell body, and the softening of the gasket material make this method increasingly challenging at increasing *T* and limit the accessible *T-P* range below 1500 K.

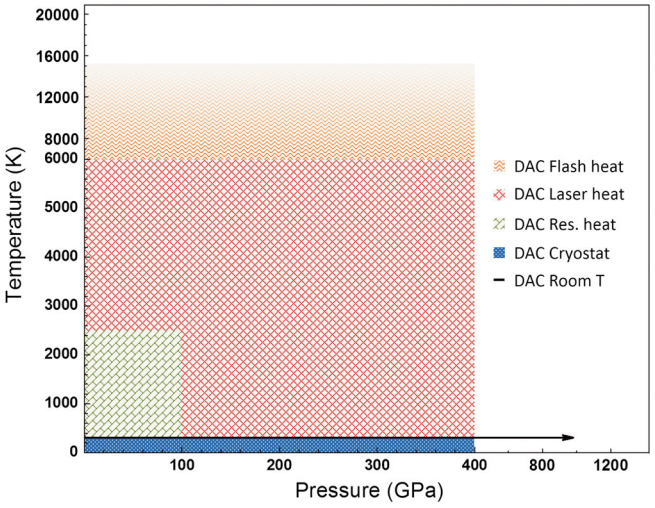

FIG. 7. *P-T* range of the DAC.

Internal resistance heating uses a microheater (Weir *et al.*, 2009) inside the sample chamber (Miletich, Cinato, and Johänntgen, 2009) around the sample. It was first used by Liu and Bassett (1975) and later improved by many others (Boehler *et al.*, 1986; Dubrovinsky, Saxena, and Lazor, 1997; Zha and Bassett, 2003). This method focuses the heating spot on the sample chamber area rather than the whole DAC body. Thus, it has made striking progress in achieving *T* above 2000 K at *P* up to 80 GPa (Zha *et al.*, 2008). However, the complexity in sample loading and preparation procedures limits its applications.

2. Laser heating

A higher *T* region is accessed by the laser-heating technique invented by Ming and Bassett (1974). It is now possible to heat the sample in a DAC to 1200–6700 K (Boehler, 2000). The infrared (IR) laser passes through the transparent diamond window and spot heats only the laser-absorbing samples without heating the anvils, gasket, and other DAC components, thus minimizing interference with the DAC operation and sample probing. Because of the transient nature of laser heating and the steep *T* gradients outside the heating spot, contradictory results were reported in the early days by different laboratories, causing confusion about the efficacy of the laser-heating technique. Significant progress in shaping, defining, and mapping (Campbell, 2008) the *T* distribution in the laser-heated DAC has since been made. Now, the laser-heating method is approaching the *T* accuracy of other high *P-T* techniques by using a "double hot-plate" system (Shen *et al.*, 2001), which exploits the optimal laser characteristics, sample configuration, and optical arrangement. The laser-heating technique does not couple well with transparent samples and requires an opaque, laser-absorbing sample. This problem has been overcome for solid samples by mixing inert laser absorbers, and for fluid samples by using a metallic foil with a high melting point (Pt, Re, or W) as the laser absorber, effectively acting like a donut-shaped internal furnace (Lin *et al.*, 2004). Transparent samples such as CO_2 have been heated up to 1660 K at 67 GPa (Santoro *et al.*, 2004), demonstrating the heating efficiency of the internal donut furnace method.

The accuracy and precision of *T* measurements in the laser-heating DAC have been improved significantly with the use of spectral radiometry systems. The thermal radiation spectrum is fitted to the Planck radiation function to determine the *T*:

$$I_\lambda = c_1 \varepsilon_\lambda \lambda^{-5} [\exp(1 - c_2/\lambda T)],$$

where I_λ is the spectral intensity, λ is the wavelength, ε_λ is the emissivity, and the two constants are $c_1 = 2\pi hc^2 = 3.7418 \times 10^{-16}$ W m^2 and $c_2 = hc/k = 0.014388$ mK, where h is the Planck constant, c is the speed of light, and k is the Boltzmann constant. The use of a conventional laser-heating system is limited to temperatures above 1200 K due to the

insensitivity of the charge coupled device (CCD) detector in the IR region that is essential for characterizing low T. This problem can be resolved by using an IR sensitive detector and IR optics to extend the temperature measurement down to 500 K (Shen *et al.*, 2010). The region between 300 and 500 K can easily be reached by heating tapes, hot plates, and many other simple methods and is considered a small perturbation of ambient T.

Pulsed laser heating has been developed to reach extreme T in DAC. This technique requires far less average power than a continuous laser. The power is mainly used to raise T of the sample with little thermally activated diffusion into the gasket or diamond. It suppresses the chemical reactions of the samples with the environment. It can attain very high T up to >10 000 K (McWilliams *et al.*, 2015) in a short time period, without the concern of overheating and breaking the diamond anvils. Experiments can now be extended to a very high P-T regime by combining pulsed laser heating, pulsed laser spectroscopy, time-resolved measurement, and a gated detector for thermal emission measurement with a time resolution as short as 5 ns (Beck *et al.*, 2007).

3. Cryogenic systems

With the immense interest in studying the low-T properties at high P, such as the transport properties, magnetic and structural transitions, and superconductivity, DAC and cryogenic technique have been integrated with DAC. Unlike heating, which can be focused locally in a small sample region, the sample and the entire DAC must be cooled down in cryogenic experiments. Many standard low-T devices can be used for cryogenic high-P experiments: i.e., the cryogen flow system, the ^{3}He system, the closed cycle refrigerator (Tanino, 1986), and the helium dilution refrigerator (Palmer *et al.*, 2015). The cryogen flow system uses liquid cryogen (nitrogen 77 K or helium 4 K) stored in an external dewar to cool down the sample. T is controlled by adjusting the flow rate and heaters inside the cryostat. The sample is either directly in contact with the evaporating liquid cryogen or indirectly cooled through a cold-finger heat exchange stage in a vacuum. The closed cycle refrigerator runs with helium gas, which cools during expansion and is recompressed to continue the thermal cycle, thus minimizing the helium consumption. To reach sub-kelvin temperatures, a ^{3}He/^{4}He dilution refrigerator is required. The record low-T high P of 27 mK at 155 GPa was reached with a dilution refrigerator (Eremets *et al.*, 2000).

III. MULTIPLE PROBES FOR HIGH *P-T IN SITU* CHARACTERIZATIONS

Integrations of the DAC with an array of optical, laser, x-ray, and electromagnetic transport probes have enabled *in situ* high P-T observations with accuracy rivaling ambient condition investigations. These tools, integrated with hydrostatic or uniaxial media, laser or resistive heating, and cryogenic cooling, have enabled investigations of structural, vibrational, electronic, and magnetic properties over an extensive P-T range and have been the basis for major discoveries in the physics community.

A. High-P optical absorptive and reflective microscopy and spectroscopy

With optical microscopy, the P effects on the color, morphology, and growth of samples in real time can be directly observed, and the color change can be further quantified by absorption and reflective spectroscopy (Ma *et al.*, 2009; Qi *et al.*, 2015) to identify the metal-to-insulator transition of sodium at high P.

High-P absorption has been used to characterize the band-gap reduction and closure of semiconductors at high P. For example, Fig. 8 shows the P effect on the optical absorption threshold energy of C_{60} (Moshary, Chen, and Silvera, 1992). Extrapolation of the absorption edge measured in the range of 0–17 GPa indicates that the metallization of C_{60} should occur at ~33 GPa. By measuring the absorption edge of hydrogen above 300 GPa in a DAC, Loubeyre, Occelli, and LeToullec (2002) predicted that hydrogen metallizes at about 450 GPa.

In the IR wavelength range, synchrotron radiation provides a high-flux, broadband source, which is essential for measuring the transmission at the longest wavelengths allowed by the diffraction limit of the small samples at very high P. It has been used to study hydrogen up to 360 GPa. These measurements provide crucial information about the lattice vibrations and electronic properties, including whether the material has converted into a metallic state (Zha, Liu, and Hemley, 2012; Loubeyre, Occelli, and Dumas, 2013).

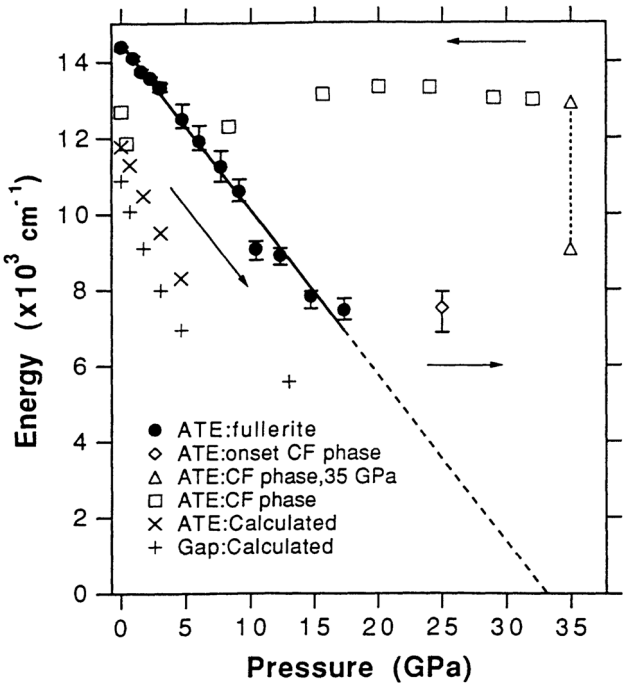

FIG. 8. The optical absorption threshold energy (ATE) as a function of P. Arrows indicate the P path. Open symbols indicate the behavior after the phase transition. Triangles at 35 GPa indicate the range of spatial variations in the sample. Open squares represent the ATE in the most transparent region. Theoretical predictions are also shown in the figure for comparison. From Moshary, Chen, and Silvera, 1992.

B. High-*P* inelastic optical scattering

Diamond is an ideal optical window for lights with a wide energy range from infrared, visible, to ultraviolet. It enables many *in situ* optical spectroscopic studies, such as Raman spectroscopy, Brillouin scattering, and fluorescence spectroscopy. These techniques are essential for the high-*P* studies of phonon and electronic structures in the DAC.

1. High-*P* optical Raman spectroscopy

Covering the energy range of several cm^{-1} to thousands of cm^{-1}, optical Raman scattering coupled with the DAC provides a convenient and versatile method for investigating the *P* effects on structural, vibrational, electronic, and magnetic changes in materials up to the maximum attainable *P*. It is an indispensable tool and is usually the first instrument that every high-*P* laboratory acquires (Loubeyre, Occelli, and LeToullec, 2002; Wang *et al.*, 2012; Howie, Dalladay-Simpson, and Gregoryanz, 2015; Yu *et al.*, 2015).

Raman spectroscopy has played a major role in studying the condensed matters of light elements, such as hydrogen. For example, Loubeyre, Occelli, and LeToullec (2002) conducted hydrogen Raman studies up to 320 GPa at 100 K and found that the vibron signature of the H_2 molecule persisted to at least 316 GPa. No phase transition was detected above 160 GPa and solid hydrogen was observed turning opaque at 320 GPa. Recently, Howie *et al.* (2012, 2014), Howie, Dalladay-Simpson, and Gregoryanz (2015), Dalladay-Simpson, Howie, and Gregoryanz (2016), Liu, Dalladay-Simpson *et al.*, 2017, Silvera and Dias, 2017, and Zha *et al.* (2017) studied the melting and phase transformations of hydrogen using Raman spectroscopy as the only available probe for hydrogen at ultrahigh *P* and high *T*.

Raman spectroscopy is ineffective for studying metals due to the very short mean-free path of the optical laser in metal. However, it has been used to study metal-to-insulator transitions under high *P*; for example, Ma *et al.* (2009) reported that metallic sodium transforms into an insulator state above 200 GPa. The corresponding Raman spectra show no features below 130 GPa, but a pronounced Raman spectrum appears at higher *P*. This indicates a major phase transformation, which is associated with a gradual decrease in the reflection of visible light from the sample. Above 150 GPa, the Raman spectra again show marked changes, including a strong decrease in intensity, which signifies another phase transition.

Raman scattering has been used for probing not only the *P*-induced changes of the molecular arrangement, but also molecular changes themselves. For example, Raman spectra have been used to identify collapsing C_{60} cages induced by *P*. Wang *et al.* (2012) studied the Raman spectra of compressed solvated C_{60} at different *P*. Their observations suggest that the C_{60} cages start to collapse at 32 GPa and completely transform into amorphous carbon clusters at higher *P*.

The evolution of an electronic B_{1g} mode with *P* in $YBa_2Cu_3O_{7-\delta}$ was used to identify the mechanism of superconductivity in high-*T* superconductors (Goncharov and Struzhkin, 2003).

2. High-*P* Brillouin spectroscopy

Brillouin scattering is dominated by low-frequency phonons and therefore measures the elastic behavior of materials. The acoustic velocities can be determined *in situ* at high *P* from the Doppler shift of laser light by acoustic waves (Li *et al.*, 2006). Brillouin scattering is used to investigate the elastic properties and high-frequency viscous behavior of crystalline and amorphous solids, liquids, molecular solids, and glass-forming compounds and can also provide information on other high-*P* properties such as the refractive index (Matsuishi *et al.*, 2003), photoelastic properties, hypersonic attenuation, structural relaxation, or phase transitions (Grimsditch and Polian, 1989; Speziale, Marquardt, and Duffy, 2014).

Coupled with EOSs measured from x-ray diffraction, Brillouin scattering has been used to build a primary *P* scale independent of the *a priori P* standard. For example, Zha, Mao, and Hemley (2000) completed a study of the elasticity and the EOS of MgO up to 55 GPa in a DAC using high-*P* single-crystal Brillouin scattering and synchrotron x-ray diffraction techniques. Integration of single-crystal velocity measurements from Brillouin scattering and density information from XRD gave the three principal elastic tensor elements (C_{11}, C_{12}, and C_{44}) and various secondary elasticity parameters, including the single-crystal elastic anisotropy, Cauchy relation, aggregate sound velocities, and Poisson's ratio, as functions of *P*. The study provided a direct determination of a primary *P* scale.

When XRD is integrated with Brillouin scattering measurements, it is possible to simultaneously refine both the elastic constants and sample orientation in high-symmetry single crystals. The elastic tensor was resolved for a H_2S single crystal grown in a DAC up to 7 GPa (Shimizu and Sasaki, 1992). This method provides a means for systematic studies of the elastic properties and phase transitions of condensed gases under high *P*.

Brillouin scattering spectroscopy is vital for comparing Earth materials with deep Earth seismological observations. It can be effectively coupled with a laser-heated DAC for studying seismic velocities in the lower mantle *P*-*T* conditions ranging from 24 GPa-2000 K to 135 GPa-2800 K (Murakami *et al.*, 2007, 2012; Speziale, Marquardt, and Duffy, 2014). Figure 9 summarizes the available elasticity data of important mantle minerals measured mainly using Brillouin scattering at high *P*-*T*.

In situ Brillouin scattering has also been used to study transitions in glass and liquid. Tkachev, Manghnani, and Williams (2005) carried out Brillouin scattering measurements of a silicate glass and showed a dramatic increase in the *P* dependence of the longitudinal velocity and a discontinuity in the compressibility of the glass, suggesting a second-order polyamorphic transition. Li *et al.* (2006) used Brillouin scattering with an externally heated DAC to observe water structural transformation from low-density to high-density regimes indicated by elastic discontinuity.

The Brillouin scattering technique was used to measure the sound velocity in polycrystalline H_2O ice up to 100 GPa by Ahart *et al.* (2011). They found that the aggregate shear modulus increased monotonically with *P* and was about

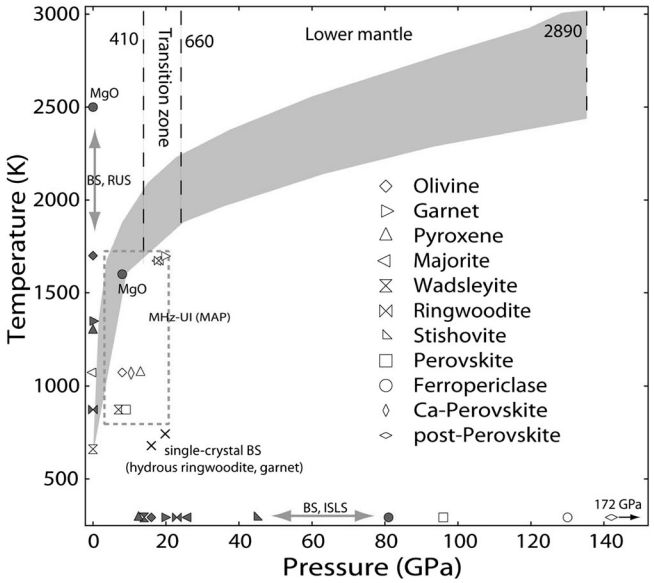

FIG. 9. Elasticity data of important mantle materials measured at high *P-T*. The shaded area illustrates the range of *P-T* conditions in the Earth's transition zone and lower mantle. Open symbols: polycrystalline samples; full symbols: single-crystalline samples. From Speziale, Marquardt, and Duffy, 2014.

110 GPa at 60 GPa. The high value of the aggregate shear modulus plausibly gives rise to the high shear strength in ice VII.

3. High-*P* optical fluorescence spectroscopy

The fluorescence of a material involves excitation of an electron from the ground state to an excited state. After a certain lifetime, the electron decays to a lower level and emits fluorescent photons with energy equal to the difference between the excited and the final state. Fluorescence spectroscopy can provide important information for understanding electronic structures. High *P* can alter the band gap and charge transfer, and all band structures can be efficiently modified. Fluorescence spectroscopy has been used to study the *P* effects on a variety of materials including semiconductors, rare-earth oxides, phosphors, fullerenes, etc.

The fluorescence of both bulk and nano ZnO under high *P* were studied using *in situ* high-*P* photoluminescence (PL) (Chen *et al.*, 2006). The PL spectrum taken at atmospheric *P* exhibits the dominant near-band-edge exciton transitions and a broadband deep-level emission structure centered in the yellow spectral region. Under compression, these excitonic spectral features shifted toward higher energy as the ZnO band gap increased. The near-band-edge PL features did not decrease in intensity until the samples underwent *P*-induced phase transitions from a direct-gap wurtzite to an indirect-gap rock salt structure.

C. High-*P* ultrasonic probes

Brillouin scattering in the DAC is a powerful tool for elasticity measurements up to 100 GPa. However, it is limited to transparent single crystals. The development of ultrasonic interferometry at near-optical wavelengths enables measurement of the high-precision elastic-wave travel times of single crystals in a submillimeter size. The application of gigahertz technology in the DAC has been used to study the elasticity and sound velocity of opaque samples at *P* up to 150 GPa (Spetzler *et al.*, 1996; Bassett *et al.*, 2000; Jacobsen *et al.*, 2002, 2004; Decremps *et al.*, 2014).

Utilizing single-crystal XRD and gigahertz ultrasonic interferometry to generate high-frequency shear waves, Jacobsen *et al.* (2002) studied the effects of nonstoichiometry on the elastic moduli of (Mg,Fe)O. The acoustic technique featured a *P*-to-*S* elastic-wave conversion by internal reflection on the oriented facet of a single-crystal MgO buffer rod. The full elastic tensor C_{ij} of minerals can be measured at extreme conditions without optical constraints. With the same method, Jacobsen *et al.* (2004) also studied the effects of *P* and the composition on the shear-wave velocities in magnesiowüstite (Mg,Fe)O: a major lower-mantle oxide. They found that the magnesiowüstite containing more than 50% iron exhibits *P*-induced softening of the C_{44} shear mode, indicating instability in the rock salt structure. Furthermore, similar to MgO, the oxide containing 20% iron shows increasing shear velocities, indicating that the oxide should have a wide *P*-stable field. The relative stability of Mg-rich (Mg,Fe)O and the strong compositional dependence of the shear-wave velocities in (Mg,Fe)O imply that the seismic heterogeneity in Earth's lower mantle may result from compositional variations rather than phase changes in (Mg, Fe)O (Jacobsen *et al.*, 2004).

While the gigahertz ultrasonic interferometry method is versatile, accurate measurements at very high *P* still suffer from limited quasihydrostaticity. Recently, Decremps *et al.* (2014) combined a picosecond ultrasonics technique with a DAC and studied the acoustic properties of iron up to 150 GPa. Figure 10 shows a schematic diagram of the DAC and picoseconds acoustics combination setup, which allows the direct measurement of the longitudinal sound velocity in the region of 100 GPa.

D. High-*P* XRD of polycrystalline, single-crystal, multigrain, and amorphous materials

Synchrotron x-ray radiation provides powerful, penetrating, versatile probes for a full range of diagnostic studies of samples in DACs. XRD has long been the most basic probe for the *in situ* identification of high *P-T* phases and the determination of *P-T-V* EOSs and other elastic properties. One of the two geometries of the x-ray beam relative to the DAC is generally used, namely, the axial XRD in which the incident x-ray beam passes through a diamond anvil along the axial direction of the DAC to impinge upon the sample, and the diffraction x-ray passes through the second anvil or the radial XRD in which the incident x-ray beam in the radial direction of the DAC passes through an x-ray transparent gasket. The radial XRD is used for studying rheology, preferred orientation, and elasticity of samples under uniaxial stress (Mao *et al.*, 1998). Most XRD studies are conducted with the axial geometry.

For a century, XRD has been conducted with one of two extreme sample conditions: (1) a single crystal, which produces a single set of diffraction spots, directly

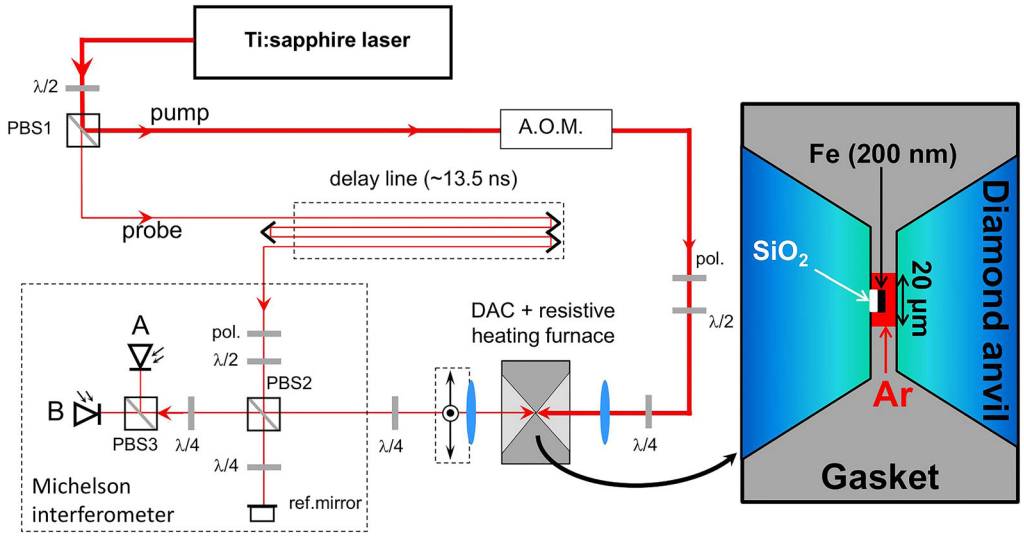

FIG. 10. Schematic diagram of the DAC and picosecond acoustics combination setup in the transmission configuration. The light source is a femtosecond Ti:sapphire laser delivering $\lambda = 800$ nm light pulses of about 100 fs width at a repetition rate of 79.66 MHz. The output of this pulse laser is split into pump and probe beams focusing on two opposite surfaces of the sample. The pump beam is then modulated at the given frequency of 1 MHz by an acousto-optic modulator (A.O.M.). Both real and imaginary parts of the reflectivity are measured using a Michelson interferometer. PBS: polarizing beam splitter; $\lambda/4$: quarter-wave plate; $\lambda/2$: half-wave plate; pol.: linear polarizer; A and B: diodes. From Decremps *et al.*, 2014.

corresponding to the geometric orientation of the crystal; or (2) a polycrystalline or powder sample, which comprises a large number of randomly orientated crystals, so numerous that the diffraction spots overlap and merge into smooth rings for each class of a reflection plane. The geometric relation is completely lost and only the *d*-spacing information of the diffraction planes is observed. DAC experiments have used both methods too, but neither is optimal. The powder samples are usually comprised of an insufficient number of crystals and produce spotty instead of smooth rings, resulting in unreliable intensity measurements. On the other hand, it is difficult to keep a single crystal intact without crushing it under extreme P and through phase transitions.

Polycrystalline XRD is by far the predominant method used for the DAC at high P (Duffy, 2005). For a single phase or high-symmetry multiple phases, polycrystalline XRD may be used effectively for the discovery of new phases. However, polycrystalline XRD has intrinsic limitations when the sample consists of multiple phases with orthorhombic or lower symmetry. Diffraction rings cover most of the detector area, and only a couple of low-angle diffraction rings are unique to a phase; most other rings overlap with one another and cannot be used for the unique identification or accurate determination of the crystallographic parameters (Lee, O'Neill, and Jeanloz, 2004). New structures and minor phases are often overshadowed by the diffraction of major phases and are impossible to find or identify. Advanced crystallographic software, such as RIETVELD and LEBAIL, may get the most out of a powder pattern but cannot overcome these intrinsic limitations. In addition, the common practice of integrating the 2D ring into a 1D peak plot throws away valuable information, such as the azimuthal angle (η) of the diffraction spot around the ring.

Single-crystal XRD contains orientation and geometrical relationships in addition to *d* spacings and thus provides a definitive characterization of the unit cell and symmetry (Finkelstein *et al.*, 2014). Unless the crystal is orientated exactly relative to the incident monochromatic x-ray beam to satisfy the Bragg relation, the crystal gives no signal and the detector remains blank. Rotating the crystal around the ω axis (perpendicular to the incident x-ray beam) can bring the crystal to Bragg conditions and momentarily generates a single diffraction spot at a given η and ω angles. For a typical DAC with a 40° (inclusive) conical opening, access to the reciprocal space is limited to $\pm 10°$, and the number of XRD spots after a complete rotation is still quite limited, with only a couple of dozen spots for a crystal. Larger openings up to 100° can be made with Be, cBN, or diamond backing plates, but typically at the expense of sacrificing the maximum attainable P-T range. In spite of its advantages, a single crystal cannot be sustained through phase transitions and often breaks down into multiple crystals and generates spotty XRD patterns.

Spottiness, which is generally regarded as a flaw in polycrystalline XRD, can be turned into a great advantage if crystallites are separated and handled as individual single crystals. The high-brilliance x-ray beam available at synchrotron facilities has made it possible to collect diffraction spots in a powder sample comprised of hundreds of submicron crystallites. The experimental setup (Fig. 11) and data collection procedure are identical to single-crystal XRD. With hundreds of crystallites, the number is large enough that different diffraction spots with well-defined η appear in every ω step (Fig. 12, left), but it is also sufficiently small so that the strong spots do not overlap into continuous rings. The summation of XRD images over the complete $-10°$ to 10° ω scan results in a spotty powder image (Fig. 12, right), which

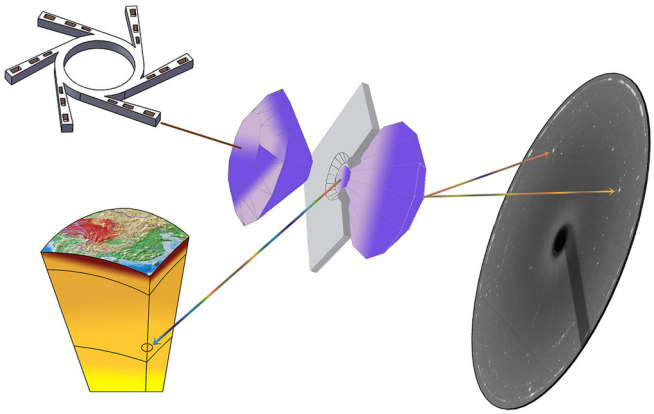

FIG. 11. Schematic diagram of *in situ*, high-*P* synchrotron XRD of a DAC sample at high *P-T* conditions. High-energy, high-brilliance, x ray from a synchrotron beam line is focused through a diamond anvil and impinges upon the mineral samples at high *P-T* conditions simulating the Earth's deep interior. The diffracted x-ray spots from the sample in the DAC pass through the second anvil and create a two-dimensional image on a CCD detector.

can be integrated and processed like a normal polycrystalline XRD.

The process of identifying diffraction spots and searching for the orientations of hundreds of single crystallites presents a major computational challenge. Fortunately, the newly developed fully automatic beam line experiment (FABLE) software package (Sørensen *et al.*, 2012), which is a suite of programs used for processing and indexing diffraction spots, is capable of separating and identifying the crystallographic orientation of each individual crystallite in the aggregate of hundreds of crystallites. The indexing procedure is carried out by the program GRAINSPOTTER in the FABLE package. Once separated, the data set for each crystallite can be handled with the standard single-crystal refinement program that is identical to a stand-alone single crystal, resulting in excellent statistics in refinement and full coverage of the reciprocal space.

This method developed by Zhang *et al.* (2014) is very powerful for the unequivocal determination of symmetry and unit cells, testing different indexing models, picking out minor phases, and even resolving the strain of individual crystallites.

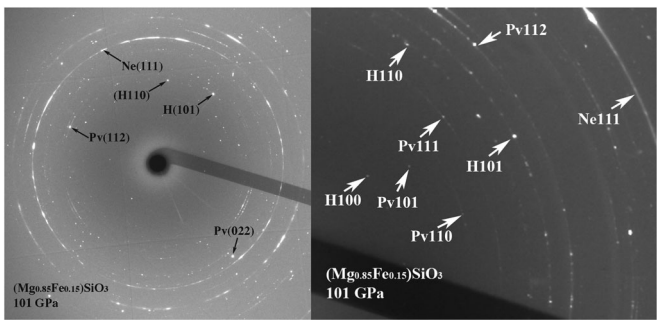

FIG. 12. Left: 2D multigrain XRD image at $\omega = 0°$ showing the discrete diffraction spots of Pv and the H phase. Right: Summation of ω step scans from $-10°$ to $10°$ showing polycrystalline XRD rings with single-crystal-like spots.

It has been used successfully to solve the crystal structure of postperovskite and discover a new *H* phase at megabar *P*. The main limitation for applying multigrain crystallography (MGC) is the overlapping of diffraction spots originating from too many crystallites. This can be controlled by growing the crystal size and/or reducing the beam size. For instance, in experiments at 101 GPa, the sub-μm crystallites matched the x-ray beam spot of 6×8 μm^2 well. The MGC method found 154 individual crystallites, each with 11 to 27 reflections consistent with the $(Fe_{0.4}Mg_{0.6})SiO_3$ *H* phase, and 130 individual crystallites of the $MgSiO_3$ perovskite (Pv) with a maximum of 48 reflections (Zhang *et al.*, 2014). If the spots are too numerous, the beam size can be reduced to cover less grains or the grain size increased by further annealing at high *P-T*.

High-*P* XRD has also been used to study amorphous systems such as liquids and glasses under extreme conditions. For example, liquid iron alloys (Fe-5 wt%, Ni-12 wt% S, and Fe-5 wt%, Ni-15 wt% Si) have been measured up to 94 GPa and 3400 K using XRD in a laser-heated DAC (Morard *et al.*, 2013). With careful background subtraction, signal normalization, and Fourier transformation of the diffraction patterns, the densities of the liquid alloys were successfully extracted and used to determine the *P-V* EOSs of the liquids. To optimize the weak XRD signals from the scattering of amorphous materials by minimizing the absorption and scattering of the diamond anvils, Soignard, Benmore, and Yarger (2010) designed a perforated DAC by perforating the anvil to within 50–100 μm of the sample; the amount of diamond and the resulting background or interference was dramatically reduced. SiO_2 and B_2O_3 glasses were measured up to the *P* of 50 GPa with the perforated diamond anvils and high quality data were obtained.

E. High-*P* x-ray spectroscopy

External fields such as x rays can perturb condensed matter and turn ground states into excited states. Therefore, the energy and other properties of the excited states can be probed by x-ray spectroscopy or inelastic x-ray scattering (IXS) methods, which also provide information about the ground states. With the advancement of synchrotron technology, a great number of powerful probes have been developed for the wealth of physical phenomena and properties under compression.

X-ray spectroscopy is ideally suited to high-*P* applications if the x-ray photons have sufficient energy to penetrate the anvils or gasket to reach the sample. It includes nonresonant inelastic scattering (NIXS), resonant inelastic x-ray scattering (RIXS), resonant x-ray emission spectroscopy (RXES), nonresonant x-ray emission spectroscopy (XES), and x-ray absorption spectroscopy (XAS). XAS can be further divided into x-ray near edge structure spectroscopy (XANES) and extended x-ray absorption fine structure, in addition to XAS-based spectroscopic methods such as x-ray magnetic circular dichroism (XMCD). Furthermore, there is another type of x-ray spectroscopic technique that utilizes nuclear resonant scattering, which can also be divided into nuclear resonant inelastic x-ray scattering (NRIXS) and nuclear resonant forward scattering (NRFS) also known as synchrotron Mössbauer spectroscopy (SMS) methods. A formal and

detailed description of how x rays interact with matter and the IXS and XAS techniques can be found in the reviews by Schülke (2007), Rueff and Shukla (2010), Ament *et al.* (2011), and van Veenendaal (2015). Here we focus on their high-P applications. The developments of third-generation high-energy synchrotron sources, high-strength x-ray transparent Be or composite Be + cBN gaskets, and new DAC designs have allowed a battery of x-ray spectroscopy studies under extreme P (Shen and Mao, 2017).

1. High-energy-resolution IXS for high-P phonon dispersive studies

According to linear response theory, NIXS will have peaks at the poles of the electron density response function, which occur wherever there is a collective response of the electron gas (plasmons), a response to the lattice vibrations (phonons), or a single particle response (particle-hole excitations, excitons, etc.). The field of IXS has grown very rapidly over the past decade as new instruments come online. Most importantly, its capability of measuring μm-sized crystals makes it possible to probe samples at extreme high-P environments.

Farber *et al.* (2006) determined the lattice dynamics of molybdenum at high P to 37 GPa using high-energy-resolution IXS (HERIXS) (Fig. 13). They found a significant decrease in the H-point phonon anomaly. By comparing the experimental and calculations based density functional theory (DFT), they suggested the H-point anomaly in molybdenum arose from electron-phonon coupling.

Loa *et al.* (2012) measured the phonon dispersion relationships of a high-P phase cerium-oC4 (α' phase with the α-uranium crystal structure) at 6.5 GPa using inelastic x-ray scattering. Pronounced phonon anomalies were observed, which were remarkably similar to those of α-U.

2. NRIXS for high-P phonon density of states measurements

NRIXS is a special type of IXS that uses nuclear resonant scattering from "Mössbauer" nuclei in the sample as the excitation energy. Since the intrinsic width of nuclear resonance is very sharp on the order of neV, the energy resolution for these experiments is limited only by the incident beam resolution (meV). The nuclear resonant process is incoherent; what is measured is the phonon density of states (DOS) weighted with the contribution from the resonant nuclei. From NRIXS, the partial density of states can be obtained to derive important dynamic, thermodynamic, and elastic information, such as the vibrational kinetic energy, vibrational entropy, Debye temperature, and sound velocities.

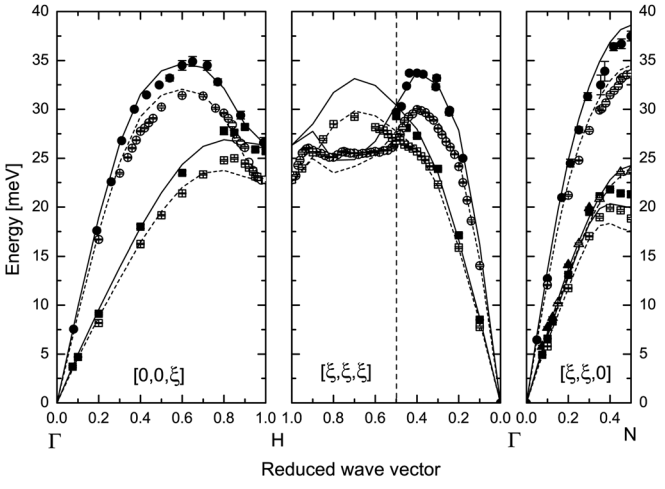

FIG. 13. Phonon dispersions in molybdenum. The filled symbols are IXS data collected at 17 GPa; the open symbols are inelastic neutron-scattering results at 1 atm. Circles are longitudinal acoustic modes and squares are transverse acoustic modes. From Farber *et al.*, 2006.

Mao *et al.* (2001) reported the phonon DOS of iron measured by NRIXS to 153 GPa (Fig. 14). From the DOS, they derived the elastic and thermodynamic parameters of iron, including the shear modulus, compressional and shear velocities, heat capacity, entropy, kinetic energy, zero-point energy, and Debye temperature. In comparison to the compressional and shear velocities from the preliminary reference Earth model, the results suggest that the Earth's inner core has a mean atomic number equal to or higher than pure iron, which is consistent with an iron-nickel alloy.

3. IXS for high-P plasmon studies

Plasmon results from a collective oscillation of the electron gas and appears as a peak in IXS measurements. For example, sodium, which has long been regarded as one of the simplest metals, displays a great deal of structural, optical, and electronic complexities under compression. Mao *et al.* (2011) compressed pure Na in the body-centered cubic (bcc) structure to 52 GPa and in the face-centered cubic (fcc) structure from 64 to 97 GPa, studying the plasmon excitations of both structures using the momentum-dependent inelastic x-ray scattering technique (Fig. 15). *Ab initio* calculations indicated that the deviation was an expected behavior of Na remaining as a simple metal.

4. X-ray Raman probes for high-P chemical bonding of low-Z elements

The K-edge spectra contain a wealth of element-specific information on chemical bonding, electron energy, and structural coordination. The K-edge energies of light elements such as H, He, C, O, Na, Mg, Al, and Si, however, are in the soft x-ray regime below 2–3 keV and are inaccessible through DAC windows. Nonresonant x-ray Raman scattering (XRS), an energy loss spectroscopy using hard x rays as a bulk sensitive probe, allows the study of low and intermediate Z elements at extreme conditions. The high-P K edge of helium (H. K. Mao *et al.*, 2010), carbon (Mao *et al.*, 2003), and oxygen (Meng *et al.*, 2004, 2008; H. K. Mao *et al.*, 2010) have been successfully measured. Lee, Eng, and Mao (2014) gave a comprehensive review of the high-P XRS applications.

A very tight collimation of the scattered beam is required to reduce background relative to the signal, particularly for the weak x-ray scatterings of light elements. Recently this problem was resolved using a polycapillary as an x-ray focusing optic (Chow *et al.*, 2015). A focusing optic was used for collection of the scattered x ray with a sizable solid angle similar to a condensing lens in the optical energy range. The focusing optic provides the desired depth resolution,

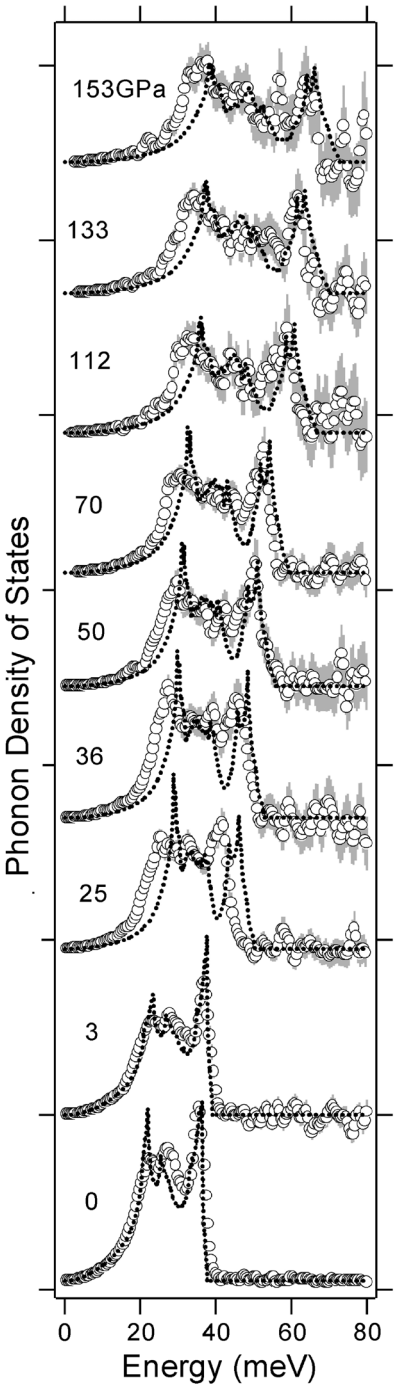

FIG. 14. The phonon density of states of iron measured using NRIXS up to 153 GPa. The circles represent the experimental data and the dashed lines are the theoretical calculations. From Mao *et al.*, 2001.

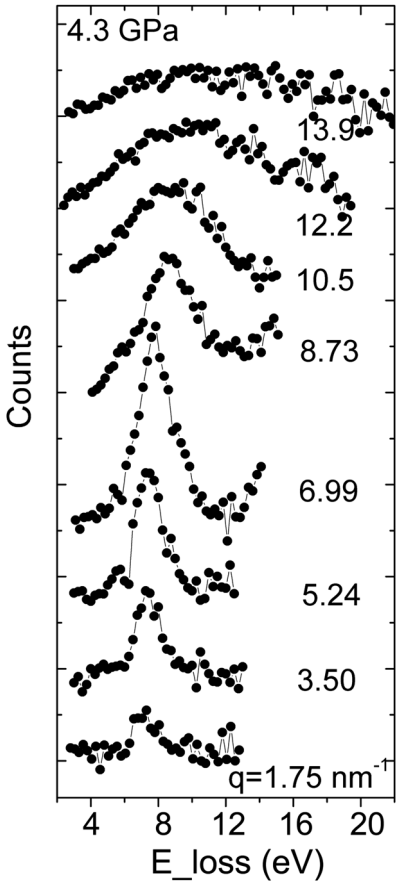

FIG. 15. IXS spectra (background subtracted) of bcc Na at 4.3 GPa with scattering angles from $2\theta = 2°$–$16°$ at a 2° increment (corresponding to $q = 1.75$ to 13.9 nm^{-1}). From Mao *et al.*, 2011.

significantly discriminating the background signals originating from materials surrounding the samples.

5. X-ray absorption near edge spectroscopy for the local electronic structure of *d* and *f* elements at high *P*

As the energies of transition-metal (TM) *K* edges ($1s$-$4p$ transition), RE, and noble metal $L_{2,3}$ edges ($2p$-$5d$ transitions) are still above 3 keV (the cutoff energy of the DAC window), conventional x-ray absorption spectroscopy, especially XANES, can be applied at high *P* to study the local electronic configuration of the probed elements. As the sample volume probed by XANES is about $\frac{4}{3}\pi r^3$ with *r* of only about 5 Å (*r* is the volume radius, while the volume center is the probing atom), it is a local probe that is insensitive to long-range ordering or environments.

Ramos *et al.* (2009) presented a XANES study to describe the local process toward the *P*-induced abrupt changes in the resistivity of Jahn-Teller (JT) distorted, doped $LaMnO_3$ compounds up to 37 GPa (Fig. 16). They identified successive steps toward the *P*-induced abrupt changes in resistivity. These steps were associated with local processes such as the opening of the interoctahedra tilt angles and the average symmetrization of the Mn local environment.

6. XES for high-*P* valence electronic band

During the XES process, a core electron is excited by the incident x ray and the core hole is filled by an electron from a valence band. Another photon is emitted whose energy equals the energy difference between the two electronic levels. XES can provide valence, spin, and bond information of the system under high *P*. Struzhkin *et al.* (2006) reported measurements of the valence-band width in compressed Ge determined from

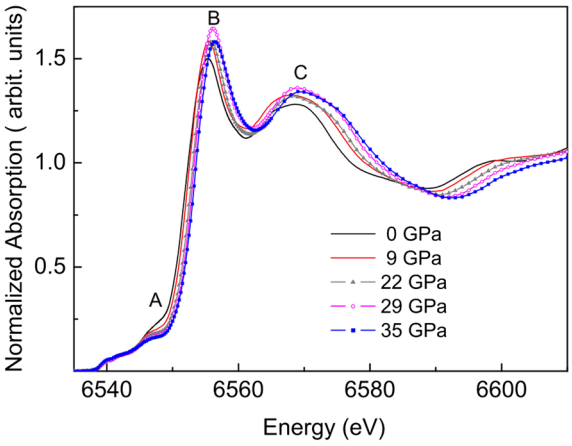

FIG. 16. Evolution of XANES features at the Mn K edge of $LaMnO_3$ for increasing P. From Ramos *et al.*, 2009.

x-ray XES below the Ge K edge (Fig. 17). The width of the valence band did not show any P dependence in the semiconducting diamond-type structure of Ge below 10 GPa. On the other hand, in the metallic α-Sn phase above 10 GPa, the valence bandwidth increased under compression. DFT calculations show an increasing valence bandwidth under compression, both in the semiconducting phase (contrary to the experiment) and in the metallic α-Sn phase of Ge (in agreement with observed P-induced broadening). The P-independent valence bandwidth in the semiconducting phase of Ge appears to require theoretical advances beyond the DFT or GW approximation.

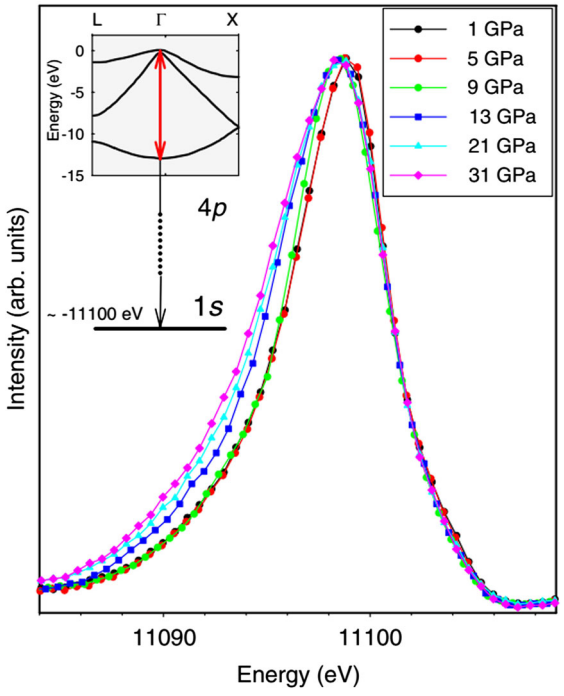

FIG. 17. Valence-band emission spectra in Ge at selected P. Emission spectra at 1, 5, and 9 GPa were collected from the semiconducting diamond-type phase and have nearly identical line shapes, while the spectra at 13, 21, and 31 GPa from the metallic β-Sn phase demonstrate an increasing linewidth under P. From Struzhkin *et al.*, 2006.

7. Resonant XES for high-P local electronic structure of d and f elements

Using the same experimental setup as XES, RXES and partial fluorescence yield x-ray absorption spectroscopy experiments can be performed by scanning incident x-ray energies across the absorption edge. During RXES experiments, XES are collected for different selected incident energies near an absorption edge. RXES studies of transition-metal and rare-earth systems give important information on the electronic states of the sample, such as the intra-atomic multiplet coupling, electron correlation, and interatomic hybridization. Ding *et al.* (2012) demonstrated a strong dependence of high-resolution $1s$-$3p$ (or $K\beta$) RXES on local spin correlations at high P. They showed that the pre-edge region in $K\beta$ RXES of CoO could be separated into a local quadrupolar contribution and nonlocal dipolar intensity, which arises from the mixing of the cobalt $4p$ states with their neighboring cobalt $3d$ orbitals. For P below 12 GPa, they observed a twofold increase in the nonlocal contributions with respect to the local contributions. For P greater than 12 GPa, the ratio remained nearly constant. The observed P dependence and strong intensity changes cannot be explained by conventional bond-length shortening and were instead ascribed to increased intersite $4p$-$3d$ mixing due to changes in the magnetic ordering (Fig. 18).

8. XES probes for local spin moment and spin-pairing transition in transition elements

The emission spectra of most $3d$ transition elements with partially filled d orbitals are characterized by a main peak and a satellite peak located at lower energy, due to the $3p$-core and

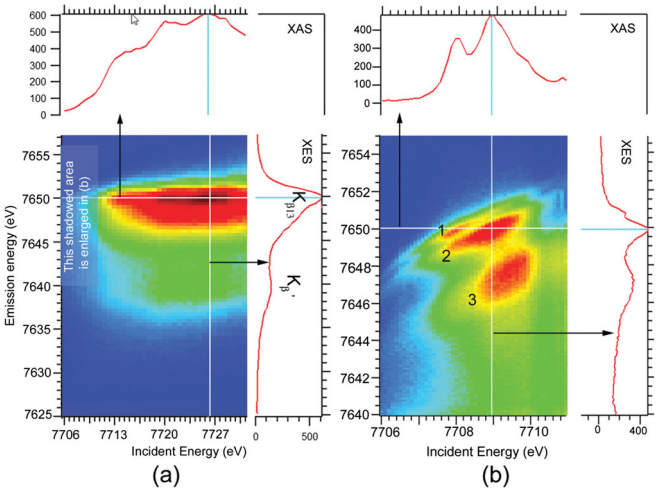

FIG. 18. High-P $1s$-$3p$ RXES map of CoO at 12 GPa. (a) The RXES map was created at emission energies ranging from 7625 to 7657 eV and incident energies ranging from 7706 to 7713 eV. (b) The enlarged REXS map from (a) at emission energies ranging from 7640 to 7654 eV and incident energies ranging from 7706 to 7711 eV. The line spectra in (a) and (b) at the top represent the partial yield fluoresce x-ray-absorption spectrum, while the spectra on the left are emission spectra. The three peaks labeled 1, 2, and 3 show the Raman shift due to resonance effects. From Ding *et al.*, 2012.

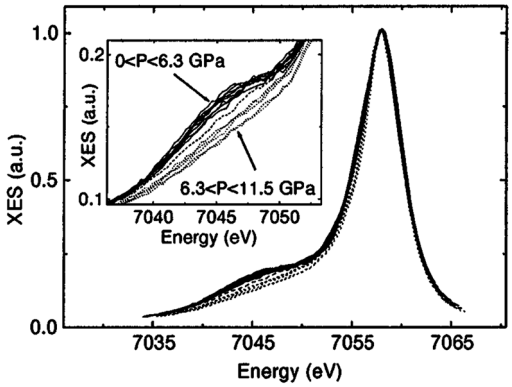

FIG. 19. The XES spectra of FeS at high P. The dashed line shows an intermediate spectrum obtained on decompression at 6.1 GPa. The sequence of P was 1.25, 2.0, 2.7, 3.5, 6.3, 7.5, 10.0, 11.5, 8.2, 6.9, 6.1, 5.2, 1.4, and 0.2 GPa. From Rueff *et al.*, 1999.

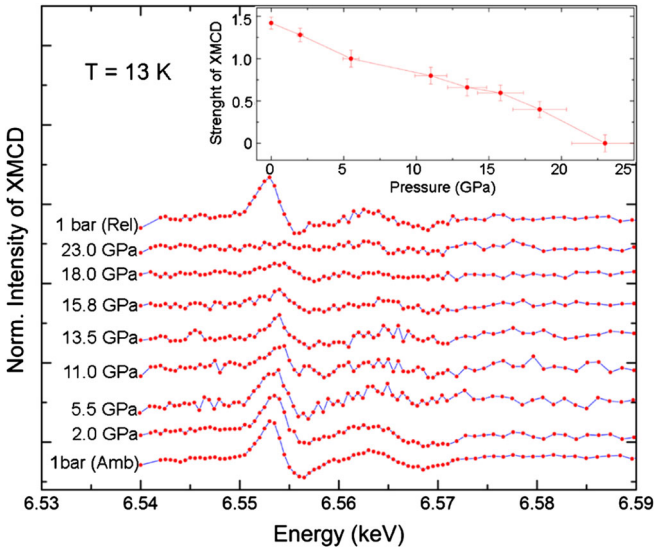

FIG. 20. Normalized XMCD data of $La_{0.75}Ca_{0.25}MnO_3$ collected at 13 K from 1 bar to 23.0 GPa. The inset shows the intensity of the overall XMCD strength vs P. 1 bar (Amb) and 1 bar (Rel) are ambient spectra taken before compression and after P release, respectively. From Ding *et al.*, 2009.

$3d$-hole exchange interaction in the emission final state. The intensity of the satellite and the energy splitting between the main peak and the satellite are proportional to the local spin moment of the element. Rueff *et al.* (1999) reported a P-induced high-spin to low-spin transition in FeS using XES techniques. The transition was evidenced by the disappearance of the low-energy satellite in the Fe $K\beta$ emission spectrum of FeS (Fig. 19). Since then, XES has been used as a standard tool to study the local moment and spin-pairing transition.

9. X-ray magnetic circular dichroism for long-range ferromagnetic moment

XMCD is a powerful technique for studying the magnetic states in strongly correlated electron systems. With an external magnetic field and circularly polarized x ray, XMCD is based on XAS and provides element- and orbital-specific information about the probed materials. In the hard x-ray region, DACs coupled with high-P XAS experiments can also be used for XMCD studies of the K edge ($1s$-$4p$ transition) of transition metals, and the $L_{2,3}$ edges ($2p$-$5d$ transitions) of rare-earth elements. The dichroic spectrum originates from the delocalized $4p$ or $5d$ electronic states hybridized with the localized $3d$ or $4f$ states, so the spectral intensity is usually very weak compared with that from the $L_{2,3}$ edges ($2p$-$3d$) and $M_{4,5}$ edges ($3d$-$4f$) in the soft x-ray region.

Ding *et al.* (2009) carried out low-temperature Mn K-edge XMCD and XRD measurements to investigate the stability of the ferromagnetic (FM) ground state in manganite $La_{0.75}Ca_{0.25}MnO_3$ under quasihydrostatic compression. The magnetic dichroism signal gradually decreases with P and disappears at 23 GPa (Fig. 20). These changes are attributed to a ferromagnetic-antiferromagnetic (FM-AF) transition, which is associated with orbital ordering at high P.

10. High-P magnetism probed by NRFS

NRFS measures the hyperfine splitting reconstructed from the time-dependent intensity of a conventional Mössbauer spectrum, which provides valuable information about oxidation states, magnetism, and the site occupancy of isotope enriched elements, i.e., Fe^{57} under extreme conditions. For example, Jackson *et al.* (2005) measured two silicate perovskite samples $Fe_{0.05}Mg_{0.95}SiO_3$ (Pv05) and $Fe_{0.1}Mg_{0.9}SiO_3$ (Pv10), up to 120 and 75 GPa, respectively. The results are explained in the framework of the "three-doublet" model, which assumes two Fe^{2+}-like sites and one Fe^{3+}-like site are well distinguished by the hyperfine fields at the location of the Fe nuclei (Fig. 21).

NRFS is also called synchrotron Mössbauer spectroscopy. Unlike the conventional, laboratory-based, energy-domain Mössbauer spectroscopy, the signal from synchrotron NRFS is generated in the time domain due to the quantum beats interference. Potapkin *et al.* (2012) established an energy-domain SMS facility at the European Synchrotron Radiation Facility based on a nuclear resonant monochromator employing the pure nuclear reflections of an iron borate ($^{57}FeBO_3$) crystal.

11. Resonant IXS probes for low-energy excitations at high P

Hard x-ray RIXS can measure the energy, momentum, and polarization changes of the scattered photon. These changes are transferred to the intrinsic excitations of the material under study. In RIXS, the incident photon energy is chosen to coincide with, and hence resonate with, one of the atomic x-ray transitions of the system. The resonance can greatly enhance the inelastic scattering cross section, sometimes by many orders of magnitude, and offers a unique way to probe the charge, magnetic, and orbital degrees of freedom of selected atomic species in a crystal (Ament *et al.*, 2011). The elementary excitation spectrum in solids spans the range from plasmons and charge-transfer excitations at a few eV, determining, for instance, the optical properties, through excitons, dd excitations, and magnons down to phonons at the meV scale. In principle, RIXS can measure

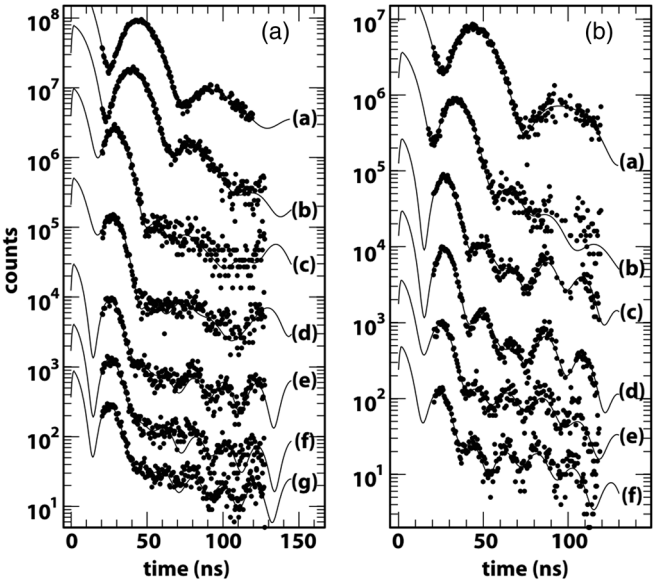

FIG. 21. (a) The SMS time spectra (filled circles) and calculations with the best-fit parameters (solid lines) for $Fe_{0.05}Mg_{0.95}SiO_3$ at the following P: (a)–(g) ambient, 5, 40, 60, 85, 100, and 120 GPa. The vertical axes represent intensity. (b) The SMS time spectra and calculations with the best-fit parameters for $Fe_{0.1}Mg_{0.9}SiO_3$ (a)–(f) at 3, 23, 42, 55, 65, and 75 GPa. From Jackson *et al.*, 2005.

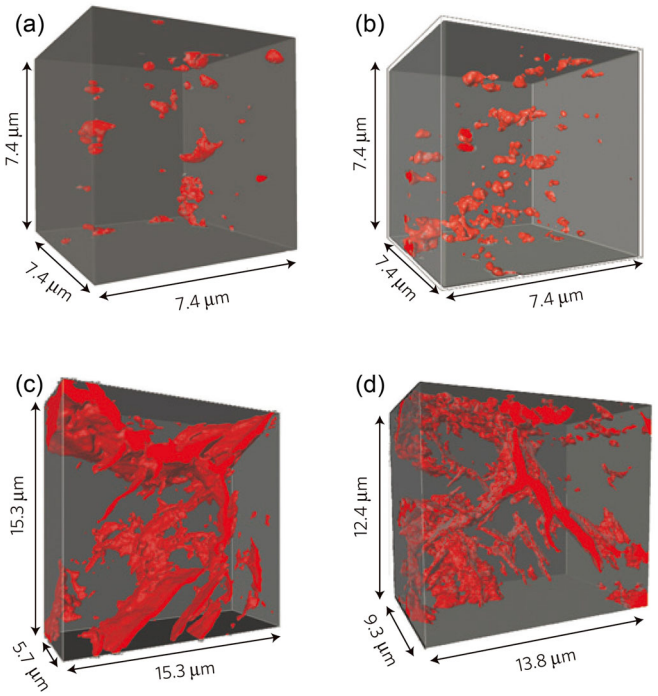

FIG. 22. 3D distribution of iron alloy melt in silicate perovskite. (a) Samples were synthesized at 25 GPa, (b) 39 GPa, (c) 52 GPa, and (d) 64 GPa. From Shi *et al.*, 2013.

the momentum dependence of the excitation energy of all these modes, i.e., their dispersion, because the photon transfers momentum as well as energy to the material under study (Ament *et al.*, 2011).

Recently the DAC has been coupled with RIXS techniques to study charge excitations, such as the crystal field excitation, the Mott gap excitation, the charge-transfer excitation, and the spin-orbiton excitation in the valence band of $FeBO_3$ (Kim *et al.*, 2014) and $Sr_3Ir_2O_7$ (Ding *et al.*, 2016) at high P up to 60–70 GPa, demonstrating the RIXS techniques as a promising new tool in high-P science.

F. High-*P* x-ray tomography

XRD is an accurate technique for volume determination of crystalline materials at high P, but does not give a unique, accurate measurement of volume for amorphous or liquid materials because the amorphous diffraction peaks are very broad and their relations to the volume are undefined. To overcome this problem, measuring the volume directly using x-ray imaging and tomography is a promising technique. The synchrotron-based transmission x-ray microscope (TXM) can visualize the shape, size, and composition of three-dimensional objects inside the DAC. Resolutions of tens of nanometers make this technique exceptionally powerful at very high P, where the sample dimensions could be as small as a few μm.

By applying high-P TXM tomography measurements to metallic glasses, Zeng *et al.* (2014, 2016) studied the relationship between the macroscopic density determined from TXM and the average interatomic spacing estimated from a diffraction method. The results show that the volume of metallic glasses varies with P by 5/2 power of the principal diffraction peak position, instead of the cubic power that is observed in crystalline and gas or liquid systems.

In another example, Shi *et al.* (2013) successfully used TXM to visualize the interconnected liquid iron alloy melt network within silicate perovskite grain boundaries at P above 50 GPa. A mixture of enstatite and iron-nickel-sulfur alloy was compressed in a DAC from 25 to 64 GPa at temperatures ranging from 2300 to 3300 K and then quenched rapidly to freeze its texture (Fig. 22).

The spatial resolution of TXM is determined by the focusing zone plate as an objective. The current technology fabricates high aspect ratio fine zones to set the limit of the TXM resolution to a few tens of nanometers. X-ray coherent diffractive imaging (a lenseless microscope, which is not limited by any x-ray optics such as a zone plate) can achieve a better spatial resolution than full field x-ray microscopy techniques.

Yang *et al.* (2013) applied a mutual coherent function method in Bragg coherent diffractive imaging to investigate the 3D evolution of the morphology and internal strain of a 400 nm gold single crystal under P up to 6.4 GPa. Diffraction patterns collected in different angles in the vicinity of the Bragg peaks were transformed into real space information by algorithms. The contribution from the gasket and medium were deconvoluted during computation. With additional constraints, phases that are attributed to lattice distortions were retrieved with a sensitivity of 0.01%.

G. High-*P* neutron diffraction

Neutrons have their own spin and can interact directly with nuclei with a scattering intensity that is (scattering factor)

independent of the atomic number (Z) but varies with isotopes of the same elements. Moreover, neutron-scattering factors do not decrease with scattering angles, so a greater reciprocal space can be probed. These characteristics allow neutron diffraction to probe the structures and magnetic orderings of crystalline and amorphous materials with very light elements (e.g., H, Li, and B) and heavy elements (e.g., Ta, U, and Pu), which are difficult to investigate using XRD techniques. The high penetrating power of neutrons present great advantages in designing P cells, which realize their full potential in a broad spectrum of scientific problems. However, as the flux of the neutron source is much lower and more difficult to focus compared to synchrotron x-ray, neutron studies require a large sample (e.g., mm size) to obtain acceptable signal statistics. Recently, the neutron inelastic scattering technique has been also applied at high P to spin resonance and phonon dispersive study.

1. *P*-induced network changes

Zeidler *et al.* (2014) performed *in situ* high-P neutron diffraction on SiO_2 up to 17.5 GPa and molecular dynamics simulations employing a many-body interatomic potential model to investigate the structure of cold-compressed silica glass. On the basis of the molecular dynamics results, an atomistic model for densification was proposed where rings are "zipped" by a pairing of fivefold and/or sixfold coordinated Si sites. The model gives an accurate description of the mean primitive ring size dependence on the mean Si-O coordination number, thereby linking a parameter that is sensitive to ordering on multiple length scales to a readily measurable parameter that describes the local coordination environment.

2. *P*-induced magnetic ordering

The 3d transition-metal oxides belong to electron-correlated systems. Their structure and properties are complicated by the interactions of the charge, spin, lattice, and orbital moment in the system. For example, FeO and CoO are paramagnetic insulators with a rock salt structure above their Néel temperatures (T_N) of 198 and 290 K, respectively. Below T_N, they transform into AF states. CoO distorts into a tetragonal symmetry, accompanied by a small rhombohedral distortion, whereas FeO distorts into a rhombohedral structure. These distortions are due to magnetoelastic coupling. Upon compression at room T, FeO and CoO were observed to distort into rhombohedral structures at ~15 GPa (Ding *et al.*, 2005) and 43 GPa (Guo *et al.*, 2002), respectively. Based on the linear P dependence of T_N and its similarity to lattice distortion at low temperature, it was predicted that the rhombohedral lattice distortion in FeO at ~15 GPa should be associated with a magnetic ordering transition due to magnetoelastic coupling (Yagi, Suzuki, and Akimoto, 1985), as it occurs at low T. However, diffraction measurements applied to FeO and CoO (Ding *et al.*, 2005) found no magnetic ordering accompanying the structure distortion of FeO at high P up to 20 GPa; while in CoO, the magnetic ordering transition started around 2 GPa (Ding *et al.*, 2006), far below the structure distortion around 43 GPa. These results indicate their structure distortions are not related to a magnetic ordering transition.

Another example is that Zhou *et al.* (2011) mapped the P-T phase diagram for both the crystal and magnetic structures of $LaCrO_3$ perovskite using *in situ* neutron diffraction under P. The system offers an opportunity to study the evolution of the magnetic order, spin direction, and magnetic moment on crossing the orthorhombic-rhombohedral phase boundary. Moreover, they also developed a microscopic model of their superexchange interaction on the basis of the crystal structure, accounting for the behavior of T_N under high P.

3. High-*P* study of spin glass

Apetrei *et al.* (2007) presented a comparative study of $(Tb_{0.8}La_{0.2})_2Mo_2O_7$ and $Gd_2Mo_2O_7$ situated at the verge of a Mott transition from a FM metal to insulating spin glass; both compounds transformed into a spin glass state at high P. Under P, the lengths scale of the mesoscopic correlations was strongly reduced, whereas the short-range correlations were unchanged.

4. Hydrogen position in light-elemental systems

Clathrate hydrates are icelike crystalline solids with guest molecules encapsulated in the frameworks bonded by water molecules and are typically stable at high-P and/or low-T conditions.

Using high-P Raman, infrared, x-ray, and neutron studies Mao *et al.* (2002) showed that H_2 and H_2O mixtures crystallize into the sII clathrate structure with an approximate H_2/H_2O molar ratio of 1:2. The clathrate cages were multiple occupied by H_2 molecules.

Lokshin *et al.* (2004) also used neutron diffraction to determine the D_2 clathrate hydrate crystal structure. They found that the hydrogen occupancy in the D_2 clathrate could be reversibly varied by changing the large (hexakaidecahedral) cage occupancy between two and four molecules, while maintaining single occupancy of the small (dodecahedral) cage. They also observed that above 130–160 K, the guest D_2 molecules were in a delocalized state, rotating around the centers of the cages. A decrease of temperature resulted in rotation freezing, followed by complete localization below 50 K.

Boehler *et al.* (2013) designed new strongly supported conical diamond anvils for neutron diffraction and reached 94 GPa with a sample volume of $\sim 2 \times 10^{-2}$ mm^3, a 100-fold increase. This sample volume was sufficient to measure the full neutron diffraction patterns of D_2O–ice at this P, at the high flux spallation neutrons and pressure beam line in Oak Ridge National Laboratory. This study provides an almost fourfold extension of the previous P regime for such measurements.

5. High-*P* study of phonon dispersion

Klotz (2001) made great progress in high-P inelastic neutron scattering techniques, allowing the measurement of phonon dispersion to ~12 GPa on triple axis spectrometers. By applying high-P inelastic neutron scattering techniques, they studied the P-induced frequency shifts of the acoustic

branches of a number of "simple" systems (Ge, GaSb, PbTe, FeO, Zn, and Fe). Several of these solids showed pronounced "mode softening" under *P*.

6. High-*P* study of spin resonance

Pratt *et al.* (2009) applied inelastic neutron-scattering measurements to $CaFe_2As_2$ under applied hydrostatic *P* to show that the AF spin fluctuations observed in the ambient *P*, paramagnetic, and tetragonal phases are strongly suppressed in the collapsed tetragonal phase. These results are consistent with a quenched Fe moment in the collapsed tetragonal phase and the strong decrease in resistivity observed upon crossing the boundary from the tetragonal to the collapsed tetragonal phases.

Marty *et al.* (2012) carried out a high-*P* study of the unconventional superconductor $FeTe_{0.6}Se_{0.4}$ up to 1.5 GPa with neutron scattering, resistivity, and magnetic susceptibility measurements. The neutron spin resonance energy and the superconducting transition *T* were extracted as a function of applied *P* in samples obtained from the same crystal. Both increased with *P* up to a maximum around 1.3 GPa, directly demonstrating a correlation between these two fundamental parameters of unconventional superconductivity.

Nevertheless, comparatively large sample volumes are still required in neutron-scattering measurements at high *P*.

H. High-*P* electromagnetic transport probes

1. Resistivity measurement in DAC

High-*P* electrical transport properties are important in condensed-matter physics research, materials science, chemistry, and Earth science. The early four-probe resistivity technique was developed by Mao and Bell (1981), where thin metallic wires were aligned in the sample chamber of the DAC as probes to contact the sample. Soft powder such as NaCl was used as a *P* medium. van der Pauw methods can be used to determine the resistivity, based on the data obtained from the four-probe measurements. This method was often used for measuring the resistance of inorganic or bulk samples.

For an accurate determination of the resistivity, a method based on a single crystal was developed (Adachi *et al.*, 2001), allowing better *P* media than NaCl to be chosen. Resistance measurements prove challenging because of the shearing stresses in the DAC, such as metal probes breaking at the edge of the diamond anvil and/or leads short circuiting due to increased width under *P* and plastic flow. Grzybowski and Ruoff (1984) applied a metal film circuit directly onto a diamond anvil, where a solid *P* medium locked the sample in place, in electrical contact with the leads. A combination of thin-film fabricating and photolithography techniques was adopted to further improve the method (Grzybowski and Ruoff, 1984; Hemmes *et al.*, 1989); the shape and position of these thin-film probes can be designed according to experimental requirements and remain unchanged during compression. Rotundu *et al.* (2013) designed beveled diamonds with FIB conductive depositions that survived *P* in excess of 200 GPa.

To overcome the difficulty of arranging the small sample and improve the endurance of the electrodes during compression, an alternative way to perform resistance measurements is to use lithographically designed electrical leads on the diamond anvils (Gao *et al.*, 2005). Molybdenum is usually deposited as a conductor onto a diamond anvil. A layer of Al_2O_3 film is fabricated onto the Mo-coated layer for insulation. The regular shape of the microelectric circuit was fabricated by using this photolithography technique (Hemmes *et al.*, 1989). Recently, an improved method with FIB conductive depositions was developed (Rotundu *et al.*, 2013), which can meet the requirements of a gaseous *P* transmitting medium. The samples were attached to the flat tip of the diamond using FIB ultrathin lithographic deposited Pt-based leads, which were typically 5 nm thick. The inner terminal of these leads passed over the sample, ensuring the electrical contact and rigid attachment of the sample to the diamond. Meanwhile, four microelectrodes with thin laser-cut platinum were displayed in a radial position to connect the FIB probes at the edge of the diamond culet to complete the connection from the sample to the outside electrodes. In this way, the DAC can be closed in precompressed gas using a gas loading system.

2. Magnetic susceptibility measurement in DAC

The magnetic susceptibility technique is an inductive method that does not require physical contact with the sample. A single frequency standard technique used at ambient *P* has been adapted for DAC experiments. This technique is capable of detecting signals from the samples at *P* below 50 GPa; because it is necessary to reduce the diameter of the diamond anvil culets used to reach high *P*, the sample signal is also reduced. Such small sample signals are very difficult to detect as they are minute in comparison to the background. Several other techniques have been developed to reduce the background signal in single frequency techniques. These include the third harmonic method (Raphael, Reeves, and Skelton, 1998) and the vibrating magnetometer technique (Ishizuka, Amaya, and Endo, 1995). The latter has been used to detect superconductivity in vanadium to 120 GPa with a record high $T_c = 17.2$ K.

The double frequency modulation method was introduced by Timofeev *et al.* (2002) and developed to detect both the superconducting transition and the magnetic transition in ferromagnets. This technique has been used to reach the highest *P* of 230 GPa and holds the record for high-*P* magnetic susceptibility measurements on superconductors.

Recently a DAC with a small diameter (<9 mm) was designed to fit in the bore of the quantum design's magnetic properties measurement system (MPMS) magnetometer. The superconducting transition at a record high of 203 K was detected in the H-S system based on this method (Drozdov *et al.*, 2015).

IV. ATOMIC STRUCTURES UNDER COMPRESSION

The structural arrangements of atoms dictate all other materials properties. From a structural perspective (Wang and Fernandez-Martinez, 2012), condensed matter can be

categorized into crystalline (with periodic translational symmetry), amorphous (no periodic and orientational symmetry), quasicrystalline (with orientational but not periodic translation symmetry), and "amorphous crystalline" (crystalline materials containing amorphous building blocks). P is a powerful variable that can smoothly tune or radically change all structural parameters, including the atomic positions, coordination, symmetry, periodicity, and ordering in crystalline or amorphous materials. Numerous polymorphic crystalline phase transitions, amorphization (Mishima, Calvert, and Whalley, 1984; Hemley *et al.*, 1988; Wang *et al.*, 2012; Lv *et al.*, 2013), devitrification (Zeng *et al.*, 2009, 2010), and polyamorphism (Sheng *et al.*, 2007) have been discovered at high P. Combining P with nanocrystallinity results in different phase transition sequences (Wang *et al.*, 2010) and rheological behaviors (Chen *et al.*, 2012; B. Chen *et al.*, 2014) from bulk samples.

A. Crystallographic complexity at high P

Conventional wisdom assumed that compression led to the increasing coordination of hard-sphere atoms, and greatly simplified structures. This implies that elements made of identical atoms would all turn into fcc or hexagonal-close-packed (hcp) crystals. This perception changed dramatically around the turn of the century. New theories and experiments have now demonstrated that crystallography is far more intricate and rich at high P. Indeed, P always improves the packing efficiency. However, P forces atoms to interact with one another, which greatly enhances the nonspherical nature of the atoms. Close packing of nonspherical irregularly shaped atoms with interactive electrons is very complicated. For instance, at increasing P the simple s-p element Ca goes through the transition sequence of 12-coordinated fcc to 8-coordinated bcc to 6-coordinated simple cubic (sc) structures, completely opposite to conventional wisdom. High-P single-crystal XRD shows that Ca-III is not exactly sc, but sustains the sc-like primitive unit by a rhombohedral distortion at 300 K and a monoclinic distortion below 30 K. The high-P phase is dictated by high-T anharmonicity and low-T metastability fine-tuned with phonon stability at the local minimum (W. L. Mao *et al.*, 2010). In a small-T range below 10 K (Li *et al.*, 2012), β-tin structured calcium was observed with $I4_1/amd$ symmetry at 35 GPa. This experimental observation established a new phase diagram for calcium up to 110 GPa and 5–300 K (Fig. 23).

At higher P, Ca crystallizes into a long chain and incommensurate structure (W. L. Mao *et al.*, 2010; Nakamoto *et al.*, 2010). At ambient P, uranium is the only element with an exotic incommensurate structure, but more than a dozen elements (McMahon and Ackland, 2010) become incommensurate at high P and the number is increasing with more investigations.

The pioneering high P-T study of Na led to the discovery of its room T melting at 118 GPa (Gregoryanz *et al.*, 2005). The extended studies (Gregoryanz *et al.*, 2008) to 130 GPa display myriad (>10) high-P crystalline solid phase changes in Na; many of them have altogether new crystal structures, including exotic unit cells containing up to 512 atoms for such a simple element (Fig. 24). High-P studies of elemental Li revealed seven complex structures and a record low high-P melting minimum at 200 K and 40 GPa (Guillaume *et al.*, 2011). Li showed a melting maximum in the melting lines and that melting line decline extended to well below room temperature to 200 K.

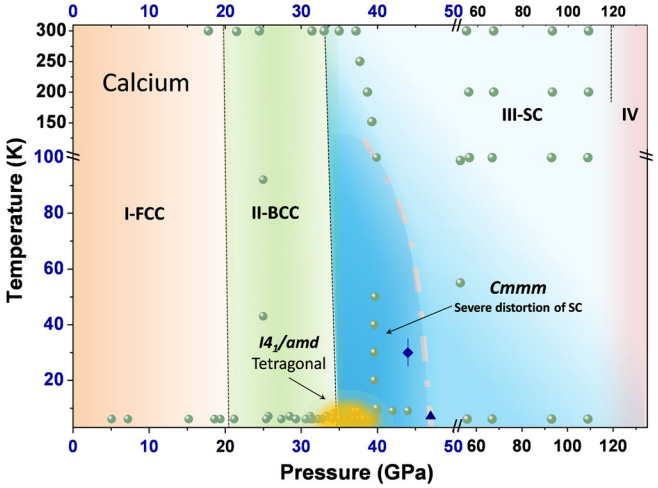

FIG. 23. High-P, low-T phase diagram of elemental Ca. From Li *et al.*, 2012.

B. P-induced amorphization and nanosize effect

Amorphous solids are usually produced by fast cooling the melt to T below the glass transition avoiding crystallization. However, P can also be used to make amorphous materials through a P-induced amorphization (PIA) process. PIA was

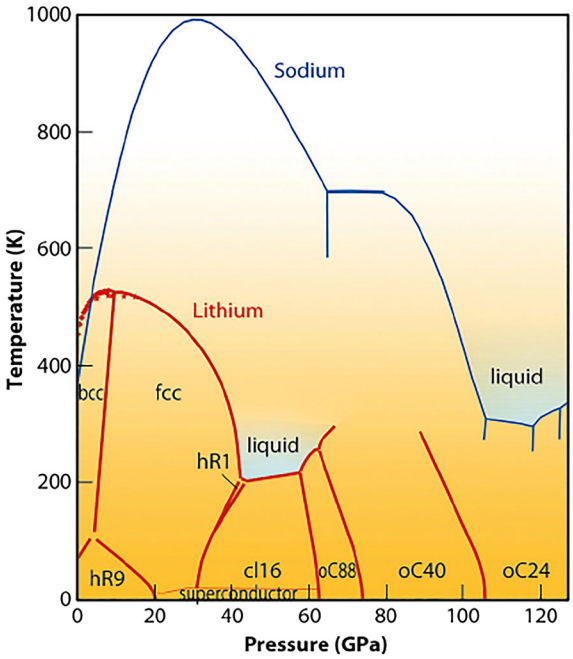

FIG. 24. Phase diagrams of lithium and sodium showing that the two elements have similar high-P polymorphism. From Gregoryanz *et al.*, 2008 and Guillaume *et al.*, 2011.

first discovered by pressurizing ice I at 77 K to its metastable melting P of 1 GPa (Mishima, Calvert, and Whalley, 1984). Hemley *et al.* (1988) found that silica underwent an irreversible crystalline to amorphous transition at high P by using Raman and energy dispersive XRD. Since then, PIA has become the subject of intense studies, and many elements and compounds, including organic materials, have been found to have PIA transitions. Although the recent study reported by Hu *et al.* (2015) using new generation synchrotron techniques suggested that the XRD peaks broadening used as a criteria for PIA in coesite (Hemley *et al.*, 1988) might be due to the emergence of multiple new diffraction peaks in the crystalline-crystalline transitions, most PIAs reported during the last three decades are truly crystalline-amorphous transitions.

Using high-P indentation, silicon crystals were found to undergo a crystalline to amorphous transition during rapid unloading (Ruffell, Bradby, and Williams, 2006). This amorphization was size dependent (Mann *et al.*, 2000). Different amorphous structures have been induced in monocrystalline silicon by high-P indentation and polishing. High-resolution transmission electron microscopy and nanodiffraction found that the structures of amorphous silicon that form at relatively slow and fast loading and unloading rates are dissimilar and inherit the nearest-neighbor distance of the crystal in which they are formed (Jang *et al.*, 2005). Such kinds of amorphization have also been found for silicon nitride, germanium, and other materials (Jang *et al.*, 2005).

The nanosize effect can promote PIA in poor glass formers, such as TiO_2 and Y_2O_3 (Swamy *et al.*, 2006; Wang *et al.*, 2010). Molecular crystals made of large clusters, such as fullerenes, have also been found to have PIA due to the P-induced collapse of their building blocks (Sundqvist, 1999). Pure fcc C_{60} crystals transform into sc structures at 0.2 GPa and then turn amorphous at 26 GPa. The Raman spectra of decompressed samples indicate that the bulky ball is retained at low P but starts to collapse at P higher than 26 GPa, suggesting the PIA is attributed to the P-induced crushing of the carbon cages. C_{70} crystals also show similar P behavior. However, studies on solvated fullerenes showed that the long-range order can be preserved even though the individual cages are crushed and become amorphous (Wang *et al.*, 2012).

P was found to induce amorphization in Ta_2O_5 nanowires, which showed significant improvement in electrical conductivity. The pair distribution functions measured by XRD, together with Raman spectroscopy, transmission electron microscopy, and first-principle calculations, suggested that the amorphization is initiated by a disruption of connectivity between polyhedra at the weak-bonding positions along the a axis (Lv *et al.*, 2013).

C. *P*-induced devitrification

High P can also promote the devitrification of amorphous materials. For example, amorphous ice can easily transform into a crystalline phase under further compression (Hemley, 2000). P-induced devitrification has also been discovered in metallic glasses. Zeng *et al.* (2009, 2010, 2011) investigated the polymorphism of $Ce_{75}Al_{25}$ metallic glass using the DAC and x-ray diffraction. Surprisingly, $Ce_{75}Al_{25}$ metallic glass devitrifies into an fcc structure. Further studies suggest that the $4f$ electrons of Ce are localized at high P and bring Ce and Al into compliance with the Hume-Rothery rules for the formation of the fcc alloy (Zeng *et al.*, 2010). Even more surprisingly, Zeng *et al.* (2011) observed a P-induced devitrification where every portion of a cm-sized $Ce_{75}Al_{25}$ metallic glass ribbon crystallized independently with an identical orientation to form a giant fcc single crystal, suggesting the presence of incipient topological long-range ordering in the glass.

D. *P*-induced polyamorphism and liquid-liquid transition

P is an effective thermodynamic variable to induce polyamorphism, which is a transition between different amorphous states observed in several types of amorphous materials. Amorphous ice, silica, and chalcogenide glasses share the common trait that their constituent atoms with preferred bonding geometries would change under P and lead to polyamorphism. Metallic glasses are formed from close packing of only metallic atoms. Sheng *et al.* (2007) investigations of $Ce_{55}Al_{45}$ metallic glass resulted in the first observation of a P-induced transition between two distinct amorphous polymorphs in metallic glass. The large density difference observed between the two polymorphs was attributed to their different electronic and atomic structures. The observation of a liquid-liquid transition in a material having two distinct liquid phases of differing density is experimentally challenging and requires simultaneous high-P and high-T conditions and an instantaneous capture of the diffuse scattering from both liquid phases (Cadien *et al.*, 2013).

Recently Cunsolo *et al.* (2015) probed the dynamical signatures associated with the polyamorphic transition in amorphous GeO_2 at high P using the newly developed THz spectrum technique based on inelastic x-ray scattering and first-principle lattice dynamics calculations. The evolution of the THz spectrum of density fluctuations in the sample as a function of P was investigated. A clear transformation in the Q-dispersion behavior upon the polyamorphic transition was observed. Based on DFT calculations, the change was interpreted as the abrupt evolution from a quartzlike to a rutilelike behavior of amorphous GeO_2 and indicated that the collective dynamics of amorphous GeO_2 in the THz range was strongly sensitive to the changes in the local structure. The investigations of the THz dynamics provide an important insight into the polyamorphic transition and link it to the transformations of elastic properties (Cunsolo *et al.*, 2015).

V. SIMPLE 1*s* ELECTRON SYSTEMS UNDER COMPRESSION

A. The quest for metallic hydrogen

As the first and most abundant element in the Universe, hydrogen research has been leading the advancement of modern science and development of new energy applications. Wigner and Huntington (1935) predicted that under sufficiently high P condensed hydrogen molecules would eventually dissociate into atoms. With a single electron forming a half-filled valance band, the dense atomic phase would be an alkali metal. Ashcroft (1968) further predicted that metallic

hydrogen could be a very high-temperature superconductor. These potentials led to the quest for metallic hydrogen and intense experimental and theoretical investigations of high-P hydrogen. Compressing solid hydrogen up to 12-fold at 300 GPa, Mao and Hemley (1994) summarized numerous astonishing and unexpected high-P phenomena. Searching for the metallic state in hydrogen has been the main driving force behind relentless technological developments in the high-P sciences over the decades (McMahon *et al.*, 2012).

Extensive efforts have also been devoted to warm liquid metallic hydrogen in the high-temperature and high-P regime of the phase diagram. Weir, Mitchaell, and Nellis (1996) were the first to report an observation of metallic conductivity in warm liquid hydrogen in a shock experiment at 140 GPa. Evidence for liquid metallic deuterium from reflectance measurements was followed by a number of shock experiments (Collins *et al.*, 1998; Loubeyre *et al.*, 2012; Knudson *et al.*, 2015). Zaghoo, Salamat, and Silvera (2016) also reported a phase transition to warm liquid metallic hydrogen by a laser-heating experiment. A spectroscopy experiment by McWilliams *et al.* (2016) cautions the claim of a metallic state from the analysis of reflectance data for warm liquid hydrogen.

Metallization of hydrogen at low T has been reported previously by Mao and Hemley (1989) and Dias and Silvera (2017). Both claims were based on the observed opacity and reflectivity of the samples and both suffered from the absence of a verifiable P determination. Mao and Hemley (1989) reported that at 77 K and above 250–300 GPa hydrogen mixed with ruby grains turned opaque and interperated it as a band-gap closure of hydrogen. The peak P was beyond the useful range of the ruby scale and the claimed P was estimated based on the measurable ruby always from the maximum. Recently Dias and Silvera (2017) reported the observation of hydrogen compressed between two Al_2O_3 coated diamond anvils changing from a transparent solid to a reflective metal at a claimed high P of 495 GPa at low T. Claiming P much higher than the present limit of beveled anvils requires a convincing P calibration measurement. Dias and Silvera (2017) published the Raman spectra of diamond for P calibration; however, the spectra showed an independent peak, rather than a plateau edge as described in Sec. II.C.3. It is obviously not from the tip of a diamond and cannot be used to infer P. They also showed linear extrapolation of a load versus P relation up to 495 GPa (Liu, Dalladay-Simpson *et al.*, 2017; Silvera and Dias, 2017), which conflicts with the well-established S-shaped load versus P relationship (Fig. 6). Estimation based on their S-shaped curve would yield a P significantly less than 300 GPa.

It is also necessary to demonstrate that the opaque and reflective sample was indeed hydrogen (Liu, Dalladay-Simpson *et al.*, 2017; Silvera and Dias, 2017). There are numerous scenarios and common pitfalls where the hydrogen sample could have been lost or altered during the experiment. For instance, Ruoff and Vanderborgh (1991) raised the possibility that the opaque and reflective sample in the Mao and Hemley (1989) experiment was metallic Al produced by the hydrogen reduction of Al_2O_3 (ruby). The same criticism is equally applicable to Dias and Silvera's most recent work in which the diamond anvils were coated with Al_2O_3. In addition, the frequently occurring failure of losing hydrogen and the intrusion of the metallic gasket into the sample chamber will also produce images identical to these presented as metallic hydrogen by Dias and Silvera. On the other hand, Mao and Hemley's experiment was free from this scenario by showing the opaque hydrogen in between the ruby grains. Valid pressure determination and sample verification are necessary to demonstrate the metallization of hydrogen.

B. The rich high P-T phase diagram of hydrogen

Three solid phases were established before 2011 and the structure of phase I with the space group of $P6_3/mmc$ was determined. This structure (phase I) persists to at least 119 GPa at 300 K as revealed by XRD measurements (Loubeyre *et al.*, 1996). Phase I transforms to broken-symmetry phase II at temperatures less than 150 K and 110 GPa. Phase II then transforms to phase III at 150 GPa. Phase III maintains up to 300 GPa at least. XRD measurements (Akahama and Kawamura, 2010) suggested that hydrogen molecules in phase III remained in the vicinity of the hexagonal-close-packed lattice. *Ab initio* calculations (Pickard and Needs, 2007) showed that a $C2/c$ structure could be a candidate for phase III because its vibrational properties agree with the available experimental data. At higher P, other structures such as molecular $Cmca$-12, followed by $Cmca$, and then monatomic $I4_1/amd$ were predicted (Pickard and Needs, 2007). Figure 25 summarizes the phase diagram of hydrogen.

Major advances in understanding the phase diagram of hydrogen came in 2011–2016. A new solid phase of dense hydrogen, phase IV, was experimentally discovered at 300 K and above 230 GPa (Eremets and Troyan, 2011; Howie *et al.*, 2012; Zha, Liu, and Hemley, 2012). This new phase IV exhibits a change in the gradient of the fundamental vibrational-mode frequency and a remarkable drop in resistance with respect to P at a constant temperature 300 K. Based on Raman spectroscopy, Howie *et al.* (2012) proposed a structural model for the newly discovered phase IV. This structure is highly unusual; it consists of unbound molecules lying in a layer sandwiched between honeycomb graphenelike layers made of six-atom rings, which are unsymmetrical and have different size lengths, yielding both molecular and "atomic" (in the rings) hydrogen at the same time. Besides having an unusual structure, phase IV exhibits other exciting properties. The extrapolation shows that the minimum P needed to close the band gap and turn hydrogen into metal is above 375 GPa at 300 K.

It was proposed that at high P the increased energy of the zero-point oscillations in hydrogen would destabilize the lattice and form a ground fluid state at the absolute zero temperature. Theories also suggest (Babaev, Sudbø, and Ashcroft, 2004, 2005) that this fluid state, representing a new state of matter, would have unusual properties governed by quantum effects, such as superfluidity and superconductivity. The maximum of the P-T melting curve was indeed observed. A high P-T Raman spectroscopy study (Howie, Dalladay-Simpson, and Gregoryanz, 2015) explored this possibility by mapping the phase diagram of hydrogen at above 200 GPa and T from 300 to 800 K. A new phase

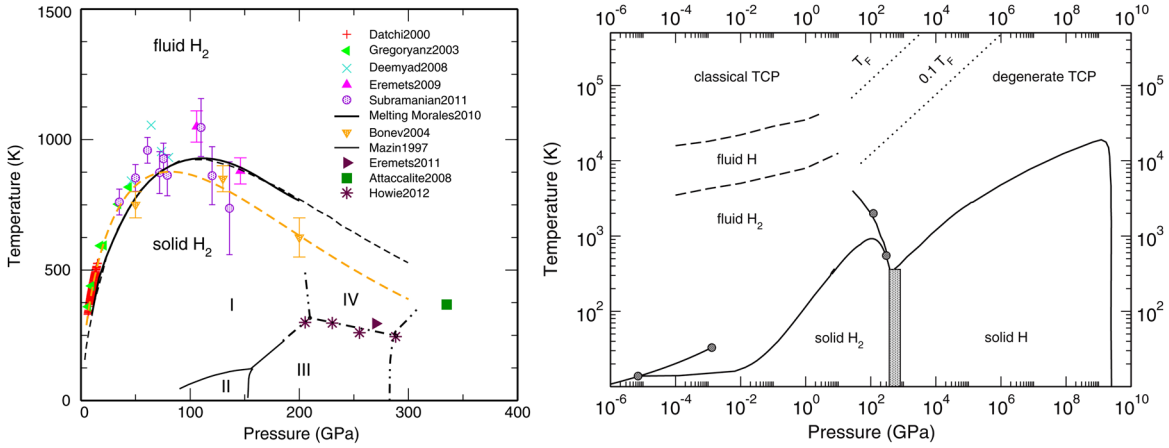

FIG. 25. Hydrogen phase diagram. Left: experimental results; right: theoretical predictions. From McMahon *et al.*, 2012.

transition was observed as T increased above 480 K at 255 GPa (Howie, Dalladay-Simpson, and Gregoryanz, 2015). The transformation was interpreted as melting, which would be the lowest melting temperature of any material at these high P.

Recent experimental breakthroughs have revealed a remarkably rich and interesting phase diagram comprising of at least five distinct molecular solid hydrogen phase regions at 100–385 GPa and 300 K. A Raman spectroscopy study up to 360 GPa by Zha *et al.* (2014) reported a new solid phase of dense hydrogen and deuterium and tentatively identified it as phase V. A Raman spectroscopy study up to 385 GPa by Dalladay-Simpson, Howie, and Gregoryanz (2016) gave Raman evidence of measuring hydrogen and deuterium samples and reported a new solid phase V above 325 GPa with slightly different criteria from Zha *et al.* (2014). Although the ultimate goal of metallic hydrogen appears close, the last mile is harder than ever due to several challenging factors. First, 400 GPa is the practical P limit of a DAC experiment for any sample, let alone hydrogen, which is hard to retain under extreme conditions. Secondly, one must demonstrate the retention of hydrogen to the maximum P. The most common failure is caused by losing hydrogen through diffusion into the gasket or anvil. The collapse of the sample chamber and intrusion of the metallic gasket into the previous hydrogen region will result in an opaque and reflective "sample" which gives the appearance of metallic hydrogen.

Sample characterizations for multimegabar hydrogen studies have been limited to optical spectroscopies. Fundamental investigations on hydrogen crystal structures and electronic band structures that directly relate to metallization are still unattainable. Nevertheless, the ultimate experimental question of metallic hydrogen is about its electronic band-gap closure, but the hydrogen band gap has not been measured directly even at relatively low P. All previous studies on the P-induced changes of the electronic structure of hydrogen are based on indirect measurements of the refractive index and dielectric coefficient (Hemley, Hanfland, and Mao, 1991), infrared reflectivity and absorption (Hemley *et al.*, 1996; Loubeyre, Occelli, and LeToullec, 2002), or transport properties (Eremets and Troyan, 2011). Solid hydrogen has a very wide electronic band gap of 14.5 eV in the vacuum ultraviolet region. Measurement of the hydrogen band gap with 14.5 eV one-photon probing is not possible in the DAC as the photon will be completely blocked by the diamond band gap that forbids all lights above 5 eV. However, the hydrogen sample in a DAC is accessible by IXS; with tens of keV high-energy x-ray photon in and photon out, it analyzes the energy loss between the two photons. Using a beryllium gasket and a panoramic DAC, it is possible to conduct IXS spectroscopy of the second-row elements at high P (Mao *et al.*, 2002, 2006; Lee, Eng, and Mao, 2014), but hydrogen is particularly difficult. The challenges are threefold: First, IXS is a count-limited technique. Second, as the lightest element, hydrogen is by far the weakest x-ray scatterer and all sample-containment materials of the P cell, such as Be and diamond, appear as heavy elements that produce overwhelming background signals. Third, ultrahigh P is achieved by minimizing the sample volume; the hydrogen sample at 360 GPa is only 3–5 μm diameter and 1 μm thick. Nevertheless, the IXS study of hydrogen and its band-gap closure could well be a challenging goal for the next-generation synchrotron x-ray facilities.

C. Helium: The widest-gap insulator under compression

P effects on the band structures of insulators are of great interest and have been widely studied. Helium has the largest known band gap and its change under high P-T conditions attracts great interest from astrophysicists. Helium makes up a large fraction of giant gaseous planets, including Jupiter and Saturn, where it is subjected to extremely high P-T conditions. Using first-principles molecular dynamics simulations, Stixrude and Jeanloz (2008) showed that band closure in pure helium occurs at lower P than previously thought. This suggests that helium behaves as a metal, at least at the highest P encountered in Jupiter and perhaps over a wider range of P in the many hotter and larger planets than Jupiter. From static high-P experiments, H. K. Mao *et al.* (2010) carried out the first direct measurement of the electron excitations of single-crystal helium above 11 GPa using IXS (Fig. 26). A rich electron excitation behavior was revealed including a cutoff edge above 23 eV, a sharp exciton peak showing linear volume dependence, and a series of excitations and continuum at 26 to 45 eV. The electronic dispersion over two Brillouin

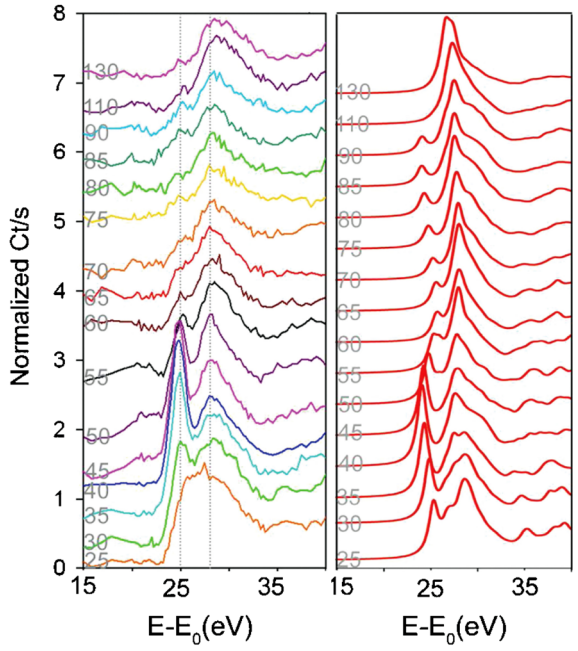

FIG. 26. The first direct measurement of electron excitations of single-crystal helium above 11 GPa. (Left) Experimental and (right) theoretical IXS spectra along the $h00$ direction, IXS spectra are shown with scattering angles from 25° to 90° in 5° steps and 90° to 130° in steps of 20°. From H. K. Mao *et al.*, 2010.

zones was determined, providing important information to understand its band structure under high P.

VI. P EFFECTS ON ELECTRON BONDING STRUCTURES

A. P effects on s- and p-electron bonding

P can drastically alter the nature of s- and p-electron bonding. Under P, the ordinary sense of "reactive" and "inertness" changes. For instance, the inert-gas element helium forms a compound with nitrogen (Vos and Schouten, 1991), argon forms a van der Waals compound with hydrogen which is stable to 358 GPa (Ji *et al.*, 2017), and xenon forms compounds with hydrogen (Somayazulu *et al.*, 2010), fluorine (Kim, Debessai, and Yoo, 2010), and oxygen (Dewaele *et al.*, 2016). Noble metals are no longer noble but react to form nitrides (Gregoryanz *et al.*, 2004; Young *et al.*, 2006). P could cause highly reactive molecules, such as H_2 and O_2, to become inert to each other and coexist in the same crystal (Mao *et al.*, 2006). Even some of the most common materials behave in highly unusual ways under P. Sodium chlorides are found to form exotic stoichiometry, including the cubic and orthorhombic $NaCl_3$ and two-dimensional metallic tetragonal Na_3Cl (W. Zhang *et al.*, 2013).

The high-P x-ray Raman spectroscopy provides a particularly powerful probe for studying the changes of the s-p bonding of second-row elements (Lee, Eng, and Mao, 2014), as shown in studies of carbon (Mao *et al.*, 2003), BN (Mujica *et al.*, 2003; Meng *et al.*, 2004), oxygen (Meng *et al.*, 2008), borates (Lee *et al.*, 2005, 2007), and silicates. The hybridization of atomic orbitals is greatly influenced by their strong interactions at high P. The sp^2 (π^*) bonding, which is the basic structural unit of B, C, and N, becomes unstable and converts to sp^3 (σ^*) bonding at high P. X-ray diffraction and near carbon K-edge x-ray Raman spectroscopy of graphite at high P (Mao *et al.*, 2003) revealed that half of the π^* bonds between graphite layers convert to σ^* bonds above 17 GPa, whereas the other half remain as π^* bonds, resulting in a new carbon allotrope that is superhard and can cause indentation in diamond. This new phase was later calculated to have a monoclinic crystal structure (Li *et al.*, 2009). Another amorphous carbon allotrope with nearly complete π^* to σ^* conversion was found to be a superhard amorphous diamond (Lin *et al.*, 2011; Niu *et al.*, 2012). Some specific examples follow.

B. Compressional behavior of free-electron gas

Alkali metals, with a single conduction s electron per atom, are considered the best examples of nearly free-electron (NFE) gas which was the original conjecture of the atomic metallic hydrogen. However, new theories surprisingly predict that the archetypal alkali metals Li and Na lose their NFE characters. Neaton and Ashcroft (1999) made a bold conjecture predicting that atoms in these archetypal metals may pair and become insulators under high P (Ashcroft, 2002) and become the counter example of metallization and dissociation of H_2. P-induced high superconducting temperatures in Li have reached up to 20 K (Shimizu *et al.*, 2002; Struzhkin *et al.*, 2002; Deemyad and Schilling, 2003). A study of Na above 100 GPa led to the discovery of its room temperature melting point at 118 GPa (Gregoryanz *et al.*, 2005). A study of elemental Li (Guillaume *et al.*, 2011) revealed seven complex structures and a record low high-P melting minimum at 200 K and 40 GPa. The complex structures and phase diagram were immediately corroborated by independent first-principles calculations. Finally, a metal-semiconductor transition was reported with optical and electric measurements at 90 GPa (Matsuoka and Shimizu, 2009). Likewise, Na was observed becoming insulating in the $hP4$ structure above 200 GPa (Ma *et al.*, 2009). The surprising crystallographic complexities of Na and Li at high P are closely connected to their electronic properties. Results from megabar DACs and optical probes have observed evidence of a band-gap opening (Lazicki *et al.*, 2009).

Synchrotron high-P IXS (Mao *et al.*, 2011) has been used to observe the Na and Li plasmon peaks which are collective (a discrete number) oscillations of the free-electron gas density. The high-P IXS studies have directly monitored the change of NFE gas behavior of Na up to 90 GPa. The dynamic structure factor of lithium in the intermediate-q regime was determined at ambient P (Hill *et al.*, 1996). IXS from the K edge of lithium metal at forward and backscattering geometries was further conducted to reveal dipolar ($1s \rightarrow p$) to monopolar ($1s \rightarrow s$) excitations (Krisch *et al.*, 1997). However, all literature on the IXS of Li is limited to ambient P, and high-P electronic information is still completely missing.

C. P-induced Fermi surface nesting

When different parts of the Fermi surface coincide by shifting a certain wave vector, a nested Fermi surface forms.

Mathematically, the energy spectrum satisfies the condition $E(\boldsymbol{k}+\boldsymbol{Q}) = -E(\boldsymbol{k})$, where $\boldsymbol{Q}$ is the nesting vector, and the energy is counted relative to the chemical potential. A nested Fermi surface can result in a logarithmic divergence in the susceptibility or response function (Khomskii, 2010). This divergence leads to instabilities of metals with respect to the formation of a charge density wave (CDW) or spin density wave (SDW), with an ordering wave vector usually equal to the nesting vector Q. Such a logarithmic divergence can be responsible for the Kohn anomaly in the renormalized phonon energy spectra too.

The Fermi surface nesting vector could be reduced by compression to induce a structure distortion. For example, while the elemental vanadium is stable in that bcc structure at ambient P, XRD studies (Ding *et al.*, 2007) discovered that vanadium undergoes a second-order phase transition through continuous distortion into a rhombohedral lattice at 63–69 GPa. According to calculations (Landa *et al.*, 2006), a Kohn anomaly appears at ambient P at $\boldsymbol{q} = 1/4$ along the $[q00]$ direction in the transverse acoustic phonon mode, a consequence of Fermi surface nesting in the third band. Upon compression, the nesting vector $\boldsymbol{q}_n = 0.48\pi/a$ decreases and the effect of the Kohn anomaly on C_{44} increases; when q_n becomes zero a minimum appears in the shear elastic constant C_{44} due to an electronic topological transition. Such a softening of C_{44} is responsible for the P-induced cubic-rhombohedral distortion in vanadium (Fig. 27). Theoretical predictions on elemental vanadium, tantalum, and niobium are quite similar, and the theoretically proposed shear softening in Ta has been experimentally observed (Antonangeli *et al.*, 2010).

Ca-III, the first superconducting calcium phase under P, was identified as sc by x-ray diffraction experiments. In contrast, all previous theoretical calculations showed that sc has a higher enthalpy than many proposed structures and possesses an imaginary phonon branch. By using newly developed sub-μm high-P single-crystal XRD, cryogenic high-P XRD, and theoretical calculations, W. L. Mao *et al.* (2010) demonstrated that Ca-III is neither exactly simple cubic nor any of the lower-enthalpy phases, but sustains the simple-cubic-like, primitive unit by a rhombohedral distortion at 300 K and a monoclinic distortion below 30 K. The origin of these distortions is the P-induced Fermi surface nesting that causes phonon instability. In response to phonon instability, the primitive cell simply distorts slightly into a nearby phonon-stable form (W. L. Mao *et al.*, 2010).

P could also suppress the CDW to induce a quantum critical point. For example, the elemental chromium orders antiferromagnetically near room temperature and the ordering temperature can be driven to zero by applying high P. Feng *et al.* (2007) combined DAC and synchrotron x-ray diffraction techniques to directly measure the spin and charge orders in the pure metal as it approached a quantum critical point (Fig. 28). Both spin and charge orders are suppressed exponentially with P. By comparing the development of the order parameter with that of the magnetic wave vector, they attributed the destruction of antiferromagnetism to the growth in electron kinetic energy, relative to the underlying magnetic exchange interaction.

VII. HIGH-P STUDIES ON d-ELECTRON SYSTEMS

Materials that contain transition-metal elements from the third to the fifth rows in the periodic table are d-electron

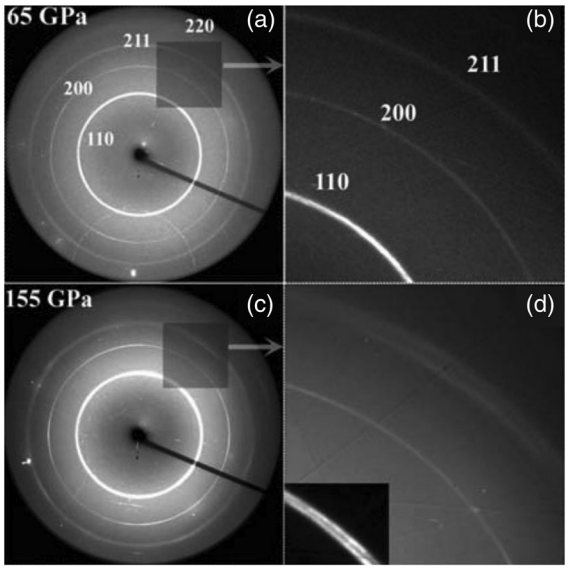

FIG. 27. (a) The XRD pattern of bcc vanadium recorded on an image plate at 65 GPa. (c) The XRD pattern of vanadium at 155 GPa. (b), (d) The enlarged images of the shadow areas in (a) and (c), respectively. Splitting of 110 shows a rhombohedral distortion above 69 GPa, which is associated with Fermi surface nesting. From Ding *et al.*, 2007.

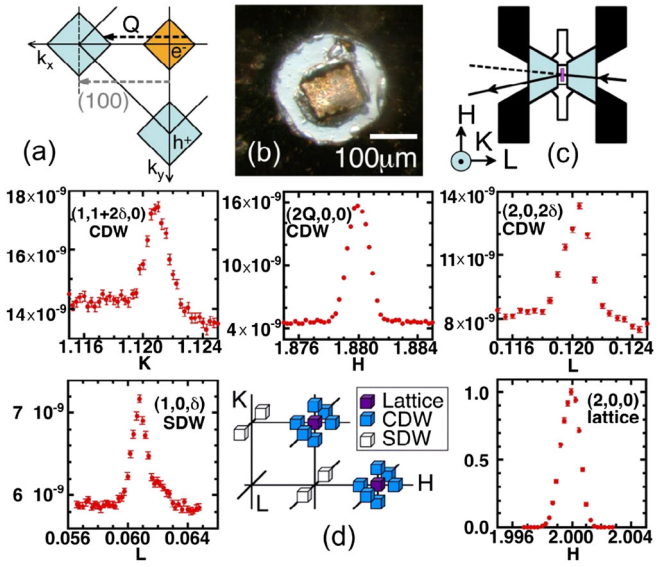

FIG. 28. XRD measurement of an incommensurate SDW and CDW in a DAC. (a) Schematic diagram of Cr's Brillouin zone. (b) Typical view through the P chamber shows a single-crystal Cr sample. (c) Schematic diagram of XRD through DAC. (d) High-resolution and high-sensitivity monochromatic x-ray diffraction from Cr at 8 K and 4.0 GPa. The results show that P suppresses both spin and charge orders to approach a quantum critical point. From Feng *et al.*, 2007.

systems. They are the most studied compounds in condensed-matter physics due to their interesting physical phenomena, including the Mott insulating state, high-T_c superconductivity, magnetism, multiferroicity, colossal magnetic resistance, etc.

One characteristic of d-electron systems is that they have unfilled d shells, and the special extension of the d-electron wave function is usually smaller than the distance between the atoms or ions, especially in oxides. These compounds thereby correspond to a low-density electron system with $r_s \gg 1$, where $r_s = r_{s(\mathrm{ave})}/a_0$, $r_{s(\mathrm{ave})}$ is the average electron distance, and a_0 is the Bohr radius, in contrast to the typical metals with $r_s \sim 2$–3. In these systems, the effective hopping of electrons between metal ions t, which determines the electron bandwidth $W \sim 2zt$ (z is the lattice coordination number), is much smaller than the on-site Coulomb electron-electron interaction U (Hubbard term). It is due to such a large electron interaction or correlation effect that Fermi-liquid theory, where electrons are treated as weakly interacting, can break down, causing the field of strong electron correlations.

The competition between electron itinerancy in solids, originating from wave function hybridization and localization effect due to electron-electron repulsion, forms the central theme of strongly correlated systems (Harrison, 1989; Basov *et al.*, 2011; Khomskii, 2014). In addition, the d electrons have their own internal degrees of freedom such as charge (e), spin (s), and orbital (l). Since the d electrons also couple with the lattice, the interplay between the d-electrons' internal degrees of freedom with the lattice (or phonon) forms a delicate balance for the whole quantum system. Such a balance, however, is highly susceptible to external influences such as the T, P, magnetic field, or doping, which could lead to many emergent phenomena with novel properties. In this regard, the field of electron-correlated systems concerns not only strong electron interaction, but also the interplay between various intertwined degrees of freedom.

P is a unique parameter in terms of tuning a system's electronic and magnetic structures for various reasons: (1) P is powerful; it changes the energy by $V\Delta P$. For instance, the effect of 1 T (on $g = 2$ materials) is ~1 K, while 1 GPa is ~614 K for Fe to be compressed to 100 GPa (Rueff and Shukla, 2010). Currently static compression by DAC in the laboratory can easily reach 200–300 GPa. (2) P is clean. Its main effect is to change the lattice parameters, which makes experiments more theoretically transparent compared with chemical doping. (3) P is effective. It directly changes the bond length and bond angle, which are the key parameters determining the effective hopping t, which in turn govern the system's electronic and magnetic structures. In contrast, T and the magnetic field more directly couple with phonons and electron spins, respectively.

P can not only tune the competition between the electron interaction U and bandwidth W, but also breaks the delicate balance formed by the interplay of the spin, orbital, charge, and lattice degrees of freedom. Many novel transitions, such as the spin-pairing transition, Mott insulator-metal transition (IMT), magnetic transitions, quantum critical point, and quantum phase transitions, have been observed in transition-metal compounds at high P.

A. Spin-pairing transitions

When transition-metal ions form a crystal, the interaction of the d electrons with the surrounding ions in the crystal splits the fivefold degenerate d levels. The splitting of the d levels is determined by the local symmetry of the crystal field. In this section, we discuss only the octahedral crystal field with local ligand O_h or nearly O_h symmetry. For instance, if a transition-metal ion is surrounded by an octahedron of anions (a typical situation in transition-metal compounds such as NiO or CoO), the fivefold d level splits into a lower-energy triplet t_{2g} group and a higher-energy doublet e_g group. The energy difference between the two groups is the crystal field splitting Δ_{cf}, also called $10Dq$.

In principle, there are two contributions to the crystal field splitting of the d levels: one is the point charge contribution (Coulomb repulsion from negatively charged ligands), and the other is the d-p orbital covalency or hybridization (Khomskii, 2014). Both contributions could be tuned by P, and the value of Δ_{cf} increases with external P. As the electron filling in the split d levels depends on the competition between the crystal field splitting Δ_{cf} and Hund's exchange coupling J_H, the so-called "spin-pairing transition" [also named the high-spin (HS) to low-spin (LS) transition, the spin-state transition, or the spin-crossover transition] could be induced by external P when Δ_{cf} reaches a critical value.

For example, in compounds with a $3d^4$ or $3d^5$ configuration (e.g., Mn^{3+}, Mn^{2+}, or Fe^{3+}) in an octahedral crystal field, after three electrons occupy the t_{2g} group with parallel spins, the fourth electron could occupy either the e_g group to form a HS state or the t_{2g} group to form a LS state. In a simple atomic picture, the energy difference between the HS and LS states is $\Delta E = E^{\mathrm{HS}} - E^{\mathrm{LS}} = \Delta_{\mathrm{cf}} - 3J_H$ (Khomskii, 2014). For $3d$ transition-metal oxides, Δ_{cf} is typically about 2 eV, whereas J_H is about 0.8–0.9 eV. Therefore, $\Delta E < 0$ and the HS is favored for $3d$ transition-metal oxides at ambient conditions. In contrast, in $5d$ transition-metal oxides, as the wave function of $5d$ is more extended than that of $3d$, Δ_{cf} becomes larger (~3.0 eV) and J_H is smaller (~0.5–0.6 eV). Consequently, $\Delta E > 0$ and the LS is usually favored by $5d$ oxides, such as iridates.

Δ_{cf} is proportional to $K/d_{\mathrm{T\text{-}O}}^n$ ($n = 3.5$–7) (Harrison, 1989) where K is a constant and $d_{\mathrm{T\text{-}O}}$ is the bond length between the transition-metal ion and the ligand anion. At certain critical P, a spin-pairing transition occurs with $\Delta_{\mathrm{cf}} - 3J_H$ changes from negative to positive. For example, at ambient conditions α-Fe_2O_3 (hematite) is an AF insulator in a corundum structure. Rozenberg *et al.* (2002) discovered that it transforms to the Rh_2O_3 (II)-type structure, with a 10% reduction in volume at 50 GPa. Pasternak *et al.* (1999) implied a collapse of the magnetic moments and a nonmagnetic nature of the high pressure phase based on their Mössbauer spectroscopy measurements. Conductivity measurements indicate that an insulator-to-metal transition occurs between 40 and 60 GPa. Using XES, Badro *et al.* (2002) showed that the magnetic moment dropped from HS to LS at 72 GPa. Wang, Ding *et al.* (2010) observed with high-P partial fluorescence yield Fe K-edge x-ray absorption spectroscopy measurements that Fe_2O_3 transforms from a HS insulator to a

LS metal above 48 GPa. These studies indicate that α-Fe_2O_3 undergoes multiple transitions including a spin-pairing transition, structure transition, and insulator-metal transition at around 50 GPa.

MnO is a textbook example of a Mott insulator. Yoo *et al.* (2005) revealed an isostructural, first-order Mott transition in MnO at 105 GPa, with a 6.6% volume collapse and insulator-metal transition, based on high-resolution XES spectroscopy and angle-resolved XRD data. Mattila *et al.* (2007) confirmed that the nature of the transition at ~100 GPa is a spin-pairing transition, by combining XES and ligand multiplet calculations.

Lyubutin *et al.* (2009) investigated a series of compounds containing Fe^{3+}, such as $FeBO_3$, $LuFeO_3$, $YFeO_3$, $BiFeO_3$, $GdFe_3(BO_3)_4$, $NdFeO_3$, and $LaFeO_3$ by applying nuclear resonant forward scattering, XES, and optical absorption techniques. All these materials were found to display *P*-induced spin-pairing transitions at around 40–60 GPa. Intriguingly, the spin-pairing transitions in these materials were also accompanied by insulator-to-metal transitions.

For the $3d^6$ and $3d^7$ configurations (e.g., Fe^{2+}, Co^{3+}, Co^{2+}, and Ni^{3+}), however, the LS state is more likely to become the ground state upon compression. These examples include FeS (Rueff *et al.*, 1999), FeO (Mattila *et al.*, 2007), and (Mg,Fe)O (Badro *et al.*, 2003). Moreover, as the energy difference ΔE becomes smaller for the $3d^6$ case, an intermediate-spin (IS) state can also appear, e.g., $LaCoO_3$ (Vankó *et al.*, 2006) and Fe_3O_4 (Ding *et al.*, 2008). FeS is an AF insulator ($T_N \sim 598$ K) in a NiAs-type structure. FeS is at the boundary between the charge-transfer and Mott-Hubbard insulators in the Zaanen, Sawatzky, and Allen (ZSA) classification scheme. Using XES spectroscopy, Rueff *et al.* (1999) reported a *P*-induced HS to LS transition in FeS around 7 GPa. The transition is evidenced by the disappearance of the low-energy satellite in the Fe $K\beta$ emission spectrum. This pioneering experiment established the use of XES as a diagnostic tool for characterizing the local spin-moment and spin-pairing transition under *P*. The spin-pairing transition in FeS was also confirmed by Nyrow *et al.* (2014) with XRS measurements on the M_{23} edge of Fe.

In CoO and FeO, a magnetic collapse attributed to the spin-pairing transition was reported at 90–100 GPa by Mattila *et al.* (2007) using XES assisted by the ligand multiplet calculations (Fig. 29). The ionic radii (i.e., the sizes) of the HS and LS states of the same ion are substantially different. The LS ions are always smaller than their HS counterparts, and this difference can be as much as 15%. For example, the ionic radius of the 6-coordinated HS Co^{3+} is 0.61 Å, and that of its LS counterpart is 0.545 Å. Therefore, *P* would tend to stabilize the LS state and favor the HS-LS transition, which leads to significant volume reduction. Its occurrences in major mantle minerals, such as ferropericlase, bridgmanite, and postperovskite, are important for understanding the seismic wave heterogeneity in the lowermost mantle and would affect the interpretations of the geophysical and geochemical models (Lin *et al.*, 2005; Badro, 2014).

Using XES, Vankó *et al.* (2006) confirmed the IS-to-LS transition in $LaCoO_3$ that was reported by Vogt *et al.* (2003). Moreover, their PFY XANES spectra also show a continuous redistribution of the $3d$ electrons between the t_{2g} and e_g levels of cobalt caused by the spin-pairing transition. Ding *et al.* (2008) observed a reduction of the magnetic moment in Fe_3O_4 between 12 and 16 GPa. Based on the XES and theoretical modeling, they also attributed the moment reduction to an HS-to-IS transition of Fe^{2+} in the octahedral sites.

B. Mott insulator-to-metal transition

Insulators can be classified into several types: (a) a band-gap insulator, (b) a Peierls insulator, (c) an Anderson insulator, and (d) a Mott insulator. The formations of (a)- and (b)-type insulators are primarily due to electron interactions with the crystal lattice and phonons. In principle, the transitions from these insulators to metals could be understood in the

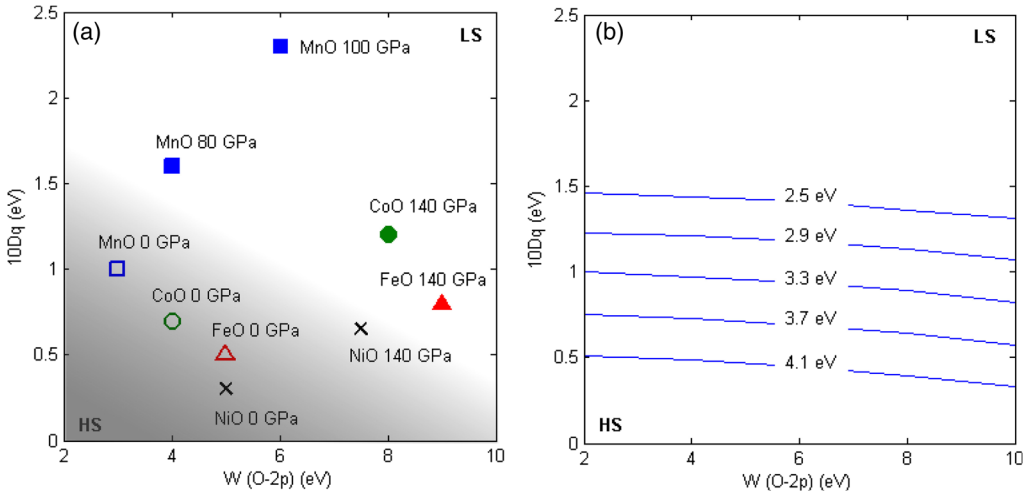

FIG. 29. Phase diagram of the magnetic collapsed in the transition-metal oxides. (a) The symbol coordinates refer to the calculated values of $10Dq$ and W (O-$2p$), for the HS (open symbols) and LS (closed symbols) states. Crosses indicate the absence of a spin transition. The shaded area is a guide to the eye separating the two regions. (b) The lines mark the calculated HS-LS transition boundary for the d^7 configuration for different values of V_{eg} (hybridization strength). From Mattila *et al.*, 2007.

framework of standard band theory without invoking an electron-electron interaction. However, the formation of a Mott insulator goes beyond band theory and is purely due to the electron interaction or correlation effect. For instance, band theory predicts a metallic ground state of NiO and CoO, in conflict with experimental findings. The term "Mott insulator" was later coined for the class of solids violating the simple expectation of band theory. The Anderson insulator involves an interaction between localized and itinerant electrons, but will not be discussed in this section.

Although Mott transitions occur in Mott insulators, not all Mott insulator-to-metal transitions are pure Mott transitions. In a pure sense, the term Mott transition is a localized-itinerant transition without any accompanying long-range order, which in principle could be driven by band-filling control or bandwidth control (Imada, Fujimori, and Tokura, 1998). Band-filling-controlled transitions cause the system to become metallic under doping or a change of electron concentration. Bandwidth-controlled transitions are driven by a change in the ratio between the Coulomb interaction (or the on-site Hubbard repulsion) U to the bandwidth $W \sim 2zt$. For U/W bigger than a critical (U/W), the material is a Mott insulator, while for smaller U/W it is a metal. Such transitions can be ideally induced by the application of P, which increases the overlap of wave functions and consequently the electron hopping t as well as the bandwidth W. Moreover, the on-site Coulomb interaction can be screened more efficiently when the material approaches the itinerant regime. This can accelerate the insulator-metal transition under P because of a faster decrease of U/W. However, in reality, a pure Mott transition is rarely observed because structural transition, spin-pairing transition, or charge ordering would usually also concur or occur earlier.

So far, most Mott insulator-to-metal transitions reported usually concur with a spin-pairing transition or structure transitions or distortion. The spin-pairing transition could modify U, which may, in turn, trigger the insulator-metal transition. On the other hand, an accompanied structural transition would make it more difficult to determine the mechanism underlying the insulator-metal transition. In this sense, these types of Mott insulator-to-metal transitions simply might not be regarded as pure Mott transitions, as their metallization could be related to the change of the spin state or lattice. In fact, the spin-pairing transition induced metallization of Mott insulators is now specifically called a "Hubbard energy control" (Lyubutin *et al.*, 2009) insulator-to-metal transition, a new type of control in addition to the band-filling control and bandwidth control. The mechanism can be understood as follows.

As U is defined by $U_{\mathrm{eff}} = E(d^{n+1}) + E(d^{n-1}) - 2E(d^n)$, how much U changes when the spin-pairing transition occurs is estimated by applying a simple atomic model. For compounds containing Fe^{3+} or Mn^{2+} (d^5), when an HS to LS crossover transition occurs, the change of U_{eff} is equal to $U^{\mathrm{LS}}_{\mathrm{eff}}(d^5) - U^{\mathrm{HS}}_{\mathrm{eff}}(d^5) = (U - J_H) - (U - \Delta_{\mathrm{cf}} + 4J_H) = \Delta_{\mathrm{cf}} - 5J_H$ (Khomskii, 2014). Since Δ_{cf} is about 2 eV and J_H is about 0.8–0.9 eV, it is clear that an HS to LS spin-pairing transition can cause a reduced U_{eff}, which thereby also favors an insulator-metal transition. This mechanism might be related to the metallization of Fe_2O_3 (Pasternak *et al.*, 1999; Badro *et al.*, 2002; Wang, Ding *et al.*, 2010), MnO (Yoo *et al.*, 2005; Mattila *et al.*, 2007), $FeBO_3$ (Lyubutin *et al.*, 2009), $GdFe_3(BO_3)_4$ (Lyubutin *et al.*, 2009), $RFeO_3$ (R = La, Nd, Pr, Lu) (Lyubutin *et al.*, 2009), and $BiFeO_3$ (Lyubutin *et al.*, 2009).

Since AF ordering is more common than FM ordering in transition-metal oxides, here we discuss only the AF state. For compounds containing $Fe^{2+}(3d^6)$, $Co^{3+}(3d^6)$, or Co^{2+} $(3d^7)$, the change of U during a spin-crossover transition is $U^{\mathrm{LS}}_{\mathrm{eff}}(d^6) - U^{\mathrm{HS}}_{\mathrm{eff}}(d^6)(\mathrm{AF}) = (U + \Delta_{\mathrm{cf}} - J_H) - (U - \Delta_{\mathrm{cf}} + 3J_H) = 2(\Delta_{\mathrm{cf}} - 2J_H)$ or $U^{\mathrm{LS}}_{\mathrm{eff}}(d^7) - U^{\mathrm{HS}}_{\mathrm{eff}}(d^7)(\mathrm{AF}) = \Delta_{\mathrm{cf}} - 2J_H$. When the spin-pairing transition occurs for d^6 and d^7 configurations, Δ_{cf} should be equal to or larger than $2J_H$. In this situation, U is actually larger in the LS state. Consequently, for FeS, FeO, and CoO, their metallization cannot simply be attributed to the spin-pairing transition. Therefore, while MnO (d^5), FeO (d^6), and CoO (d^6) all have a distorted fcc structure with spin-pairing transitions above 80–140 GPa, these materials have quite different metallization scenarios and possibly different mechanisms: MnO becomes metallic simultaneously with the spin-pairing transition due to the Hubbard energy control, while FeO has to be heated above 1000 K to become metallic after a spin-pairing transition (Fischer *et al.*, 2011; Ohta *et al.*, 2012). CoO becomes metallic between 43 and 63 GPa, but coincides with a structural transition (cubic to rhombohedral distortion) at 42 GPa (Guo *et al.*, 2002), so it is still difficult to determine if the metallization of CoO is driven by electron correlation U/W or by the structural transition.

In contrast to the aforementioned examples, NiO with a $Ni^{2+}(d^8)$ configuration has no LS state. Gavriliuk, Trojan, and Struzhkin (2012) observed that the resistance of NiO drops by ~3 orders of magnitude at ~240 GPa with a concomitant change of the resistance behavior from semiconducting to metallic. Based on simple multielectron considerations, they concluded that the metallic phase of NiO forms when the effective Hubbard energy U_{eff} is almost equal to the estimated bandwidth $2W$, where U_{eff} is defined as the U/W, U is the on-site electron-electron Coulomb repulsive interaction, and W is the bandwidth. If there is no structural distortion or a structural transition concurs with such an insulator-metal transition, this case could be regarded as a perfect pure Mott transition (Fig. 30).

While some other Mott insulator-metal transitions without spin-pairing transitions have been reported at high P, most of them were accompanied by structural transitions or distortion. In this situation, where the d-electron charge, spin, and orbital degrees of freedom are strongly coupled with the lattice, it remains a challenge to clearly determine the driving force of a Mott insulator-to-metal transition.

For example, $LaMnO_3$ is the parent compound for many doped manganites that exhibit colossal magnetoresistance. This system displays a complex correlation between the structural, orbital, magnetic, and electronic degrees of freedom. Extrapolating Raman and XRD data, the complete suppression of the JT distortion was predicted at 18 GPa, supporting the view of $LaMnO_3$ as a classical Mott insulator. Using high-P and low-T Raman spectroscopy, Baldini *et al.* (2011) provided the first experimental evidence of the

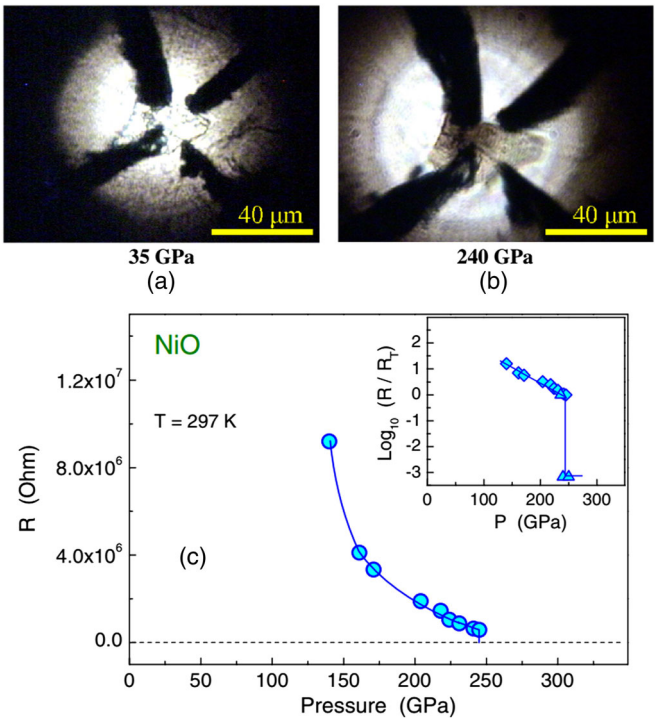

FIG. 30. Resistivity measurements of NiO at high P, where NiO becomes metallic at ~240 GPa. The images of a NiO sample at (a) 35 GPa and (b) 240 GPa. The four Pt leads are connected to the NiO sample in the central part of the cBN gasket. (c) A strong nonlinear decrease of resistance in the NiO sample has been measured at room temperature under compression. From Gavriliuk, Trojan, and Struzhkin, 2012.

persistence of the JT distortion in $LaMnO_3$ up to 34 GPa over the entire stability range of the insulating phase and thus revived the debate on the character of the insulating phase and the origin of the IMT in $LaMnO_3$.

V_2O_3 is a textbook Mott system and has been studied for more than 60 years. Its IMTs are usually accompanied by structural changes, and the mechanisms of the IMT have been under heated debate, in spite of the tremendous efforts devoted to this topic. Recently Ding *et al.* (2014) observed that P can decouple the hexagonal-monoclinic structure transition from the IMT in V_2O_3. Based on their x-ray Raman scattering experiments and multiplet calculations, they concluded that the Mott IMT in V_2O_3 could not occur if the electron correlation strength does not reach a critical value (Ding *et al.*, 2014).

Another example is $GaTa_4Se_8$. Abd-Elmeguid *et al.* (2004) showed that $GaNb_4Se_8$ and $GaTa_4Se_8$ transform at 13 and 11.5 GPa from Mott insulators to a metal with a superconducting $T_c = 2.9$ and 5.8 K, respectively. The superconductivity was shown to be correlated to a P-induced decrease of the MSe_6 (M = Nb, Ta) octahedral distortion and simultaneous softening of the phonons associated with the M-Se bonds (Ohta *et al.*, 2012). However, Phuoc *et al.* (2013) observed a charge gap of ~0.12 eV and a broad midinfrared band at ~0.55 eV in a $GaTa_4Se_8$ single crystal. As the P increases, the low-energy spectral is strongly enhanced and the optical gap is rapidly filled, indicating an IMT at around 6 GPa. The evolution of the optical conductivity was considered as evidence that $GaTa_4Se_8$ is a Mott insulator which undergoes a bandwidth-controlled Mott IMT under P.

A Mott IMT could also concur with a CDW, charge disproportionation, or SDW. For the type of Mott IMT related to charge and spin ordering, it is generally believed that both the electron-electron correlation and electron-lattice (or phonon) coupling play important roles. For example, P could suppress charge disproportionation and induce a Mott IMT in $CsAuCl_3$ (Rueff *et al.*, 2006) and $PbCrO_3$. Kojima and Matsushita (2000) reported that in $CsAuCl_3$, P induced an Au valence transition from the $Au^{1+,3+}$ state to Au^{2+}, which is coupled with a structural phase transition. The metallic cubic phase that appeared under high P-T can also be obtained as a metastable phase even at ambient P and room T. This is attributed to the Au valence fluctuation or charge disproportionation. To disclose the origin of the IMT occurring at 1.6 GPa in $PbCrO_3$, J. Cheng *et al.* (2015) applied multiple techniques including electric resistance, x-ray absorption, x-ray and neutron diffraction, as well as density functional theory plus correlation energy U (DFT + U) calculations. They proposed that a charge disproportionation $3Cr^{4+} \rightarrow 2Cr^{3+} + Cr^{6+}$ association with the $6s$-p hybridization on Pb^{2+} is responsible for the insulating ground state of $PbCrO_3$ at ambient P, and that the charge disproportionation phase is suppressed under P to give rise to a metallic phase at high P.

In addition to the aforementioned examples with varying complexities, there still exist many open questions. What are the symmetry breaking order parameters during the Mott transitions? Are the Mott transitions first or second order in terms of the Landau theory of phase transition? Therefore, the Mott transitions will remain a fundamental but challenging topic in high-P physics.

C. Magnetic ordering transition

Mott insulators have localized electrons and magnetic moments. Therefore, most Mott insulators are magnetically ordered due to the exchange interaction between their local magnetic moments. In real materials, there are several factors determining the character, sign, and strength of the exchange interaction, which lead to a great variety of magnetic structures. These factors mainly concern the geometry of the lattice and the type of orbital occupation of different TM ions. In Mott systems, there are three major types of exchange interactions: superexchange, double exchange, and an Ruderman-Kittel-Kasuya-Yosida (RKKY) interaction. These exchange interactions can be tuned by P, changing the lattice parameters orbital occupation, and effective d-d hopping terms.

1. Superexchange

Superexchange originates from the second-order virtual hopping process between two ion sites. In a simple Hubbard model, the electron hopping between two ion sites with parallel spins is forbidden by the Pauli exclusive principle, while hopping between antiparallel spins is allowed. If an electron hops to one site and then hops back to the original

site, this process reduces the electron's kinetic energy by $-t^2/U$ ($U \gg t$). More details are found in the Goodenough-Kanamori-Anderson (GKA) rules. In general, the GKA rules determine the type of exchanges or magnetic ordering for different local coordination and orbital occupation. For instance, when two half-filled orbitals (with one electron) are directed toward each other, the superexchange interaction dominates to form AF ordering. When a half-filled orbital is directed toward an empty or fully occupied (two electron) orbital, the exchanger interaction is weakly ferromagnetic.

As the hopping t is sensitive to P, it could modify the superexchange and then affect the magnetic ordering. In the strong coupling limit of the Hubbard model on a square or cubic lattice, the ground state is AF ordered, which is also observed in many transition-metal compounds.

For instance, the NaCl-structured CoO is a charge-transfer-type Mott insulator with an AF ordering temperature of $T_N = 290$ K. The structure consists of corner-shared CoO_6 octahedra with a 180° Co-O-Co bond angle. In CoO, the dominant exchange interaction is the superexchange with a strength of $J \sim -t_{dd}^2/U \sim t_{pd}^4/\Delta_{CT}^2(\Delta_{CT} + 1/2U_{pp})$, where t_{pd} is the electron hopping term between Co and O, and Δ_{CT} is the charge-transfer gap; in CoO, Δ_{CT} is smaller than U_{dd}. By applying an external P of 2 GPa, the T_N of CoO increases to 300 K due to a P-enhanced J through a stronger t_{pd} hopping and saturates at 12 GPa. The effective increase of t_{dd} between two Co^{2+} sites during the transition from paramagnetic ordering to AF ordering was indeed observed by RXES experiments (Ding *et al.*, 2012).

2. Double exchange

The double exchange can be understood by treating spins quasiclassically with $t \ll J_H$. Because of the strong Hund's rule exchange, the spins of conduction electrons tend to be parallel to the localized spins. Here the electron hopping between two antiparallel spin sites is not energetically favored due to the Hund's exchange interaction at each intrasite. When mobile carriers move in a narrow band due to electron doping, the coupling of localized spins via conduction electrons could become ferromagnetic. This mechanism is called a double exchange. In Mott insulators, localized electrons typically have an AF exchange among them, and it is less favorable for the doped electron to hop between neighboring ion sites whose spins are pointing in the opposite direction. To decrease its kinetic energy, the conduction electron should make all localized spins parallel, i.e., it will result in FM ordering. In this process, by losing the exchange energy of the localized spins J, the doped carriers can gain a kinetic energy of $\sim t_x$, where t is their hopping and x their concentration. Thus, crudely speaking, if $x \geq J/t$, the system would tend to become FM (Khomskii, 2014).

The effects of P on double-exchange systems are complicated, as P could change all parameters in $x \geq J/t$. For instance, $La_{0.75}Ca_{0.25}MnO_3$ is a ferromagnetically ordered perovskite. The FM ordering is due to the double-exchange interaction, which can be regarded as an exchange between the $Mn^{3+}(3d^3)$ and $Mn^{2+}(3d^4)$ ions. When this material is subject to compression, the overall magnetic moment detected by XMCD decreases gradually with P and disappears around 23 GPa (Ding *et al.*, 2009). The underlying mechanism is attributed to a P-induced tetragonal distortion of the MnO_6 octahedra, which reduces the e_g electron occupation along the c axis. This is equivalent to reducing the doped carrier concentration $x < J/t$, which leads to a transition from FM to AF ordering. Moreover, $J = -t^2/U$ could also increase with P, which further accelerates such magnetic transitions.

3. RKKY exchange interaction

When both localized and itinerant electrons exist in a system, yet another mechanism of exchange interaction mediated by conduction electrons appears. If the bandwidth of the conduction band and the corresponding Fermi energy are large, this mechanism is known as the RKKY exchange. The exchange can be expressed as $J(r) \sim \cos(K_F r)/r^3$, where r is the distance between the magnetic ions, and K_F is the Fermi momentum (Khomskii, 2014). This exchange interaction is an oscillatory function of $K_F r$ and thus can be either FM or AF. As P could effectively reduce r, it could induce a transition between different magnetic orderings in an RKKY system.

For instance, in the FM semiconductors $Ga_{1-x}Mn_xAs$, Mn^{2+} ions in the alloys provide local magnetic moments, and at the same time act as a source of valence-band holes that mediate the Mn^{2+}-Mn^{2+} interactions. The coupling is an RKKY exchange that results in a FM phase. Applying hydrostatic P can increase the magnetization and induce a FM phase in an initially paramagnetic alloy (Csontos *et al.*, 2005).

D. Spin-liquid transition

In the frustrated magnets there can be no long-range magnetic ordering, but well-developed short-range AF correlations may still exist. Such states are called spin liquids. There are different types of spin-liquid states, with or without gaps in singlet or triplet excitations. The spin-liquid state could possibly be induced by P.

Cheong and Hwang (2000) reported that two new gapless quantum spin-liquid candidates with $S = 1$ (Ni^{2+}) moments were obtained under high P: the 6H-B phase of $Ba_3NiSb_2O_9$ with a Ni^{2+}-triangular lattice and the 3C phase with a $Ni_{2/3}Sb_{1/3}$ three-dimensional edge-shared tetrahedral lattice. Both compounds showed no magnetic order down to 0.35 K, despite Curie-Weiss temperatures Θ_{CW} of 75.5 (6H-B) and 182.5 K (3C), respectively. Below ~25 K, the magnetic susceptibility of the 6H-B phase saturated to a constant value $\chi_0 = 0.013$ emu/mol, which was followed by a linear T-dependent magnetic specific heat (C_M) displaying a giant coefficient $\gamma = 168$ mJ/mol K^2 below 7 K. Both observations suggest the development of a Fermi-liquid-like ground state. For the 3C phase, the $C_M \propto T^2$ behavior indicates a unique $S = 1$, 3D quantum spin-liquid ground state.

Recently, Zhao *et al.* (2015) measured the specific heat, susceptibility, and dielectric constant for $Y_{1-x}La_xTiO_3$ at high P. They observed a T^2-dependent specific heat at low temperatures for $0.17 < x < 0.3$ samples, indicating a spin-orbital liquid state between the FM or orbital ordering ($x < 0.17$) and AF or possible orbital liquid phase

($x > 0.3$). The nonmonotonous P dependence of T_c and the glassy behavior of the dielectric loss for the $x = 0.23$ sample suggests that it approached a possible quantum critical point.

E. Phase separation and colossal magnetoresistance in manganites

Colossal magnetoresistance (CMR) has been observed in many doped $R_{1-x}A_xMnO_3$ manganites with perovskite structure, where R is a rare-earth element, such as La or Pr, and A is usually Ca or Sr; this leads to an entire class of compounds—CMR manganites that generally have complex and rich phase diagrams. In the archetypal phase diagram of $La_{1-x}Ca_xMnO_3$ the undoped $LaMnO_3$ is a Mott insulator containing JT ions Mn^{3+} ($t_{2g}^3 e_g^1$) with $S = 2$. It experiences the cooperative JT transition with orbital ordering T_{oo} at 800 K and becomes AF ordered at much lower temperature $T_N = 140$ K. With doping of Ca^{2+} ions (hole doping), $Mn^{4+}(t_{2g}^3 e_g^0)$ ions with $S = 3/2$ and without orbital degeneracy can be introduced into the system, instead of the JT ions Mn^{3+}. The temperature of the JT transition or orbital ordering, T_{oo}, decreases rapidly with doping x, and T_N falls too; the phase separation originates from magnetic order changing into some other state, for example, a spin-glass-like state, which is also rather inhomogeneous spatially.

The CMR effect is reached in the FM phase $La_{1-x}Ca_xMnO_3$ at $0.2 < x < 0.5$. In such a compound, the resistivity is semiconductinglike at $\boldsymbol{H} = 0$, but becomes FM metalliclike for $T < T_C$ (Curie temperature). The magnetic field shifts T_c to higher P and broadens the transition. Moreover, in the vicinity of T_c, the resistivity decreases strongly with H, which can reach up to 80%. The P effects on CMR and manganites can induce changes.

1. *P* effect on CMR, Curie *T*, and IMT

P can suppress the CMR and at the same time drive up the T_c and IMT temperature (T_{IM}). Hwang *et al.* (1995) presented a detailed study on the effects of P on the magnetoresistance in doped $LaMnO_3$ at a fixed doping level. In all cases, the application of external P monotonically increased the Curie T. Similarly, Neumeier *et al.* (1995) found that in $La_{1-x}Ca_xMnO_3$ with $x = 0.21, 0.33$, and 0.40, P strongly decreased ρ and drove T_c up at rates as large as 37 K/GPa for the $x = 0.21$ specimen (Fig. 31). The results were interpreted in the framework of the double-exchange interaction involving conduction via magnetic polarons (Neumeier *et al.*, 1995). Postorino *et al.* (2003) used an infrared absorption technique and found the P dependence of T_{IM} in $La_{0.75}Ca_{0.25}MnO_3$ has an exponentially increasing behavior. Then, Kumaresavanji *et al.* (2013) observed similar behaviors in the bilayer manganite system $La_{1.24}Sr_{1.76}Mn_2O_7$ where the T_C and T_{MI} increased with hydrostatic P at a rate of $dT_C/dP = 20.8$ K/GPa and $dT_{IM}/dP = 20$ K/GPa. They also observed an appreciable increase of magnetic moments at low T with increasing P.

2. *P* effect on AF ordering

P favors AF ordering, which can lead to phase separation. Ding *et al.* (2009) used high-P XMCD to probe the Mn K edge and found that the magnetic dichroism signal in $La_{1-x}Ca_xMnO_3$ ($x = 0.25$) gradually decreased with P and disappeared at 23 GPa. Meanwhile the uniaxial compression of the MnO_6 octahedra along the b axis increased continuously with P and became anomalously large at 23.5 GPa. They attributed these changes to a FM-AF transition associated with orbital ordering at high P. The FM-AF transition did not occur immediately but progressed continuously through the phase separation, demonstrating that the AF phase grew out from the FM phase (Ding *et al.*, 2009). Such a P-induced phase separation in $La_{1-x}Ca_xMnO_3$ ($x = 0.25$) was also confirmed by Baldini *et al.* (2012), with neutron diffraction up to 8 GPa. Okada and Yamada (2012) reported P-induced phase separation in $Nd_{0.53}Sr_{0.47}MnO_3$ and $Pr_{1-x}Ca_xMnO_3$ ($0.30 < x < 0.50$). Moreover, Dang *et al.* (2013) observed a FM to AF transition in $Pr_{0.7}Sr_{0.3}MnO_3$ at 2 GPa. Interestingly, Baldini *et al.* (2015) even found a phase separation in undoped $LaMnO_3$; the FM phase grew out from the AF due to the percolation induced by P. This phase separation led to the CMR effect in an undoped $LaMnO_3$.

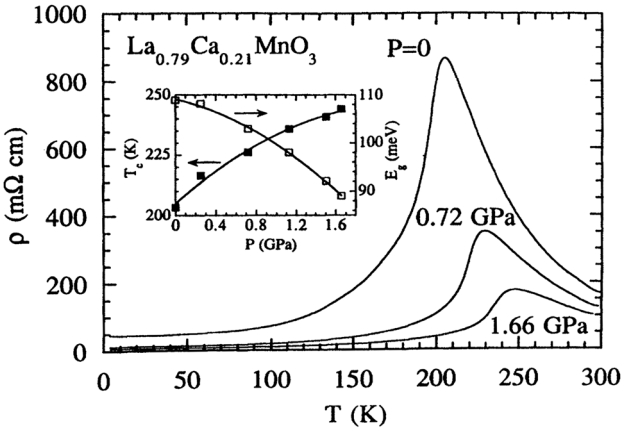

FIG. 31. Resistivity vs T at three hydrostatic P for $La_{1-x}Ca_xMnO_3$ ($x = 0.21$). In the inset the P dependence of the T_c and the activation energy E_g are plotted. From Neumeier *et al.*, 1995.

3. *P* effect on Jahn-Teller distortion in manganites

The P effect on cooperative JT distortion in manganites remains debatable. Using synchrotron XRD, optical spectroscopies, and transport measurements, Loa *et al.* (2001) studied $LaMnO_3$ up to 40 GPa. They observed the cooperative JT distortion continuously reducing with increasing P. There was a strong indication that the JT effect and the concomitant orbital ordering were completely suppressed above 18 GPa. The system retained its insulating state to 32 GPa, supporting the view that $LaMnO_3$ is a classic Mott insulator. Recently, using high-P and low-T Raman techniques, Baldini *et al.* (2011) provided the first experimental evidence of JT distortion persistence in $LaMnO_3$ up to 34 GPa over the entire stability range of the insulating phase. They revived the debate on the character of the insulating phase and the origin of the IMT in $LaMnO_3$.

VIII. HIGH-*P* STUDIES OF *f*-ELECTRON SYSTEMS

In addition to the d-electron systems, materials containing rare-earth and actinide elements with partially filled $4f$ and $5f$

shells are f-electron systems that also show a strong electron correlation. One characteristic feature of f electrons is that they are even more localized than d electrons.

In particular, the on-site Hubbard repulsion U of the f electrons is always much larger than the corresponding hopping t, leading to small crystal field splitting (~0.1 eV). In addition, the superexchange interaction between f electrons is usually much weaker than that in transition-metal compounds. This results in very low magnetic ordering T (~1–10 K). A second characteristic feature is that even though f electrons are localized, there are itinerant s, p, or d electrons at nearby energies, forming broad bands. The most fundamental physics of f-electron materials results from the immersion of their magnetic moments in a quantum sea of mobile conduction electrons. The interaction between f electrons and conduction electrons has two consequences: a nonmagnetic state due to the screening of f-electron local moments by conduction electrons, also known as the Kondo effect (Kondo, 1964), or long-range magnetic ordering due to the RKKY interaction (Ruderman and Kittel, 1954).

The Kondo effect consists of hybridization of the f orbitals and conduction bands and leads to the formation of a strongly renormalized Fermi liquid, which is the so-called heavy-fermion regime, whereas the RKKY exchange interaction between two f electrons via the conduction electrons leads to a localized magnetically ordered state of the f electrons. The competition of the Kondo effect and RKKY can lead to commonly observed quantum critical transitions, which are shown in Fig. 32.

Generally speaking, the RKKY interaction is $J_{\mathrm{RKKY}} \sim J_{f\text{-}c}^2/E_F$, where the f-c exchange $J_{f\text{-}c}$ is $\sim V_f^2/|E_f - E_F|$, and V_f is the f-c hybridization; f and c stand for the f electrons and conduction electrons, respectively, while the Kondo temperature T_K is $\sim E_F \exp(-J_{f\text{-}c}/E_F)$. For a deep f level with more localized electrons and thus a small $J_{f\text{-}c}$, the Kondo temperature T_K is exponentially small. In this case, the RKKY interaction usually wins over the Kondo effect, resulting in a magnetic state. This is the situation for most rare-earth metals and compounds. However, if $E_f - E_F$ becomes small, the Kondo effect may become stronger and lead to a heavy-fermion state. Once $E_f > E_F$, the delocalization of the f electrons could lead to a mixed valence state, which resides "in between" the heavy fermion and normal metals with $m^* - 10$–$10^2 m_0$.

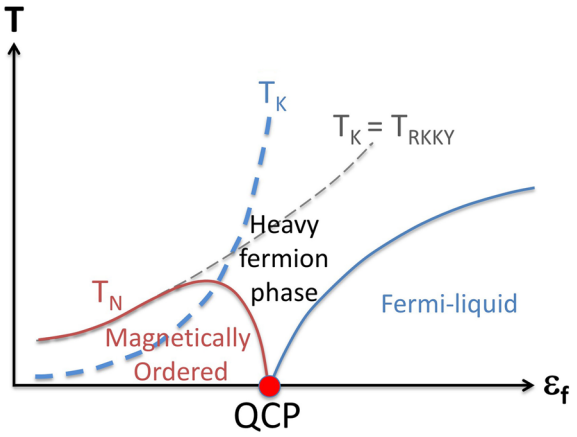

FIG. 32. Generic phase diagram of heavy-fermion systems results from the competition between the Kondo and RKKY interactions. From Doniach, 1977.

P can have significant impacts on both the Kondo effects and RKKY interaction—the two controlling effects on f-electron systems. First, P enhances V_f and changes both the RKKY coupling and the Kondo temperature, but it tends to favor the Kondo effect in theory (Rueff *et al.*, 2006; Khomskii, 2014). For instance, in cerium with only one $4f$ electron, when V_f increases with P, the f electron occupancy n_f significantly deviates from unity, and the double occupancy is expected to increase. Reaching the Kondo regime, a portion of $1 - n_f$ f electrons is delocalized that could lead to a mixed valence state (Rueff and Shukla, 2010). The second effect of P is to delocalize the f electrons, which directly affects the electronic screening and vibrational entropy. Both effects can cause dramatic changes of f-electron systems, but sometimes it is not easy to differentiate the effects.

A. Volume collapse and mixed valence in f-electron materials

Many trivalent rare-earth metals undergo a dramatic high-P transformation, which is generally believed to arise from a change of the $4f$ electron correlation. During some transformations, the changes appear abruptly and are accompanied by unusually large volume collapses of 9% to 15%. Similar behavior is also observed in the actinides (Fig. 33).

The P-induced α-γ transition in Ce is an archetypical example of the volume-collapse phenomenon (Ramirez and Falicov, 1971). This isostructural phase transition accompanied by a large volume contraction that ends in a tricritical point is a manifestation of the subtle interactions between the f levels self-consistently embedded in a sea of conduction electrons. However, its mechanism remains under debate in

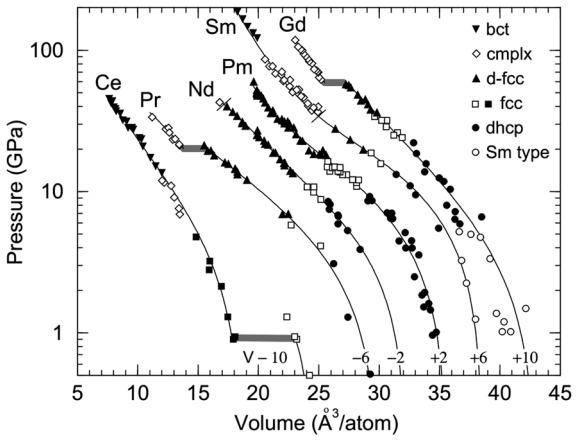

FIG. 33. P-V systematics for the rare-earth elements. "cmplx" denotes a number of complex, low-symmetry structures. The volume-collapse transitions are marked with thick horizontal hatched lines for Ce, Pr, and Gd, and thin lines perpendicular to the curves denote the d-fcc to the $hP3$ symmetry change in Nd and Sm. The curves are guides to the eye. Note that the data and curves have been shifted in volume by the numbers (in the Å^3/atom) shown at the bottom of the figure. From McMahan *et al.*, 1998.

spite of tremendous efforts during the past four decades (Johansson, 1974; Allen and Martin, 1982; McMahan, Held, and Scalettar, 2003; de' Medici *et al.*, 2005). The anomalous behavior of Ce at the transition is commonly described by two possible scenarios. The first was suggested early on by Johansson (1974) and based on the concept of a Mott transition within the f-electron subspace, which may still be relevant in this context. The other view is the Kondo volume-collapse model (Allen and Martin, 1982; Allen and Liu, 1992), in which the transition is driven by the change in the hybridization between the two phases with different unit-cell volumes. Recent theoretical analyses point to an intermediate behavior at finite temperature in either phase, with electron correlations and screening as mandatory components (McMahan, Held, and Scalettar, 2003; de' Medici *et al.*, 2005) Recent experiments suggested that the electronic structure changes resulted mainly from band formation of the $4f$ electrons, which concurs with reduced electron correlation and increased Kondo screening at high P (Rueff *et al.*, 2006). However, to date experiments still cannot agree on which theory is correct for deciphering the puzzle of the α-γ transition. The relationship between the Kondo volume collapse and quantum criticality was discussed by Dzero *et al.* (2006), where the situation of the end point suppressed to $T = 0$ was considered.

In the $Ce_{75}Al_{25}$ metallic glass, Zeng *et al.* (2010) observed that the Ce $4f$ electron transformed from its ambient localized state to an itinerant state above 5 GPa, which was also accompanied by a volume collapse of about 8.6%. They attributed these changes to $4f$ electron delocalization. The transition led to a new type of electronic polyamorphism in densely packed metallic glass dictated by the Ce constituent, which is fundamentally distinct from the conventional structural polyamorphism resulting from coordination change and atomic rearrangement (Zeng *et al.*, 2010).

The mixed valence is another interesting feature of f-electron materials. It describes the effect of coherent quantum fluctuations within a restricted set of valence configurations, such as the fluctuations between the Ce^{3+}/Ce^{4+}, Eu^{2+}/Eu^{3+}, and Yb^{2+}/Yb^{3+}. While the majority of isolated lanthanide atoms are in the trivalent state, Ce, Eu, and Yb appear also in other states, due to the relative stability of their unfilled (i.e., Ce^{4+}), half-filled (i.e., Eu^{2+}), or completely filled (i.e., Yb^{2+}) orbitals. The application of sufficient P would prompt Ce, Eu, and Yb to become trivalent. However, so far only a mixed valence state has been observed in Eu and Yb at high P.

At ambient P Eu metal is divalent and is AF ordered at 90 K. Superconductivity in Eu at P above 35 GPa was predicted more than 30 years ago by Johansson and Rosengren (1975), who estimated this P to be sufficient to push Eu to full trivalency. Recently Debessai *et al.* (2009) observed superconductivity in Eu above 75 GPa. Theoretical estimation of the P necessary for a full divalent-to-trivalent valence transition in Eu ranges from 35 GPa (Johansson and Rosengren, 1975) to 71 GPa (Min *et al.*, 1986). Experimentally, Röhler (1986) measured the XANES at the Eu $L3$ edge to P as high as 34 GPa and reported that its valence increased sharply under P, reaching ~2.5 at 10 GPa and saturating at ~2.64 at higher P. In addition, measurements of the Eu IS with ^{151}Eu Mössbauer spectroscopy to 14 GPa at 44 K led Farrell and Taylor (1987) to conclude that the Eu valence increases rapidly under P, reaching ~2.45 at 12 GPa. Their measurement of the hyperfine field at 44 K and 12 GPa revealed that magnetic ordering was still present, in agreement with earlier resistivity studies to 15 GPa (Bundy and Dunn, 1981). A more recent synchrotron Mössbauer experiment at ambient temperature by Wortmann *et al.* (2008) also identified an increase in IS to 17 GPa due to a strong increase in the Eu valence. However, recent studies by Bi *et al.* (2011, 2012) on Eu up to ~100 GPa indicate that Eu metal still remaining in a mixed valence state never reaches a trivalent state. In contrast, the Eu ion in $EuAu_2Si_2$ could stabilize only in a divalent magnetic state to 3 GPa (Abd-Elmeguid, Sauer, and Zinn, 1985; Abd-Elmeguid *et al.*, 1985). Such abnormal mixed valence behaviors require more research to understand their underlying physics.

B. Quantum criticality and quantum phase transition

Since the original discovery of heavy-fermion behavior in the f-electron compound $CeAl_3$ by Andres, Graebner, and Ott (1975), a diverse range of heavy-fermion compounds, including superconductors, antiferromagnets, and insulators, has been discovered. These materials have become the focus of intense interest with the discovery that intermetallic antiferromagnets can be tuned through a quantum phase transition into a heavy-fermion state by P, as well as magnetic fields or chemical doping (Stewart, 2001, 2006; Miranda and Dobrosavljevic, 2005; von Löhneysen *et al.*, 2007). During these quantum phase transitions, the point where the AF ordering T is driven continuously to zero is defined as a "quantum critical point" (QCP) (Fig. 32).

von Löhneysen *et al.* (1994) discovered that one can tune $CeCu_{6-x}Au_x$ through an AF QCP and then reverse the process by the application of P. These experiments showed that a heavy electron metal develops "non-Fermi-liquid" properties at a QCP, including a linear T dependence of the resistivity and a logarithmic dependence of the specific heat coefficient of T. Shortly thereafter Mathur *et al.* (1998) showed that when P is used to drive the antiferromagnet $CeIn_3$ through a quantum phase transition, superconductivity develops in the vicinity of the quantum phase transition. P-tuned quantum phase transition and QCP have also been observed in other heavy-fermion metals such as $CeCu_2Si_2$ (Küchler *et al.*, 2003) and $CeRhIn_5$ (Shishido *et al.*, 2005).

P-tuned "quantum critical superconductors" then emerged. For example, $CeIn_3$ develops superconductivity at the AF QCP at 2.5 GPa. $CeCu_2(Si, Ge)_2$ has two islands, one associated with the AF state at low P and another at higher P thought to be associated with critical valence fluctuations (Yuan *et al.*, 2003, 2006). Later Rueff *et al.* (2011) measured the Ce L_3 edge and detected a clear increase of the Ce valence with P. In addition, they also found a weak electron transfer and a continuous valence change under P, suggesting a crossover regime with the hypothetical valence line terminating at a critical end point close to zero. Meanwhile, Bauer *et al.* (2010) found that applying P to $CePt_2In_7$ can also induce a broad dome of superconductivity that coexists with magnetic order at 1–3 GPa. The maximum

$T_c = 2.1$ K appears near the critical P of 3.5 GPa, where the Néel temperature extrapolates to 0 K. An analysis of the initial slope of the upper critical field, the T^{-2} dependence of the electrical resistivity, and specific heat indicates an enhancement of the effective mass m^* as the critical P is approached, suggesting that critical fluctuations may mediate superconductivity.

The f-electron compound $CeAuSb_2$ crystallizes in the $ZrCuSi_2$-type tetragonal structure and AF orders between 5 and 6.8 K, where its AF transition temperature T_N depends on the occupancy of the Au site. Seo *et al.* (2012) reported that the magnetic transition T is initially suppressed by P, but it is intercepted by a new magnetic state above 2.1 GPa. The new phase shows a dome shape P-T stability field and coexists with another phase above 4.7 GPa. The electrical resistivity shows a T^{-2} Fermi-liquid behavior. The residual resistivity and the T^{-2} resistivity coefficient increase with P, suggesting the possibility of a magnetic QCP at higher P.

C. Superconductivity

Before 1970, conventional wisdom regarded magnetism and superconductivity mutually exclusive. Early work on the interplay of the Kondo effect and superconductivity by Maple *et al.* (1972) suggested that the Kondo screening suppressed the pair breaking effects of magnetic moments, but the implication of these results was only slowly digested. Since the discovery of superconductivity in $CeCu_2Si_2$ (Steglich *et al.*, 1979), the list of known heavy-fermion superconductors is growing rapidly. More details about the P-induced superconductivity in heavy-fermion systems can be found in Sec. X.G.

IX. HIGH-P STUDIES ON TOPOLOGICAL INSULATORS

Among various tuning tools such as doping and magnetic fields, P is clean and effective for the exploration of topological superconductivity. The concept of topological superconductors resembles that of topological insulators, exhibiting a full pairing gap in the bulk and metallic surface state with the Majorana fermion. Topological insulators require both spin-orbital coupling and time-reversal symmetry. An ideal topological insulator should exhibit an insulating bulk state and a robust surface or edge state. Such interesting characteristics have been well determined in two-dimensional HgCdTe quantum (Roth *et al.*, 2009), three-dimensional crystals of $Bi_{1-x}Sb_x$ (Hsieh *et al.*, 2008), and the group VI-V binary compounds Bi_2Se_3 (Xia *et al.*, 2009), Bi_2Te_3 (Chen *et al.*, 2009), and Sb_2Te_3 (Hsieh *et al.*, 2009).

The possible realization of topological superconductivity is fundamentally important not only for understanding their novel states but also for constructing topological quantum computers (Qi and Zhang, 2011). It seems natural to obtain topological superconductors from topological insulators with the expectation of maintaining the topological state. The discovery of superconductivity in copper-doped Bi_2Se_3 (Hor *et al.*, 2010), which was proposed to be a topological superconductor (Fu and Berg, 2010), attracts much interest. However, the issue regarding whether $Cu_xBi_2Se_3$ is a topological superconductor or not remains under fierce debate. Meanwhile, homogeneous bulk superconductivity in three-dimensional topological insulators is rather difficult to obtain merely by doping.

Recent electronic studies (Zhang *et al.*, 2011; Matsubayashi *et al.*, 2014) revealed that Bi_2Te_3 exhibited a superconducting transition at different P with different P-transmitting media, while all structure measurements showed that the first structural transition occurs around 8 GPa. Thus, determining the exact P for the superconducting transition is the key to settling whether Bi_2Te_3 can be a topological superconductor. The superconducting transition that followed the first structural transition is more reliable because helium was used as a P-transmitting medium.

An electrical transport study (Kirshenbaum *et al.*, 2013) on the topological insulator Bi_2Se_3 revealed superconductivity above 11 GPa with both the transition temperature T_c and upper critical field H_{c2} increasing with P up to 30 GPa, where they reached the maximum values of 7 K and 4 T, respectively. The T_c remained anomalously constant at higher P, and the carrier concentration (measured using the Hall effect) increased continuously (Fig. 34). This, together with the quasilinear T dependence of H_{c2}, suggests an unconventional P-induced pairing state in Bi_2Se_3 that is unique among the superconducting topological insulators.

Detailed structural studies (Vilaplana *et al.*, 2011) on compressed Bi_2Se_3 show that its structure evolves from rhombohedral (R-3m) to monoclinic ($C2/m$) near 10 GPa, and transforms to a bcc-like ($C2/m$) structure near 28 GPa. Considering that a superconducting transition happens around 11 GPa, the corresponding structure for superconductivity should be monoclinic. In this case, new theories and further experiments are required to clarify whether Bi_2Se_3 with such a monoclinic structure would still keep its topological characteristics.

When using hBN fine powders as a P-transmitting medium, Sb_2Te_3 quickly exhibited a trace of superconductivity around 4 GPa and zero resistance around 6.8 GPa, indicating a

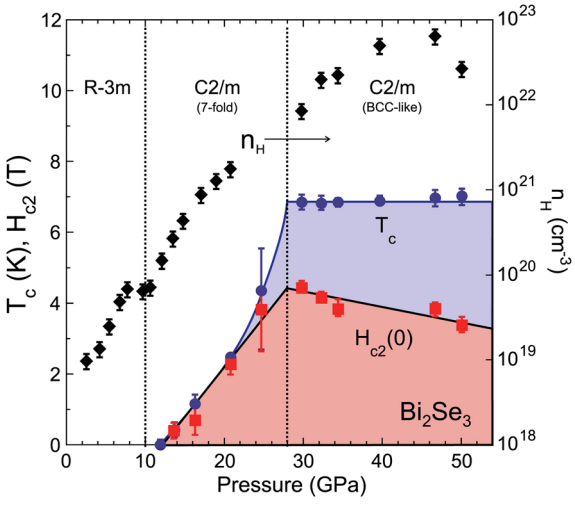

FIG. 34. Phase diagram of Bi_2Se_3 showing the evolution of carrier concentration n_H (diamonds), T_c (circles), and upper critical field H_{c2} at zero temperature (squares) as a function of P for field orientation along the crystallographic c axis of the ambient-P structure. From Kirshenbaum *et al.*, 2013.

promising topological superconductor under P (Zhu *et al.*, 2013). However, the nonhydrostatic hBN medium would cause crystal lattice distortion to reduce the c axis much faster than the a and b axes. Thus, experiments with better P-transmitting media are highly desired to examine whether the superconductivity occurs after the structural transition as in the case of Bi_2Te_3 (Zhang *et al.*, 2011).

Whether group V_2VI_3 topological insulators could become topological superconductors remains controversial. More candidates for topological superconductors would be helpful. Bismuth-tellurohaides BiTeX (X = Cl, Br, and I), the so-called Rashba semiconductors, resemble V_2VI_3 and exhibit similar structures and spin-orbital coupling (Sakano *et al.*, 2013). Among them, BiTeI is theoretically proposed to be a new inversion-asymmetric topological insulator under P (Bahramy *et al.*, 2012). The existence of a Dirac-Fermi surface in another Rashba semiconductor BiTeCl was unveiled by angle-resolved photoemission spectroscopy and scanning tunneling spectroscopy studies (Chen *et al.*, 2013). These techniques provided evidence for BiTeCl as an inversion-asymmetric topological insulator. One possible explanation is that the surface charge in single crystal BiTeCl induced by structural inversion asymmetry is equal to the applied P (Chen *et al.*, 2013). Thus, BiTeX is naturally expected to be a possible candidate for topological superconductivity under compression.

The resistance measurements (Ying *et al.*, 2016) on single crystal BiTeCl under P showed the evolution from metallic to insulating behavior. Superconductivity occurred within the insulating state after the suppression of the resistivity maximum around 13 GPa. The insulating behavior of BiTeCl might correspond to that of the topological insulators. The closeness of this superconductivity and insulating behavior indicates a possible topological superconductor.

X. HIGH-P STUDIES OF SUPERCONDUTIVITY

After a century of intense investigation, surprising discoveries still often appear in the field of superconductivity, and many unanswered problems remain. High P provides a fertile ground for exploring the ever-higher superconducting transition temperature (T_c), and tuning various electronic, magnetic, and structural interactions for testing alternative theories. At high P, unusual elemental superconductors such as sulfur (Struzhkin, Hemley *et al.*, 1997), boron (Eremets *et al.*, 2001), and lithium (Struzhkin *et al.*, 2002) were discovered. In studies of high-T_c cuprate superconductors, P has been used to achieve the record high T_c of 164 K (Gao *et al.*, 1994a), to tune an underdoped cuprate over its critical point (Cuk *et al.*, 2008), and to drive competition in the electronic order thus creating the second maximum beyond the optimal doping (Chen *et al.*, 2010).

The P variable is particularly powerful for studying the complex iron-based superconductors in which a large magnetic moment coexists with superconductivity (Dagotto, 2013). With increasing P, the T_c tunes through the maximum (33 K) of a parabolic-shaped curve and vanishes at a quantum critical point in $(K, Tl)_{1-x}Fe_2Se_{2-y}$, then suddenly and unexpectedly the T_c reemerges as a second crest at 48 K (Sun *et al.*, 2012). This behavior provides clues and connections to many enigmatic features in this system, including the magnetic superlattice, electronic charge, orbital and spin degrees of freedom, spin fluctuation, and QCP (Guo *et al.*, 2012).

A. Elemental superconductors

Significant advances have been made in the past decades in the development of a new generation of electrical transport as well as magnetic susceptibility studies at high P. These new methods are being combined with low T and high magnetic field to study superconductivity. The application of P has driven 22 elements that are not superconducting at ambient P to become superconducting. P can increase the T_c through modifications of substances already known to be superconducting. Among all elements discovered so far, calcium holds the record high T_c above 20 K accompanied by superconductivity fluctuation at 29 K at P of 216 GPa (Sakata *et al.*, 2011).

The experimental effort in exploring superconductivity in calcium by the application of P began in 1981. When measuring the T dependence of resistivity from 2 to 300 K, Dunn and Bundy (1981) observed a small superconductinglike drop near 2 K at 44 GPa. Okada *et al.* (1996) performed detailed resistivity measurements at P up to 150 GPa. A clear superconducting transition was observed starting at 50 GPa with suppression by external fields. The T_c was found to increase monotonically with P, reaching 15 K at 150 GPa. Combining x-ray diffraction and resistivity measurements (Sakata *et al.*, 2011) revealed that calcium actually possesses a surprisingly high T_c above 20 K at 216 GPa in its VII phase (Fig. 23). The continuous increase of T_c with P gives hope to achieving an even higher T_c at higher P. P-induced superconductivity and later enhancement in calcium may result from a variety of lattice distortion and associated phonon anomalies (W. L. Mao *et al.*, 2010).

Vanadium is a superconductor with a T_c of 5.4 K at ambient P but displays an evolution behavior with P similar to calcium. The vanadium group elements (V, Nb, Ta) have large positive P derivatives of the T_c. This increase of T_c with P holds for vanadium up to 120 GPa, where T_c reached a plateau of 17.2 K, probably due to a structural transition and Fermi surface nesting (Ding *et al.*, 2007).

Exploring new elemental superconductors in the GPa regime turned out to be very fruitful. For example, sulfur transforms to a metal near 100 GPa which is superconducting with an initial T_c of 14 K. The T_c increases to 17 K at 160 GPa, as detected by the magnetic susceptibility technique (Struzhkin, Hemley *et al.*, 1997). These studies allow the discovery of new classes of simple elemental superconductors that were experimentally inaccessible previously. The metallization of oxygen reported at 95 GPa, based on optical measurements, was confirmed by electrical conductivity. A low-T study revealed superconductivity of the metallic oxygen with $T_c = 0.6$ K (Shimizu *et al.*, 1998). Boron provides an additional example. First-principles calculations predicted that the array of the icosahedra boron structure breaks down near 200 GPa to form a metallic solid. The conductivity of boron was measured as a function of P up to 250 GPa (Eremets *et al.*, 2001) and exhibited a metallic state near 175 GPa. The

metallic phase was superconducting with a T_c of 6 K which increased remarkably with P to 11.5 K at 250 GPa.

As the lightest of alkali metals in group IA with only a single 2*s* electron, lithium was generally regarded as the simplest of all metals. At normal P-T conditions, its properties are well described with a near-free-electron-gas model. However, this simplest metal behaves in complex ways at the extreme conditions of low T and high P. Theoretical calculations (Neaton and Ashcroft, 1999) suggested that lithium could undergo several structural transitions, possibly leading to a "paired atom" phase with low symmetry and near-insulating properties. X-ray diffraction studies (Hanfland *et al.*, 2000) revealed a structure similar to the predicted paired structure. Superconductivity in lithium was reported to appear above 30 GPa by two groups (Shimizu *et al.*, 2002; Struzhkin *et al.*, 2002). The T_c was found to range from 9 to 16 K at P from 23 to 80 GPa. Later magnetic measurements (Deemyad and Schilling, 2003) showed that the superconducting phase exists in the P range between 20 and 60 GPa with a maximum T_c at P around 30 GPa, indicating the correlation of superconductivity with structural transitions. The observation of high T_c in dense lithium confirms the expectation that an element with low atomic numbers will have a high T_c. Compressing lithium near 80 GPa drives it to an unexpected semiconducting state (Matsuoka and Shimizu, 2009). This provides an example of driving a near-free-electron-gas metal to an insulating state solely through external P. Multiple phases in P-T phase diagrams exist, as shown in Fig. 24 (Guillaume *et al.*, 2011). Interestingly, lithium reverts to a metallic state above 120 GPa (Matsuoka *et al.*, 2014). Whether lithium would reenter a new superconducting phase at higher P in this new metallic state calls for further studies.

The occurrence of superconductivity in lithium at high P encourages the exploration of superconductivity in other group (IA) elements. For several decades, searching for possible superconductivity in dense hydrogen with very high T_c is the main motivation for the development of modern high-P science and technology. However, the currently available static P apparatuses based on DAC are still difficult for detecting the expected superconductivity in dense hydrogen.

Modern theoretical calculations on hydrogen (Pickard, Martinez-Canales, and Needs, 2012) suggested that the structure with space group *Cmca*-12 is stable at P above 280 GPa and T below 350 K. Superconductivity was predicted for the molecular metallic *Cmca* phase by increasing the T_c from 75 to 345 K when P is changed from 415 to 450 GPa (Cudazzo *et al.*, 2008). A crossover from a molecular to an atomic transition was also predicted theoretically (Azadi *et al.*, 2014). The corresponding molecule phase was suggested to have a structure with a space group of *Cmca*-12, while the atomic phase has a structure with space group $I4_1/amd$. This atomic phase was suggested to be a high-T_c superconductor from theoretical calculations (McMahon and Ceperley, 2011). The highest T_c can be reached at 360 K at 1 TPa. At higher P near 3 TPa, the T_c was also calculated to approach 425 K in another atomic phase R-3m (McMahon and Ceperley, 2011). For fluid metallic hydrogen at high P and high T, Jaffe and Ashcroft (1981) obtained the T_c at different P comparable to those for solid metallic hydrogen. Thus, no matter what the metallic state is, the dense metallic hydrogen should be a high-T_c superconductor. Experimental tests of these theoretical predications and the determinations of such high T_c are highly desirable. It is conceivable that the breakthrough of finding superconductivity at room T or even higher T in metallic hydrogen is approaching. Because of the possible existence of both the fluid and superconductivity states, one can also hope to realize the theoretically predicted superconducting superfluid (Babaev, Sudbø, and Ashcroft, 2004, 2005). All these predictions wait for high-P experimental exploration.

It has been established that the Earth's core is predominantly made of iron. At P above 13 GPa, iron is known to transform to a nonmagnetic structure and the possibility of superconductivity in this state has been predicted. Superconductivity in iron was observed to appear after the establishment of the nonmagnetic state at 15 GPa, which is close to the beginning of the bcc to hcp structural transition (Shimizu *et al.*, 2001). The P dependence of T_c is below 2 K in the P range between 15 and 30 GPa.

The latest observations of superconductors composed of very light elements with relatively high T_c at high pressures are indeed exciting and important. The light weight of these elements is in favor of the relatively high phonon energies. Both the electronic density of states and the electron-phonon coupling interaction can also be enhanced by extensive lattice compression. All these effects contribute to the high T_c in these elements.

B. Superconductivity in hydrogen-rich systems

The overlapping bands of compressed hydrides are wide, the density of states are generally high, and the electron-ion interactions from protons and group IVA ions are significant. The higher frequencies associated with the protons will lead to a high Debye T. Thus, the metallic group IVA hydrides are expected to have high values of T_c. By comparing the case of superconducting MgB_2, Ashcroft (2004) further suggested stable metallic states in the dense IVA hydrides at P considerably lower than those necessary for metallization of hydrogen. Since then, extensive experimental and theoretical investigations have been undertaken to examine this prediction on hydrogen-rich systems, especially the group IVA hydrides, such as methane (CH_4), silane (SiH_4), germane (GeH_4), stannane (SnH_4), and plumbane (PbH_4).

Theoretical simulations (Ancilotto *et al.*, 1997) showed that methane undertakes several phase transformations upon compression and could decompose into carbon and hydrogen or other hydrocarbons. Fortunately, the P-induced metallization was observed in silane (Chen, Struzhkin *et al.*, 2008) with Drude-like metallic behavior above 60 GPa. A theoretical study revealed (Chen, Wang *et al.*, 2008) that the metallic SiH_4 above 60 GPa is a metastable phase of *Cmca* symmetry. In higher P ranges above 220 GPa, the *Cmca* structure is more favorable and superconducting with a $T_c > 20$ K. Subsequently, the superconductivity of SiH_4 at 17 K in the P range of 96 and 120 GPa was experimentally observed (Eremets *et al.*, 2008). Amorphous silicon, silicon hydrides, or platinum hydrides (Kim *et al.*, 2011; Li *et al.*, 2011) were suggested to account for the observed superconductivity. The issue regarding whether new compounds originating from

SiH_4 (Degtyareva *et al.*, 2007) could be formed and be responsible for metallization and superconductivity remains unsettled.

The high-P metallic behaviors in GeH_4 (Gao *et al.*, 2008) and SnH_4 (Tse, Yao, and Tanaka, 2007) have also been predicted theoretically. A high-P superconducting phase of SnH_4 was predicted to be stable between 70 and 160 GPa with a T_c close to 80 K at 120 GPa (Tse, Yao, and Tanaka, 2007). PbH_4 even keeps its metallic character throughout the entire range of P (Zaleski-Ejgierd, Hoffmann, and Ashcroft, 2011). The predicted metallization P of group IVA hydrides decreases with increasing atomic number of the heavy elements. However, no direct experimental evidence was found on metallization of these hydrogen-rich group IVA compounds. An experimental study on GeH_4 revealed the dissociation to germanium and hydrogen under P (Chen *et al.*, 2011). The task of experimentally and theoretically determining the structural and superconducting properties of these materials at high P remains challenging.

An important message delivered from extensive theoretical calculations on group IVA hydrides is the existence of the quasimolecular "H_2" units at high P. Such H_2 units might be important for superconductivity and experimental efforts were soon devoted to H_2-containing compounds, including CH_4-H_2 (Somayazulu *et al.*, 1996), SiH_4-H_2 (Strobel, Somayazulu, and Hemley, 2009; Wang *et al.*, 2009), and GeH_4-H_2 (Strobel *et al.*, 2010). Significant intermolecular interactions between H_2 and SiH_4 were observed in the SiH_4-H_2 compound, indicating a strong covalent bonding interaction in the SiH_4-H_2 system. Raman and infrared spectroscopic measurements on $GeH_4(H_2)_2$ (Strobel *et al.*, 2010) showed a substantial softening of multiple H_2 modes compared to the bulk solid hydrogen. With increasing P, the frequencies of several Raman and infrared H_2 modes decreased, indicating an anomalous attractive interaction for closed-shell and nonpolar molecules. Interestingly, theoretical studies established that these H_2-containing compounds were superconducting under P with T_c as high as 100 K. $SiH_4(H_2)_2$ was predicted to superconduct with a T_c of 107 K at 250 GPa (Li *et al.*, 2010), $GeH_4(H_2)_2$ has a T_c of 95 K at 220 GPa (Zhong *et al.*, 2012), and $PbH_4(H_2)_2$ possesses a T_c of 107 K at 230 GPa (Cheng *et al.*, 2015). Such high-T_c values in the XH_4-H_2 systems are attractive, particularly the calculated P required for introducing superconductivity following a decreasing trend from light to heavy elements: from 248 GPa for $SiH_4(H_2)_2$, 220 GPa for $GeH_4(H_2)_2$, to 133 GPa for $PbH_4(H_2)_2$. These results indicate that the softening of the intermediate frequency phonons induced by inserted H_2 molecules is the main origin for the high T_c. These studies offer a clue to understanding the potential realization of a high T_c in metallic hydrogen and hydrogen-rich materials.

For a H_2-containing compound $(H_2S)_2H_2$, Duan *et al.* (2014) predicted that the Im-$3m$ phase would yield a high-T_c value of 204 K at 200 GPa, which is much higher than H_2-containing compounds based on group IVA hydrides. Excitingly, Drozdov *et al.* (2015) reported a similar T_c in the sulfur hydride system, although this experimental study was inspired by the theoretical prediction of Li *et al.* (2014). The new T_c record, as high as 200 K, was established in a hydrogen-rich compound.

Figure 35 summarizes the results of the temperature-dependent resistance measurements at various P and the determined T_c as a function of P for sulfur hydride and sulfur deuteride (Drozdov *et al.*, 2015; Einaga *et al.*, 2016). The results show a peak at 150 GPa for sulfur hydride and 160 GPa for sulfur deuteride, separating the low- and high-P phases. The lower T_c values in sulfur deuteride than those in sulfur hydride yield a sizable isotope effect, indicating a significant electron-phonon interaction. This suggests that phonon-mediated superconductivity can occur at such a high T_c around 200 K.

The observed superconductivity from the T-dependent resistance measurements with zero resistance in the superconducting state in sulfur hydride and sulfur deuteride received further support from magnetic detections. Drozdov *et al.* (2015) observed the superconducting transition at 203 K at 155 GPa from their magnetization measurements. Using synchrotron Mössbauer spectroscopy, Troyan *et al.* (2016) demonstrated that the superconducting sulfur hydride effectively shields the strong magnetic field of about 0.7 T up to temperatures of 90 to 100 K at 153 GPa, revealing a superconducting state below 100 K. It should be noted that there is almost a 100 K difference for the obtained T_c at almost the same P. These exciting results present a shortcut for exploring higher T_c materials from hydrogen-rich systems. Further magnetic measurements are needed to understand this difference. So far, consistent T_c values have not been obtained from the zero-resistance and magnetic susceptibility measurements.

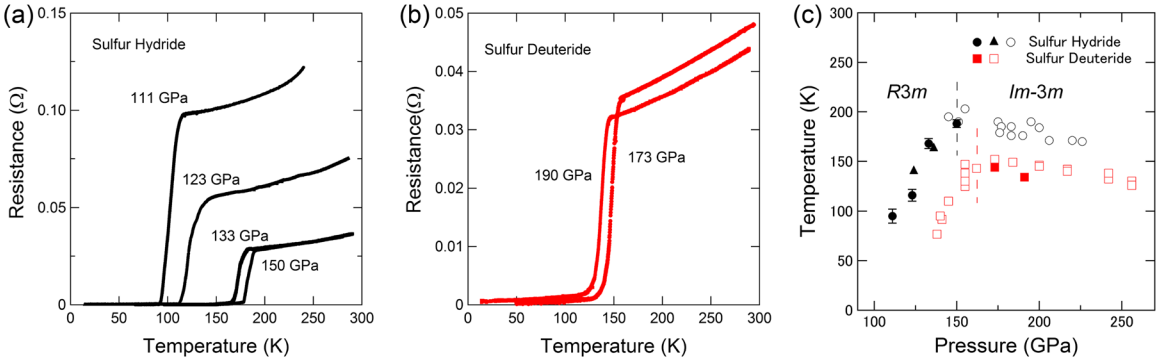

FIG. 35. T dependence of resistance in (a) sulfur hydride and (b) sulfur deuteride. (c) P dependence of superconductivity T_c of sulfur hydride and sulfur deuteride. The determined T_c values are denoted by filled symbols. Open circles and squares are taken from Drozdov *et al.* (2015). Broken lines indicate the phase boundary between the $R3m$ and Im-$3m$ structural phases. From Einaga *et al.*, 2016.

In 2016, three teams reported the structural properties of the superconducting phases of sulfur hydride from XRD investigations (Einaga *et al.*, 2016; Goncharov *et al.*, 2016; Li *et al.*, 2016). Li *et al.* (2016) observed the presence of H_3S and H_4S_3 through decomposition of H_2S and coexistence with residual H_2S in the P range of 27–140 GPa. However, theoretical calculations indicate that H_4S_3 is not superconducting. XRD experiments combined with electrical resistance measurements at both room and low T by Einaga *et al.* (2016) revealed that the superconducting phase is mostly in good agreement with the theoretically predicted bcc structure of H_3S (Duan *et al.*, 2014). The presence of elemental sulfur was also detected in their XRD patterns, thus proving the decomposition mechanism of H_2S to $H_3S + S$ under P. They concluded that the highest critical temperature of 203 K (Drozdov *et al.*, 2015) corresponds to the Im-$3m$ phase. The low-P and high-P phases shown in Fig. 35(c) are suggested to have the space groups of $R3m$ and Im-$3m$, respectively.

Meanwhile, low- (180 K) and room-T XRD and Raman spectroscopic investigations to 150 GPa conducted by Goncharov *et al.* (2016) revealed an increasing instability of H_2S with P and the formation of hydrogen sulfides with a different structure and composition, including the theoretically predicted $Cccm$ and body-centered cubiclike ($R3m$ or Im-$3m$) H_3S (Duan *et al.*, 2014). The experimental results are also supported by theoretical structure searches that suggest the stability of H_3S, H_4S_3, H_5S_8, H_3S_5, and HS_2 compounds at elevated P.

The hydrogen-rich compounds thus serve as promising candidates for realizing high-T_c superconductivity. The search has been focused on compounds containing a large fraction of atomic hydrogen. Electron-phonon calculations (Li *et al.*, 2015) revealed the YH_6 with estimated superconductive T_c of 251–264 K at 120 GPa. Hoping to turn hydrogen into an alkali metal, research efforts have focused on high-P hydrogen-rich alkali-metal hydrides. Zurek *et al.* (2009) predicted the stability ranges of LiH_2, LiH_6, and LiH_8 at 130–300, 140–300, and 100–200 GPa, respectively. Struzhkin *et al.* (2016) experimentally synthesized NaH_3 and NaH_7, and Pepin *et al.* (2017) synthesized FeH_3 and FeH_5. However, superconductivity has not yet been confirmed in these materials.

C. Transition-metal dichalcogenides

Transition-metal dichalcogenides (TMDs) are a class of materials with the formula MX_2, where M represents a transition-metal element from group IV (Ti, Zr, Hf), V (V, Nb, or Ta), or VI (Mo, W), and X is a chalcogen (S, Se, or Te). Depending on the combination of metal and chalcogen, TMDs offer a wide range of physical and electronic properties. They can be insulators such as HfS_2, semiconductors such as MoS_2, semimetals such as $TiSe_2$, or metals such as TaS_2 and $TaSe_2$.

Several TMDs have superlattice structures that are attributed to the formation of CDWs (Moncton, Axe, and Di Salvo, 1975; Wilson, Di Salvo, and Mahajan, 1975). CDW distortions have been observed in TMDs with group V metals, e.g., $2H$-TaS_2, $2H$-$TaSe_2$, and $2H$-$NbSe_2$, which are known to be superconducting. With decreasing T the crystal becomes a CDW phase. Different models were proposed to explain the CDW formations. The most common one is Fermi surface nesting, although the importance of van Hove singularities, electronic states away from the Fermi level, the JT effect, or excitonic origin were also emphasized.

Usually, the CDW lock-in temperature T_{CDW} is higher than T_c. The application of P often decreases the T_{CDW} and increases T_c (Moliniè, Jérome, and Grant, 1974; Berthier, Molinie, and Jérome, 1976). After the complete melting of the CDW phase, the T_c always reaches a maximum before decreasing upon further compression (Suderow *et al.*, 2005; Feng *et al.*, 2012; Tissen *et al.*, 2013). Understanding the relationship between the CDW and superconductivity is essential to unravel the mechanism of unconventional superconductivity in many layered materials such as cuprates, due to the similarity of their phase diagrams. Here we show how P tunes the structural, electronic, and superconducting properties of TMD materials.

The superconductivity discovered in copper-intercalated $1T$-$TiSe_2$ (Morosan *et al.*, 2006) through the suppression of the CDW order is interesting. It highlights the possible connection between superconductivity and the CDW state, which has been proposed as an example of an exciton condensate. The interplay between superconductivity and the CDW state in pure $1T$-$TiSe_2$ was also examined through the lattice compression up to 10 GPa (Kusmartseva *et al.*, 2009). It was found that at a critical P of 2 GPa a superconducting phase sets in with a maximum T_c of 1.8 K and persists up to 4 GPa. Comparisons of the normal state and superconducting properties of the two systems reveal the possibility that the emergent electronic state qualitatively depends on the manner in which the CDW state is destabilized, making this a unique example where two different superconducting domes are obtained by two different methods through intercalation or P from the same parent compound.

In $1T$-$TiSe_2$, both P and doping can be used to melt the CDW order. In either case, a superconducting dome appears in the phase diagram near the point where the CDW melts. A high-P x-ray scattering study (Joe *et al.*, 2014) directly detected the emergence of the CDW domain walls above the superconducting dome in $1T$-$TiSe_2$. The experiments supported the existence of a QCP at $P_c = 5.1 \pm 0.2$ GPa, which is more than 1 GPa beyond the end of the superconducting region. These results suggest that superconductivity in $1T$-$TiSe_2$ may not be connected to the QCP itself, but to the formation of the CDW.

$1T$-TaS_2 provides another example for examining how the CDW order and superconductivity coexist and compete. At ambient P and low T, $1T$-TaS_2 is in the commensurate CDW (CCDW) phase. Theoretical calculations indicate that this phase should be metallic, with the Fermi level in the middle of a narrow d band. However, the resistivity measurements revealed insulating characteristics. Thus, this material is believed to simultaneously undergo CCDW and Mott transitions. By applying P, the material adopts a nearly commensurate CDW (NCCDW) phase and superconductivity develops within the NCCDW state (Sipos *et al.*, 2008). Superconductivity persists at high P even after the CDW order disappears.

Compressed $1T$-TaS_2 shares a similar phase diagram with $1T$-$TiSe_2$ (Kusmartseva *et al.*, 2009). In both cases

superconductivity occurs when the CDW state is suppressed and enhances after the disappearance of the CDW state. Since the T_c almost remains constant at high P, the CDW and superconducting phases are suggested to separate in real space. Compared with the P-driven enhancement of superconductivity at the expense of the CDW order in the sister system $2H$-TaS_2, which is a superconductor at ambient P, the connection between the CDW state and superconductivity should work well for these TMDs. In the CDW state, a gap opens up over part of the Fermi surface in the direction of the $\boldsymbol{q}$ vectors of the CDW. This reduces the average density of states at the Fermi surface. Upon compression, the CDW is suppressed. The amplitude of the CDW lattice distortion will also be suppressed, therefore gradually restoring the Fermi surface and increasing the T_c accordingly.

Among the TMDs with CDW instabilities, $2H$-$NbSe_2$ has attracted particular attention because of the coexistence and possible interaction of the CDW state and superconductivity. As first revealed by neutron scattering (Moncton, Axe, and Di Salvo, 1975), the quasi-two-dimensional layer compound $2H$-$NbSe_2$ undergoes a second-order phase transition to an incommensurate CDW phase at 33 K and then superconductivity at 7.2 K. X-ray scattering studies (Du *et al.*, 2000) showed no change in the CDW correlation length as a function of the magnetic field, confirming the absence of magnetic effects. Spectroscopy evidence (Kiss *et al.*, 2007) was provided for maximized superconductivity at points in momentum (k) space that are directly connected by the CDW ordering vector. The results demonstrate that the charge order can boost superconductivity in an electron-phonon coupled system in direct contrast to the prevailing view that it competes only with superconductivity.

Evidence for correlation between the CDW and superconductivity in $2H$-$NbSe_2$ was provided again from high-P studies (Moliniè, Jérome, and Grant, 1974; Berthier, Molinie, and Jérome, 1976). The T_{CDW} was observed to drop sharply with increasing P and the CDW order disappeared at 5 GPa (Moliniè, Jérome, and Grant, 1974; Berthier, Molinie, and Jérome, 1976; Feng *et al.*, 2012). Meanwhile, the T_c increased to a maximum around 10 GPa and then decreased slightly (Suderow *et al.*, 2005). The critical P around 5 GPa was later suggested to be a QCP from high-P XRD measurements at low T (Feng *et al.*, 2012). These studies reveal the peculiar interplay between the CDW order, Fermi surface complexity, and superconductivity. Recently, the P and T dependences of the phonon dispersion of $2H$-$NbSe_2$ were measured by inelastic x-ray scattering (Leroux *et al.*, 2015). A strong T-dependent soft phonon mode, reminiscent of the CDW, was found to persist up to P as high as 16 GPa, far above the critical P at which the CDW disappears at the absolute zero T. Theoretical calculations indicated that the rapid destruction of the CDW under P is related to the zero mode vibrations (or quantum fluctuations) of the lattice renormalized by the anharmonic part of the lattice potential. The calculations also showed that the low-energy longitudinal acoustic mode that drives the CDW transition barely contributes to superconductivity, explaining the insensitivity of the T_c to the CDW transition.

NbS_2 is the only member of the $2H$-MX_2 family that does not undergo a CDW transition. $2H$-NbS_2 is a related two-band superconductor but has a comparable T_c with $2H$-$NbSe_2$. Early resistivity measurements (Moliniè, Jérome, and Grant, 1974) showed that its T_c is independent of P. Recent magnetic susceptibility measurements (Tissen *et al.*, 2013) yielded the P dependence of the T_c and H_{c2} up to 20 GPa. The T_c was found to smoothly increase from 6 K at ambient P to about 8.9 K at 20 GPa. This range of increase is comparable to that found in $2H$-$NbSe_2$. At low P, $H_{c2}(0)$ decreases, and at higher P both the T_c and $H_{c2}(0)$ increase simultaneously, which indicates that the Fermi surface topology accounts for the T_c enhancement in this material.

$2H$-MoS_2 is currently under intensive investigation as an alternative and/or complement to graphene for optoelectronic and electronic applications. It is superconducting upon intercalation with a foreign species such as organic molecules and alkali-metal atoms (Somoano and Rembaum, 1971), electrostatic doping (Ye *et al.*, 2012), or the application of P. Raman spectra and XRD patterns (Chi *et al.*, 2014) provide evidence of an isostructural phase transition from $2H_c$ to $2H_a$ modification at 20 GPa through layer sliding. This first-order transition, which completed around 40 GPa, is characterized by a collapse in the c lattice parameter and volume and also by changes in the interlayer bonding. After the completed phase transition, MoS_2 becomes metallic (Nayak *et al.*, 2014). P has proven to be powerful in driving the TMD to change from a semiconductor to a metal and eventually to a superconductor.

D. Cuprate superconductors

Cuprate superconductors are among the most fascinating and complex quantum systems. The P dependence of T_c of cuprate superconductors is of fundamental interest for elucidating the microscopic mechanism of the superconducting state, as well as for finding new materials with a higher T_c. The initial study of $La_{2-x}Ba_xCuO_4$ under P triggered the discovery of the first compound with a T_c higher than liquid nitrogen T, $YBa_2Cu_3O_7$, proving that investigations under P can provide knowledge for searching for new materials with a higher T_c.

In order to get insight into the basic mechanism responsible for high-T_c superconductivity, one always strives to observe the possible change of T_c at a fixed doping level. P is an effective way to change T_c. However, the effect of P on the T_c is very complex (Schilling, 2006). The P derivative of T_c and dT_c/dP can vary from positive to negative and strongly depends on the doping level. For most optimally doped compounds, T_c generally increases at the initial application of P, passes through a saturation point at some critical P, and then decreases gradually at higher P. An exception is $Tl_2Ba_2CuO_{6+\delta}$, which has negative dT_c/dP from the optimal to the overdoped regime (Schilling, 2006). $Bi_2Sr_2CaCu_2O_{8+\delta}$ is the only known system where the positive dT_c/dP is insensitive to the oxygen content (Sieburger, Müller, and Schilling, 1991), which makes it an ideal system to investigate the phase diagram between the saturated T_c and critical P over the full doping regime (Chen *et al.*, 2004). As shown in Fig. 36, left, the critical P decreases with doping in $Bi_2Sr_2CaCu_2O_{8+\delta}$.

The physical properties of the cuprates are influenced by the interactions between competing or coexisting phases.

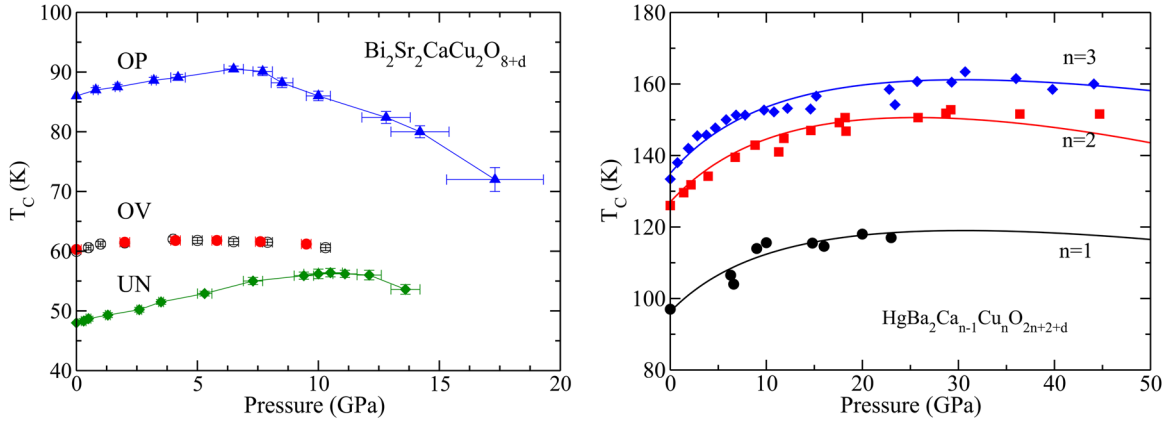

FIG. 36. (Left) The T_c P dependence of $Bi_2Sr_2CaCu_2O_{8+\delta}$ in the underdoped (UN), nearly optimally doped (OP), and overdoped (OV) levels. From Chen *et al.*, 2004. (Right) The T_c P dependence of the optimally doped $HgBa_2Ca_{n-1}Cu_nO_{2n+2+\delta}$. From Chen *et al.*, 2007. The symbols are taken from the experiments of Gao *et al.* (1994b).

Applying P generally increases the concentration of the charge carriers, which has led to the suggestion that a cuprate will eventually behave as a Fermi liquid after passing the optimal doping level. The record high T_c of 164 K was achieved in $HgBa_2Ca_2Cu_3O_{8+\delta}$ (Hg1223) (Gao *et al.*, 1994b) at a P around 30 GPa. Recent experiments have added complexity to the understanding of the P effect (Muramatsu, Pham, and Chu, 2011). Applying P causes superconductivity to vanish in some systems and even drove the material toward an insulating state in $YBa_2Cu_3O_{7-\delta}$ (Y123). This destruction of superconductivity by P was also observed in a model system $HgBa_2CuO_{4+\delta}$ (Hg1201). Single-crystal XRD measurements provided evidence for the existence of oxygen ordering, which indicates that P-induced oxygen ordering suppresses superconductivity in cuprates. The measurements of the superconducting and structural properties on an underdoped Hg1201 revealed almost the same increase in the T_c with P compared to the optimally doped compound (Wang *et al.*, 2014). The copper and oxygen bond distances alone were inadequate for explaining the large difference in T_c between the optimally doped Hg1201 and $La_{2-x}Sr_xCuO_4$. These results suggest that an interaction involving the charge reservoir layers is likely to be involved.

In a limited class of cuprate, nanoscale inhomogeneity of the spin and charge densities in the form of stripes, originating from competing electronic interactions, results in a sharp dip of the T_c at 1/8 doping in the phase diagram. Taking advantage of the high-P technique, a direct observation of the charge and spin order under P in stripe-ordered $La_{1.85}Ba_{0.125}CuO_4$ single crystals indicated that both the charge order and spin order still exist in the high-T tetragonal (HTT) phase after the long-range low-T tetragonal (LTT) phase was suppressed by P (Hücker *et al.*, 2010). X-ray absorption fine structure analysis shows that instantaneous local correlations of the characteristic octahedral tilt pattern remain robust far beyond the P of macroscopic LTT-HTT transition (Guguchia *et al.*, 2013). Across the macroscopic LTT-HTT transition, the smooth decrease of the charge-ordered T is consistent with a gradual rise in the superconducting T_c, suggesting that charge and spin orders are strongly coupled to the local octahedral distortion rather than the long-range disorder and are consistent with a short-range nematic electronic liquid-crystal state.

The interplay of superconductivity and disorder has been discussed for several decades, but a comprehensive understanding of their interactions remains unavailable. Much effort has been devoted to understanding the interplay in cuprates by adding a degree of disorder. Calamiotou *et al.* (2009) emphasized the disorder effects on superconductivity under P in two superconductors $YBa_2Cu_4O_8$ (Y124) and Y123 and nonsuperconducting $PrBa_2Cu_3O_{6.92}$ by combining synchrotron XRD and Raman spectroscopy measurements. Their analysis showed a clear anomaly in the evolutions of both the lattice parameters and phonon modes with P in these systems. The disorder increases with P when the anomaly appeared. The observed phase separation is analogous to the one previously reported by Calamiotou *et al.* in these systems at ambient P. Recently Nakayama *et al.* (2014) investigated the crystal structure and electrical resistivity of Y124 under P up to 18 GPa. A dramatic change of T_c was observed and accompanied by a structural phase transition around 10 GPa. This study was followed by Raman spectroscopy and *ab initio* calculations, which confirmed the phase transition. Recently P-induced disorder enhancement was also observed in a nearly optimally doped $Tl_2Ba_2CaCu_2O_{8+\delta}$ (Zhang *et al.*, 2015). The disorder competed with superconductivity.

The generic behavior that T_c varies with P following a paraboliclike curve in many cuprates can be understood by many two-component models, including charge carrier concentration and another intrinsic variable. For the charge-transfer model (Almasan *et al.*, 1992), the maximum T_c is considered as the other intrinsic variable besides carrier concentration. This simple model works very well for many cuprates with different dopants (Chen and Jiao, 1997). The models based on BCS-like gap equations can also be used to reproduce the T_c variation with P for many compounds. Later developments for identifying the pairing interaction strength as the second intrinsic variable have led to many explanations for the T_c evolution with P and its P derivatives for compounds with different dopants (Chen, Lin, and Gong, 2000; Chen *et al.*, 2004), the uniaxial P effect on T_c, the

rare-earth ionic size effect on T_c (Chen and Su, 2005), and even the strain effect on T_c. This variable has been confirmed by high-P NMR studies (Maisuradze *et al.*, 2011).

Lattice vibrations and excitations of electronic origin such as spin or electric polarizability fluctuations are believed to be two potential candidates of Cooper pairing in the cuprate superconductors. Both have important contributions to the pairing interaction strengths (Chen *et al.*, 2007). The consideration of pairing interaction strength and carrier concentration may be sufficient for explaining the observed T_c behavior in cuprates at high P even within the framework of phonon-mediated pairing (Chen *et al.*, 2007). Figure 36, right, presents the results of the comparison of both measurements (Gao *et al.*, 1994b) and phenomenological calculations (Chen *et al.*, 2007) for the optimally doped $HgBa_2Ca_{n-1}Cu_nO_{2n+2+\delta}$ ($n = 1$, 2, and 3). Similar components from the dynamic inhomogeneity-induced pairing model have also been used to explain the experiments (Chen *et al.*, 2010). This model includes the pairing scale and the phase ordering scale. The former characterizes pair formation and is proportional to the energy gap. The latter controls the stiffness of the system to phase fluctuations and is determined by the superfluid density. In fact, the superfluid density is approximately proportional to the carrier concentration before the optimal level, and the pairing interaction strength should be scaled by the energy gap. Therefore, the carrier concentration and the pairing interaction strength are two intrinsic P variables for understanding the P effect on the T_c in cuprate superconductors.

E. Iron pnictides and chalcogenides

The discovery of superconductivity in iron pnictides and chalcogenides has attracted great interest because of their high T_c's and their resemblance to cuprates. Applying P to iron-based compounds has brought about many rich discoveries including the introduction of superconductivity in the parent 122 compounds $BaFe_2As_2$, $SrFe_2As_2$, $CaFe_2As_2$, and $EuFe_2As_2$, the significant enhancement of the T_c above 40 K in $LaO_{1-x}F_xFeAs$ (1111) (Takahashi *et al.*, 2008), a record of 9.1 K/GPa P derivative of T_c in FeSe (11) (Medvedev *et al.*, 2009); the reemergence of the second superconducting dome with the disappearance of the first in heavily electron-doped $(K_{0.8}, Tl_{0.6}Rb_{0.4})Fe_{2-y}Se_2$ (122*) (Sun *et al.*, 2012); and the V-shaped T_c path in AFe_2As_2 (A = K, Rb, Cs) (Tafti *et al.*, 2013) or T_c oscillation (Taufour *et al.*, 2014) accompanied by T_c enhancement (Nakajima *et al.*, 2015) in KFe_2As_2 at higher P. The phase diagram and structure evolution with P were found to be similar to doping (Kimber *et al.*, 2009).

An early review of high-P studies on Fe-pnictide superconductors was given by Chu and Lorenz (2009), who mainly discussed the P effects on the magnetic and superconducting transitions of three families of doped and undoped 1111, 122, and (Li,Na)FeAs (111) compounds. The P effects on the superconducting and structural properties were later reviewed for pnictides by Stewart (2011) and the 122* family by Dagotto (2013). A specific review of 1111 and 122 was also conducted (Sefat, 2011). Here we focus on the new developments in the 122 and 11 families.

Among all iron pnictides, the $BaFe_2As_2$ system has been extensively studied because of the availability of high-purity single-crystal samples. This system shares a common phase diagram with other iron arsenides. For example, the undoped parent compound $BaFe_2As_2$ is magnetically ordered in a SDW state. With cooling, this material undergoes both structural and magnetic transitions at about 140 K (Huang *et al.*, 2008). At ambient P, superconductivity emerges upon doping by electrons, holes (Rotter, Tegel, and Johrendt, 2008), or even isovalent elements (Dhaka *et al.*, 2011) when the SDW instability is suppressed. The maximum T_c is achieved close to the optimal concentration where the SDW state is completely suppressed. As a clean tuning parameter of structural and physical properties without introducing disorder, the role of P in inducing superconductivity was highlighted in the 122 family. All the 122 parent compounds can become superconductors with the application of P. Detailed studies on the structural and magnetic properties of $BaFe_2As_2$ at high P (Wu *et al.*, 2013) indicate that subtle changes or contractions of the structure can switch on superconductivity from the neighboring AF ground state. Neutron diffraction measurements (Kimber *et al.*, 2009) on the parent compound $BaFe_2As_2$ revealed many similarities between the structural distortions under P and chemical doping. Quantum oscillation measurements (Graf *et al.*, 2012) reported that the quasiparticle effective masses m^* in this parent increase with increasing P, directly indicating the importance of enhanced electronic correction for superconductivity.

Measurements of the de Haas–van Alphen effect (Shishido *et al.*, 2010) on $BaFe_2(As_{1-x}P_x)_2$ revealed a strong reduction in m^* as the doping level moved from the optimal to the overdoped side. A comparison study of the doping and P effects on the 122 compounds suggested that the mechanism for driving superconductivity only becomes common in both cases if the system in the overdoped regime has an increased itinerancy that is responsible for T_c reduction. This explanation is also appropriate for other iron pnictides in the overdoped regime.

A close relationship between the axial ratio c/a and superconductivity has been found in the parent 122 compounds. The three-dimensional feature of their structure favors superconductivity under P. At higher P, the 122 iron-based superconductors often undertake an isostructural transformation from a tetragonal to a collapsed tetragonal cT phase at a critical P, where superconductivity disappears. This collapse was suggested to be the onset of the $4p_z$ interlayer bond formation. The suppression of the AF spin fluctuations in the cT phase was observed from high-P inelastic neutron-scattering measurements on $CaFe_2As_2$ (Pratt *et al.*, 2009). The absence of superconductivity in this cT phase was found to result from the suppression or absence of both a static AF order and dynamic spin fluctuations.

Iron selenide FeSe, the simplest Fe-based superconductor for studying the pairing mechanism, possesses many attractive features (Maiti *et al.*, 2011). Compression to 9 GPa leads to a strong enhancement of the T_c up to 37 K (Medvedev *et al.*, 2009). The same origin was found for both the nematicity and superconductivity (Wang *et al.*, 2016). The nematicity effect means that electron orbitals break lattice symmetries and align similar to a series of rods. The largest superconducting gap was obtained and closed above 65 K in strained FeSe epitaxial

thin films (He *et al.*, 2013). Additionally, transport measurements showed that the single-layer film of FeSe has a high T_c of 109 K (Ge *et al.*, 2015).

Structural studies on FeSe at different P-T delivered different phase diagrams. Except the initial tetragonal P_4/nmm and hexagonal $P6_3/mmc$ at ambient conditions (Hsu *et al.*, 2008), different measurements gave different structures for the low-T orthorhombic phases at ambient P, as well as the high-P phases (Medvedev *et al.*, 2009). It is hard to correlate the T_c with the structural parameters. In a study using a hydrostatic argon transmitting medium, no traces of superconductivity above 12 GPa were observed from ac susceptibility measurements (Braithwaite *et al.*, 2009). An experiment using a precise evaluation of the T_c from zero-resistivity temperatures (Okabe *et al.*, 2010) also revealed the destruction of superconductivity above 12 GPa. Moreover, a striking correlation between the T_c and the anion Se height relative to the Fe layer was found if the zero-resistivity T_c was chosen (Fig. 37). Such a relationship is broadly applicable to iron pnictides, strongly indicating that the highest T_c can be obtained around the optimum anion height in iron-based superconductors.

F. Organic superconductors

Superconductivity in organic molecules is based on electron interactions with electron excitations. The energy of these excitations in organic molecules is much higher than the phonon energy and can result in a substantially higher T_c. Organic superconductors are generally charge-transfer compounds that include electron donor molecules such as tetrathiafulvalene (TTF), bis-ethylenedithrio-TTF (BEDT-TTF, abbreviated as ET), and tetramethyltetraselenafulvalene (TMTSF) derivatives, as well as electron acceptor molecules such as tetracyanoquinodimethane or fullerides. The role of P in inducing and enhancing superconductivity in organic compounds is noteworthy. The first organic superconductor $(TMTSF)_2PF_6$ (Jérome *et al.*, 1980) was discovered through the use of P where the highest T_c of 14.2 K among the charge-transfer salts was also observed in β'-$(BEDT\text{-}TTF)_2ICl_2$ at a P of 8.5 GPa (Fig. 38) (Taniguchi *et al.*, 2003; Kano *et al.*, 2009). Early experiments on fullerides showed that the lattice contraction is not in favor of T_c enhancement (Sparn *et al.*, 1991). This offers a clue for enhancing the T_c through the lattice expansion.

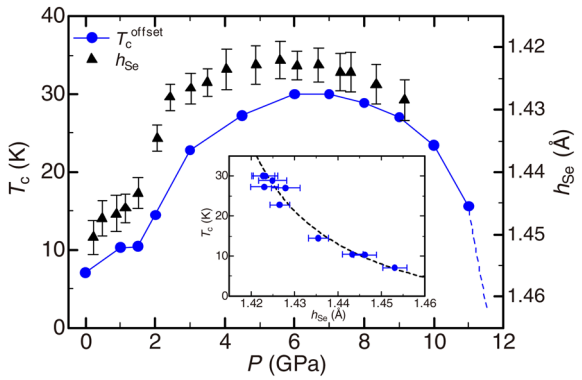

FIG. 37. P dependence of T_c and Se height h_{Se} of FeSe. The inset shows the T_c as a function of the Se height. The dotted line is a guide to the eye. From Okabe *et al.*, 2010.

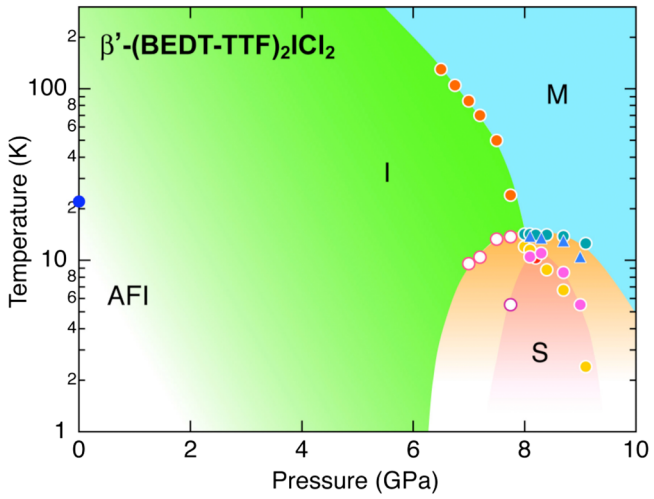

FIG. 38. P-driven phase evolution from the parent AF insulator (AFI) to a superconducting phase (S) with a metallic (M) normal state in β'-$(BEDT\text{-}TTF)_2ICl_2$. From Kano *et al.*, 2009.

Organic salts are very sensitive to applied P. In most cases superconductivity can be readily suppressed with the application of P (Sparn *et al.*, 1991) and an insulating state can even be reached at higher P (Hagel *et al.*, 2003). This is observed within fullerides, where applying P often reduces the T_c in ambient-P fulleride superconductors. Superconductivity at the record high T_c of 40 K in Cs_3C_{60} was reported when the material was compressed to 1.43 GPa (Palstra *et al.*, 1995). This was confirmed by bulk superconductivity with a T_c of 38 K in Cs_3C_{60} (Ganin *et al.*, 2008). Detailed analysis of the structural and magnetic properties revealed that the superconductivity was induced in the compound after the AF ordering of the insulating state was suppressed (Takabayashi *et al.*, 2009). The emergence of superconductivity under P highlights the role of the electron correlations in the charge-transfer salts as an important mechanism for superconductivity. Even for an electronic mechanism, the change of electronic structure by zero-point vibrations can account for an observable isotope effect (Ashcroft and Cyrot, 1993). The P effect on K_3 picene (18 K phase) is remarkable where its T_c increases linearly with P up to 1.2 GPa with $dT_c/dP = 12.5$ K/GPa (Kambe *et al.*, 2012). P also drove the single-component molecule [Ni(hfdt)2] [hfdt = bis(trifluoromethyl) tetrathiafulvalenedithiolate] to become a new superconductor after the initial insulating phase was suppressed (Cui *et al.*, 2014).

Studies of organic superconductors based on donor molecules such as BEDT-TTF or TTF derivatives and acceptor molecules such as fullerides have established that the electronic correlation parameter U/W is a unique parameter for controlling their phases and scaling T_c (Duband *et al.*, 2003). This parameter reflects the competition between the on-site interelectron repulsion U (favoring localization of the electrons) and the bandwidth W proportional to the electron transfer integral t (favoring delocalization). For fullerides (Takabayashi *et al.*, 2009), a relatively high T_c was observed in the proximity of the electron localization following a

parabolic T_c behavior achieved by decreasing the U/W through the substitution of metal ions with smaller ionic radii or by applying P. This process is also shared by the BEDT-TTF salts, in which the ratio t'/t of the next nearest neighboring integral t' to the nearest neighboring integral t is proposed to work together with the U/W to account for the superconductivity in such anisotropic organic systems (Shimizu, Maesato, and Saito, 2011).

In well-studied θ-type BEDT-TTF complexes, a unified phase diagram can be characterized by the dihedral angle between the donor columns (θ) (Mori, Tanaka, and Mori, 1998). Because U is the characteristic value of the electron donor molecule and is the same in the θ-type BEDT-TTF salts, it can be stated that U/W varies mainly due to the change of the transfer integral t or the dihedral angle θ. A reduction of θ through chemical P or external P leads to a significant increase of t and results in a decrease in U/W that drives the system from insulating or superconducting to a metallic state. Magnetic measurements on cation-doped phenanthrene (X. F. Wang *et al.*, 2011) revealed the existence of local spin moments and thereby indicated a similar interplay between magnetism and superconductivity observed in fullerides (Takabayashi *et al.*, 2009). The mechanism of superconductivity in aromatic hydrocarbons has not been solved. Although theoretical studies have attempted to investigate the electron-phonon interactions as the possible nature of superconductivity, the electron correlations in these systems are non-negligible. The P effect on superconductivity in these compounds can be well understood within the strongly correlated electron framework. The structural and vibrational information at high P is helpful for understanding the role of the controlling parameters of superconductivity in these compounds.

Recently p-terphenyl ($C_{18}H_{14}$), a hydrocarbon compound containing three benzene rings connected by C-C bonding, draws a lot of attention due to the discovery of high-temperature superconductivity (Wang *et al.*, 2017). This compound is a nonpolycyclic aromatic hydrocarbon. Different from the feature of sharing an armchair edge in polycyclic aromatic hydrocarbons such as phenanthrene, chrysene, picene, coronene, and 1,2;8,9-dibenzopentacene, benzene rings in p-terphenyl are connected by the single C-C bond. Wang *et al.* (2017) showed the superconductivity of 7.2, 43, and even 123 K in potassium-doped p-terphenyl. Bipolaronic bands were suggested to account for the observed superconductivity. By using high-resolution photoemission spectroscopy on potassium surface-doped p-terphenyl crystals, Li *et al.* (2017) presented the spectroscopic evidence for pairing gaps at the surfaces of these materials, with the gaps persisting to 60 K or above, which greatly promotes the study of superconductivity of p-terphenyl.

G. Heavy-fermion superconductors

Heavy-fermion systems are intermetallic compounds, containing lanthanide or actinide elements with partially filled $4f$ or $5f$ orbitals. The f electrons hybridize with the normal conduction electrons leading to quasiparticles with an enhanced mass. These systems can be modeled as a lattice of localized f-electron moments that are coupled to a band of conduction electrons (the Kondo effect). An indirect intersite interaction exists between the local moments as well, which competes with the Kondo effect, causing a variety of ground states.

One of the most attractive and elusive phenomena of heavy fermions is their superconductivity. The discovery of the first heavy-fermion superconductor $CeCu_2Si_2$ by Steglich *et al.* (1979) was a surprise. At that time, even a small amount of magnetic impurities were known to conflict with superconductivity in all known superconductors. Superconductivity in heavy fermions was highly scrutinized at the beginning and was accepted only after the discovery of superconductivity in UBe_{13} and UPt_3. After that, a few U-based and Ce-based heavy-fermion superconductors were discovered. Unlike the conventional superconductors, the phonon-mediated pairing does not work for the superconductivity in these heavy-fermion superconductors. Magnetic interactions are believed to be relevant for describing the superconducting and normal-state properties of other strongly correlated electronic systems. Unlike other known heavy-fermion superconductors based on Ce or U, $PrOs_4Sb_{12}$ is the first superconductor based on Pr with a T_c of 1.85 K (Bauer *et al.*, 2002).

Application of P provides a powerful means for exploring unconventional superconductivity, mostly on the border of magnetism in the heavy-fermion systems. P plays an important role in tuning the normal-state and superconducting properties of these compounds. The discovery of superconductivity in $CeCu_2Ge_2$ with the application of P has drawn attention from the condensed-matter community (Jaccard, Behnia, and Sierro, 1992). Since then, high-P studies on Ce-based heavy fermions have brought about a number of new superconductors such as $CePd_2Si_2$ (Julian *et al.*, 1998), $CeIn_3$ (Mathur *et al.*, 1998), $CeRhIn_5$ (Hegger *et al.*, 2000), $CePt_2In_7$ (Bauer *et al.*, 2010), and $CeAuSi_2$ (Ren *et al.*, 2014). $CeCu_2Ge_2$ is an isostructural sister compound of $CeCu_2Si_2$. Both share the same phase diagram when pressurized above 10 GPa, exhibiting a second superconducting phase with a higher T_c. Moreover, partial substitution of Si by Ge in $CeCu_2Si_2$ results in two distinct superconducting domes due to disorder-induced pair breaking (Yuan *et al.*, 2003). Magnetic fluctuations and valence fluctuations are proposed to mediate the electron pairing separately for each dome, while critical fluctuations stemming from an orbital transition also provide interpretation for the superconducting pairing (Willers *et al.*, 2015). Recent observations of the enhanced magnetism and superconductivity with increasing P in $CeAu_2Si_2$ over a broad P phase (Ren *et al.*, 2014) not only provide a unique example of the interplay between superconductivity and magnetism, but also underline the role of orbital physics in understanding the Ce-based heavy-fermion systems.

Quantum phase transitions are the key to understanding the interplay of superconductivity and magnetism in heavy-fermion systems. Quantum criticality is mostly obvious in Ce-based compounds but less so in U-based heavy-fermion superconductors, even though they appear near magnetism. Superconductivity in a few Ce-based compounds appears at a certain range near the critical P where the AF state disappears abruptly. In many other heavy-fermion systems, the AF order is suppressed continuously by P and superconductivity

develops near QCP. Other types of phase transitions may exist in the vicinity of superconductivity. UGe_2, URhGe, and UCoGe show superconductivity within a regime of FM ordering. In some U-based compounds such as URu_2Si_2, UPd_2Al_3, and UNi_2Al_3, the magnetic order coexists with superconductivity at a microscopic scale without a strong interaction with each other.

Stacking layers of $CeIn_3$ and $RhIn_2$ bring about superconductivity in the compressed AF $CeRhIn_5$ (Hegger *et al.*, 2000) with a tenfold increase of the maximum T_c compared to $CeIn_3$. At ambient P, $CeRhIn_5$, AF orders at 3.8 K, and the AF state vanishes at a critical P of 1.8 GPa when T_N equals T_c at 1.9 K. Upon further compression, T_N falls below the T_c and terminates at a quantum critical point at 2.3 GPa. The local nature of quantum criticality implies simultaneous fluctuations in the spin and charge channels. The de Haas–van Alphen technique is a well-established means to probe the Fermi surface. When this technique was used for $CeRhIn_5$ in the magnetic fields between 10 and 17 T, a pronounced jump in the Fermi surface was observed at a critical P of 2.3 GPa (Shishido *et al.*, 2005). The breakdown of the Kondo effect may be the source of the anomalous properties of the heavy-fermion compounds at low T. The breakdown of the Kondo effect is usually considered to be a consequence of the system's proximity to the QCP. The present experiment provides consistent evidence for a Kondo-breakdown QCP.

For the related compound $CeCoIn_5$, the lack of signatures for quantum critical behavior in Cd-doped $CeCoIn_5$ manifests a new mechanism for the coexistence of magnetism and superconductivity (Seo *et al.*, 2014). This also provides a different perspective for interpreting the response to disorder in other strongly correlated superconductors near a zero-T magnetic instability.

Replacing Ce ($4f$) with Pu ($5f$) while keeping the $CeCoIn_5$ structure increases the T_c from 2.3 to 18.5 K in $PuCoGa_5$ (Sarrao *et al.*, 2002), a T_c record holder among heavy-fermion superconductors.

XI. PERSPECTIVES: SYNERGETIC ADVANCES IN MULTIPLE TECHNOLOGIES, DISCIPLINES, AND DIMENSIONS

As a fundamental physical variable, high P alters all states of matter. Major advancement in high-P physics and technology undoubtedly has far-reaching impacts in all sciences of matter. Conversely, the multidisciplinary advancement in high-P chemistry, geoscience, astrophysics, and materials applications provides rich feedback for fundamental physics. The overall progress in the P dimension will rely greatly on synergetic advances.

A. High-*P* research and the next-generation x-ray facilities

To a great extent, the advancement of high-P physics is dictated by the capabilities of reaching extreme conditions and probing exotic properties. A number of emerging technological advancements are expected to have a major impact on high-P physics. The plethora of successful developments in high-P experimentation at synchrotron facilities has exemplified the symbiotic relationship between high-P science and penetrating x-ray probes (Shen and Mao, 2017). High-P x-ray emission spectroscopy provides information on the filled electronic states of the compressed samples (Rueff *et al.*, 1999; Badro *et al.*, 2003). High-P x-ray Raman spectroscopy probes the chemical bonding changes in the light elements (Lee, Eng, and Mao, 2014) and the electronic features of strongly correlated materials (Ding *et al.*, 2014) under compression. High-P electronic inelastic x-ray scattering spectroscopy (Rueff and Shukla, 2010) accesses the high-energy electronic phenomena, including electronic band structure, Fermi surface, excitons (H. K. Mao *et al.*, 2010), plasmons (Mao *et al.*, 2011), and their dispersions. High-P resonant inelastic x-ray scattering spectroscopy probes shallow core excitations, multiplet structures, and spin-resolved electronic structure (Ding *et al.*, 2012). High-P nuclear resonant x-ray spectroscopy provides phonon densities of state and time-resolved Mössbauer information (Shahar *et al.*, 2016). High-P x-ray diffraction determines the fundamental structures and densities of polycrystalline, single-crystal (Finkelstein *et al.*, 2014), multigrain (L. Zhang *et al.*, 2013), nanocrystalline (Yang *et al.*, 2013), and noncrystalline materials (Zeng *et al.*, 2011). High-P radial x-ray diffraction yields deviatoric elastic and rheological information (Gleason and Mao, 2013). High-P transmission x-ray tomography reveals three-dimensional texture information and changes of size, shape, and composition under various stress conditions (Jiang *et al.*, 2013; Shi *et al.*, 2013). Together these synchrotron-based techniques form a systematic network to enable high-P investigations of essential physical phenomena.

Large x-ray facilities are currently going through a major generation change in two directions, namely, the ultimate synchrotron source and x-ray free-electron laser (XFEL). The ultimate synchrotron source is to optimize all design parameters of the third-generation synchrotron sources, which may lead to improvements by several orders of magnitude in the superiority of x-ray beam characteristics, such as high brilliance, low emittance, short pulse, and high coherence. These improvements are highly desirable for high-P applications and will certainly lead to a great leap forward by extending most of the aforementioned high-P synchrotron techniques. Although XFEL is sometimes referred to as the fourth-generation source, it increases these x-ray characteristics by another 3–6 orders of magnitude at the expense of a lower repetition rate and will differ from the synchrotron in its concept and applications. Nevertheless, it provides great potential for revolutionary high-P applications, particularly in temporal resolutions. Major impacts are emerging in the high-P research areas of (1) mass transport under high P-T: elemental diffusion, viscosity, high strain rate, dynamic response; (2) transient phenomena: phase transition kinetic and mechanism, intermediate states, unstable sample conditions; (3) optical pump-probe investigations of materials' properties at extreme P-T (Gleason *et al.*, 2015); and (4) the extended P-T ranges beyond static conditions.

B. High-*P* and nanodimensions

The emergence of nanoresearch in the past two decades has proven to be highly complementary to high-P research at both technical and scientific levels. Since ultrahigh P is reached

with microscopic samples, the advantage of consorted advances of high-P and nanotechnology will continue to rise. The nanoengineering and maneuvering capabilities of the P chamber, samples, and physical probes are essential when the typical anvil size of μm advances to sub-μm. Nanomachining technology, such as the focused ion beam, has now been used for pioneering fabrication of DAC samples (Pigott, Reaman, and Panero, 2011), anvils (Sakai *et al.*, 2015), and gaskets (Orloff, Narayana, and Ruoff, 2000) to nm precision. Nanocircuits have been integrated for transport and other electromagnetic measurements. Synchrotron probes have been developed for nanoscale x-ray diffraction, absorption, and imaging for structural, elastic, plastic, and compositional studies under P. An ingenious transmission electron microscopy (TEM) method has successfully generated up to 40 GPa using a carbon nanotube as a P vessel for *in situ* TEM studies of samples encapsulated in the nanotube (Wu and Buseck, 2013).

From a scientific aspect, both the P and nanoscale are physical dimensions that control materials' behaviors. They multiply each other and generate new interesting physics of nanomaterials at high P. For instance, the size limit of dislocation in nanonickel particles was previously thought to be 30 nm below where dislocation could not form, and plastic deformation required other mechanisms. However, high-P experiments observed significant texturing in 3 nm nickel when it was compressed above 18.5 GPa and confirmed that under high external P dislocation activities could be extended down to a few-nanometer length scale (Chen *et al.*, 2012). Hence, our understanding of the nanodislocation mechanism was fundamentally altered. The application of P onto nanoparticles also creates novel materials. For instance, new superhard carbon allotropes that can indent diamond were discovered when solvated C_{60} buckyballs were subjected to high compression. Individual buckyballs were crushed into disordered clusters, while the clusters were still arranged in an ordered crystal structure. The material could be recovered after releasing P (Wang *et al.*, 2012). This discovery creates a new category of material with a long-range ordered structure formed by clusters of short-range disordered carbon atoms. The interaction of the two major dimensions, the P and the nanoscale, is expected to have numerous impacts on physics.

C. High-P chemistry

Stoichiometries among various elements are one of the most fundamental rules governing chemistry and materials syntheses. The rule can be overcome or drastically altered by extreme P. New materials with unconventional stoichiometries emerge at high P even for very common compounds. Two novel high-P compounds $Xe(H_2)_7$ above 4.8 GPa and $Xe(H_2)_8$ above 7.1 GPa contain the highest hydrogen content of all known compounds (Somayazulu *et al.*, 2010). A unique hydrogen-rich structure forms that can be viewed as a triple solid hydrogen lattice modulated by layers of Xe, consisting of Xe dimers. Varying P tunes the Xe-Xe distances over a broad range from that of an expanded Xe lattice to the distances observed in metallic xenon at megabar P. This discovery provides an insight into extremely hydrogen-rich compounds.

$BaReH_9$ is one of the most hydrogen-rich ionic salts known. Theoretical calculations (Markopoulos, Kroll, and Hoffmann, 2010) found that the NiAs-type structure of $BaReH_9$ exhibits remarkably short intermolecular $H\cdots H$ contacts, which lead to a new structure with discrete H_2 units between ReH_7^{2-} motifs. This structural change is associated with a dramatic lowering of the metallization P, so that $BaReH_9$ is expected to become metallic at the onset of the H_2-containing phase at 51 GPa. Li *et al.* (2011) discovered a new rhodium dihydride (RhH_2) with a very high volumetric hydrogen density. Compressed in fluid hydrogen at ambient temperature, the fcc rhodium metal absorbs hydrogen to form a NaCl-type, fcc rhodium monohydride at 4 GPa and a fluorite-type, fcc RhH_2 at 8 GPa. Low-temperature experiments show that RhH_2 is recoverable after releasing P cryogenically to 1 bar and is capable of retaining hydrogen at 77 K indefinitely.

Even the common salt NaCl can be changed to cubic and orthorhombic $NaCl_3$ and two-dimensional metallic tetragonal Na_3Cl at high P (W. Zhang *et al.*, 2013). These experiments establish that compounds violating chemical intuition can be thermodynamically stable even in simple systems.

D. Studies of Earth's and planetary deep interiors

In order to study the Earth's interior one must understand its constituents—ordinary minerals whose physical and chemical properties have been drastically changed by the extremely high-P conditions that prevail at great depths. Driven by the clearly defined mineral physics goals, laser-heated DAC techniques have been developed to reach the Earth's center P-T conditions of 362 GPa–6000 K and obtain the *in situ* structural, elastic, rheological, chemical, and electronic properties of relevant oxides, sulfides, silicates, hydrous minerals, metals, and alloys. The melting curve of iron at the P-T conditions of the molten outer core has been determined (Tateno *et al.*, 2010). Radial XRD methods have been invented for the determination of elasticity tensors, lattice preferred orientation, and the strength of iron to the Earth's core P. The nuclear resonant inelastic x-ray scattering method has been developed for the determination of the phonon density of states of iron and ferromagnesian postperovskite at high P for comparison with the observed seismic velocities at the D″ layer (Mao *et al.*, 2006) and the core. High-P XES is a diagnostic tool that has been established for discovering the long sought-after P-induced, iron spin-pairing transitions (Badro *et al.*, 2003) that govern element differentiation, elasticity, and radiative heat transfer in the deep mantle. These studies have applied fundamental condensed-matter physics and designed key high P-T experiments to garner crucial new information for constraining the static and dynamic models of the Earth's deep interior. In turn, these new techniques also open new areas of research in high-P physics.

A number of advancements during the past years have demonstrated that this successful synergy will definitely expand in the foreseeable future. Ohta *et al.* (2016) experimentally determined the electrical conductivity of iron to 4500 K at 100 GPa in a DAC and derived a high thermal

conductivity of the iron core that suggested rapid core cooling and a young inner core less than 700×10^6 years old. On the contrary, Konôpková *et al.* (2016) directly measured the thermal conductivity in solid iron at planetary core conditions using a flash laser-heating technique in a DAC and concluded a low thermal conductivity for the core, indicating that the Earth's magnetic field and the solid inner core are old and have persisted since the beginning of Earth's history. Shahar *et al.* (2016) instead used NRIXS to probe various iron compounds to determine the P effects on iron isotope fractionation and to derive the composition of the outer core. Using first-principles calculation and DAC high P-T experiments, Hu *et al.* (2016) discovered a highly stable, pyrite-structured iron oxide (FeO_2) at 76 GPa and 1800 K that holds an excessive amount of oxygen. They demonstrated the likely accumulation of a large quantity of this new compound at the core-mantle boundary. This scenario may explain the seismic anomaly of the ultralow velocity zone and may provide a source for the oxygen that caused the great oxidation event 2×10^9 years ago (Lyons, Reinhard, and Planavsky, 2014).

E. Materials applications

Extreme P-T environments present a vast, unexplored, fertile ground to search for transformative materials and phenomena. High-P physics studies provide a new route toward discovering advanced structural materials and new materials with enhanced performance for energy transformation (i.e., solar, mechanical, chemical to electrical), energy storage (i.e., batteries, capacitors, hydrogen), and energy transmission, sensing, and monitoring. P drastically changes chemical speciation, dissolution, reactivity, combustion, catalysis, absorption, photochemistry, and electrochemistry. P may create dozens of novel phases with very different properties in an average chemical system; many of them may be quenchable and may carry potential applications for energy generation, storage, and transportation. The interest in high-P hydrogen has recently extended well beyond the elemental forms to encompass hydrogen-containing molecular alloys and compounds for hydrogen storage applications.

P is opening up broad new vistas of superconductivity from simple elements to complex organic and inorganic materials and the creation of new electronic and magnetic materials of great significance to energy science. P strongly affects emergent properties as well as ordinary electromagnetic materials, including high-temperature superconductivity, topological insulators, charge- and orbital-density waves, electronic phase separation, magnetocapacitance, multiferroics, spintronics, Mott insulators, heavy fermions, colossal magnetoresistivity, polar energy materials, and quasi-low-dimensional materials, thus addressing problems ranging from efficient charge injection in photovoltaic devices to lossless electrical transmission over superconducting lines. P-tuning plasmons, excitons, and electron dynamics provide fundamental information necessary for the grand challenge of controlling materials' processes at the electron level.

It is important to address the underlying origin of P-induced transitions between crystalline and amorphous materials, and the creation of nanoscaled structures and orders. The dimensionality and size scale of these materials are closely related to their applications in light emission, catalysis, filtering, membranes, etc. and potentially impact energy efficiency, production, utilization, and storage. Applying variable high P, T, and strain rates will be needed to synthesize new structural materials such as diamond (Irifune *et al.*, 2003; Huang *et al.*, 2014), cBN (Tian *et al.*, 2013), and tough lightweight carbon-based materials, and to study their response and resistance under extremely harsh P-T and chemical environments.

To recover the novel high-P materials metastably at ambient P far away from equilibrium is vital for future development. Mounting examples reveal that the combination of high P and low temperatures not only creates matter, but also sustains matter, very far away from the equilibrium. In these studies, P provides a powerful means for continuously tuning the free energy of the system; x-ray photons excite systems into highly metastable states, and low temperature and chemical tuning prevent the system from reaching equilibrium. By varying these parameters, characterizing the dynamically compressed or stressed and electronically excited materials with time-resolved probes, and combining these efforts with first-principles calculations, the transition mechanisms and energy landscapes can be revealed. Such knowledge is essential for the recovery of materials to ambient conditions for use in numerous energy applications.

ACKNOWLEDGEMENTS

We thank Xing Wu for format editing. Comments from Freyja O'Toole and three anonymous reviewers improved the manuscript. We acknowledge the financial support of the U.S. National Science Foundation grants (EAR-1345112 and EAR-1447438) and the Natural Science Foundation of China Grant No. U1530402. The high-P synchrotron technology section was supported by the DOE-BES under Award No. DE-FG02-99ER45775.

REFERENCES

Abd-Elmeguid, M. M., B. Ni, D. I. Khomskii, R. Pocha, D. Johrendt, X. Wang, and K. Syassen, 2004, Phys. Rev. Lett. **93**, 126403.

Abd-Elmeguid, M. M., C. Sauer, U. Köbler, and W. Zinn, 1985, Z. Phys. B **60**, 239–248.

Abd-Elmeguid, M. M., C. Sauer, and W. Zinn, 1985, Phys. Rev. Lett. **55**, 2467–2470.

Adachi, T., H. Tanaka, H. Kobayashi, and T. Miyazaki, 2001, Rev. Sci. Instrum. **72**, 2358–2360.

Ahart, M., M. Somayazulu, S. A. Gramsch, R. Boehler, H. K. Mao, and R. J. Hemley, 2011, J. Chem. Phys. **134**, 124517.

Akahama, Y., and H. Kawamura, 2007, High Press. Res. **27**, 473–482.

Akahama, Y., and H. Kawamura, 2010, J. Phys. Conf. Ser. **215**, 012195.

Akahama, Y., H. Kawamura, and T. L. Bihan, 2001, Phys. Rev. Lett. **87**, 275503.

Allen, J. W., and L. Z. Liu, 1992, Phys. Rev. B **46**, 5047–5054.

Allen, J. W., and R. M. Martin, 1982, Phys. Rev. Lett. **49**, 1106–1110.

Almasan, C. C., S. H. Han, B. W. Lee, L. M. Paulius, M. B. Maple, B. W. Veal, J. W. Downey, A. P. Paulikas, Z. Fisk, and J. E. Schirber, 1992, Phys. Rev. Lett. **69**, 680–683.
Ament, L. J. P., M. v. Veenendaal, T. P. Devereaux, and J. P. Hill, 2011, Rev. Mod. Phys. **83**, 705–767.
Ancilotto, F., G. L. Chiarotti, S. Scandolo, and E. Tosatti, 1997, Science **275**, 1288–1290.
Andres, K., J. Graebner, and H. R. Ott, 1975, Phys. Rev. Lett. **35**, 1779–1782.
Antonangeli, D., D. L. Farber, A. H. Said, L. R. Benedetti, C. M. Aracne, A. Landa, P. Söderlind, and J. E. Klepeis, 2010, Phys. Rev. B **82**, 132101.
Apetrei, A., I. Mirebeau, I. Goncharenko, D. Andreica, and P. Bonville, 2007, J. Phys. Condens. Matter **19**, 145214.
Ashcroft, N. W., 1968, Phys. Rev. Lett. **21**, 1748–1750.
Ashcroft, N. W., 2002, Nature (London) **419**, 569–572.
Ashcroft, N. W., 2004, Phys. Rev. Lett. **92**, 187002.
Ashcroft, N. W., and M. Cyrot, 1993, Europhys. Lett. **23**, 605–608.
Azadi, S., B. Monserrat, W. M. C. Foulkes, and R. J. Needs, 2014, Phys. Rev. Lett. **112**, 165501.
Babaev, E., A. Sudbø, and N. W. Ashcroft, 2004, Nature (London) **431**, 666–668.
Babaev, E., A. Sudbø, and N. W. Ashcroft, 2005, Phys. Rev. Lett. **95**, 105301.
Badro, J., 2014, Annu. Rev. Earth Planet Sci. **42**, 231–248.
Badro, J., G. Fiquet, F. Guyot, J.-P. Rueff, V. V. Struzhkin, G. Vanko, and G. Monaco, 2003, Science **300**, 789–791.
Badro, J., G. Fiquet, V. V. Struzhkin, M. Somayazulu, H. K. Mao, G. Shen, and T. LeBihan, 2002, Phys. Rev. Lett. **89**, 205504.
Bahramy, M. S., B.-J. Yang, R. Arita, and N. Nagaosa, 2012, Nat. Commun. **3**, 679.
Baldini, M., Y. Ding, S. Wang, Y. Lin, C. A. Tulk, A. M. d. Santos, J. F. Mitchell, D. Haskel, and W. L. Mao, 2012, Phys. Rev. B **86**, 094407.
Baldini, M., T. Muramatsub, M. Sherafatic, H.-k. Mao, L. Malavasi, P. Postorino, S. Satpathy, and V. V. Struzhkin, 2015, Proc. Natl. Acad. Sci. U.S.A. **112**, 10869–10872.
Baldini, M., V. V. Struzhkin, A. F. Goncharov, P. Postorino, and W. L. Mao, 2011, Phys. Rev. Lett. **106**, 066402.
Basov, D. N., R. D. Averitt, D. van der Marel, M. Dressel, and K. Haule, 2011, Rev. Mod. Phys. **83**, 471–541.
Bassett, W. A., 1979, Annu. Rev. Earth Planet Sci. **7**, 357–384.
Bassett, W. A., 2009, High Press. Res. **29**, 163–186.
Bassett, W. A., H. J. Reichmann, R. J. Angel, H. Spetzler, and J. R. Smyth, 2000, Am. Mineral. **85**, 283–287.
Bassett, W. A., T. Takahashi, and P. Stook, 1967, Rev. Sci. Instrum. **38**, 37–42.
Bauer, E. D., N. A. Frederick, P. C. Ho, V. S. Zapf, and M. B. Maple, 2002, Phys. Rev. B **65**, 100506(R).
Bauer, E. D., H. O. Lee, V. A. Sidorov, N. Kurita, K. Gofryk, J. X. Zhu, F. Ronning, R. Movshovich, J. D. Thompson, and T. Park, 2010, Phys. Rev. B **81**, 180507(R).
Beck, P., A. F. Goncharov, V. V. Struzhkin, B. Militzer, H. K. Mao, and R. J. Hemley, 2007, Appl. Phys. Lett. **91**, 181914.
Bell, P. M., and H. K. Mao, 1981, Carnegie Inst. Washington Yearb. **80**, 404–406.
Berthier, C., P. Molinie, and D. Jérome, 1976, Solid State Commun. **18**, 1393–1395.
Bi, W., Y. Meng, R. S. Kumar, A. L. Cornelius, W. W. Tipton, R. G. Hennig, Y. Zhang, C. Chen, and J. S. Schilling, 2011, Phys. Rev. B **83**, 104106.
Bi, W., *et al.*, 2012, Phys. Rev. B **85**, 205134.
Boehler, R., 2000, Rev. Geophys. **38**, 221–246.
Boehler, R., 2006, Rev. Sci. Instrum. **77**, 115103.
Boehler, R., and K. De Hantsetters, 2004, High Press. Res. **24**, 391–396.
Boehler, R., M. Guthrie, J. J. Molaison, A. M. d. Santos, S. Sinogeikin, S. Machida, N. Pradhan, and C. A. Tulk, 2013, High Press. Res. **33**, 546–554.
Boehler, R., M. Nicol, C. S. Zha, and M. L. Johnson, 1986, Physica B+C (Amsterdam) **139–140**, 916–918.
Braithwaite, D., B. Salce, G. Lapertot, F. Bourdarot, C. Marin, D. Aoki, and M. Hanfland, 2009, J. Phys. Condens. Matter **21**, 232202.
Bridgman, P. W., 1935, Rev. Mod. Phys. **7**, 1–33.
Bundy, F. P., and K. J. Dunn, 1981, Phys. Rev. B **24**, 4136–4141.
Cadien, A., Q. Y. Hu, Y. Meng, Y. Q. Cheng, M. W. Chen, J. F. Shu, H. K. Mao, and H. W. Sheng, 2013, Phys. Rev. Lett. **110**, 125503.
Cai, Y. Q., *et al.*, 2005, Phys. Rev. Lett. **94**, 025502.
Calamiotou, M., A. Gantis, E. Siranidi, D. Lampakis, J. Karpinski, and E. Liarokapis, 2009, Phys. Rev. B **80**, 214517.
Campbell, A. J., 2008, Rev. Sci. Instrum. **79**, 015108.
Chen, B., K. Lutker, J. Lei, J. Yan, S. Yang, and H. K. Mao, 2014, Proc. Natl. Acad. Sci. U.S.A. **111**, 3350–3353.
Chen, B., K. Lutker, S. V. Raju, J. Yan, W. Kanitpanyacharoen, J. Lei, S. Yang, H.-R. Wenk, H. K. Mao, and Q. Williams, 2012, Science **338**, 1448–1451.
Chen, J.-Y., C.-S. Yoo, W. J. Evans, H.-P. Liermann, H. Cynn, M. Kim, and Z. Jenei, 2014, Phys. Rev. B **90**, 144104.
Chen, S. J., Y. C. Liu, C. L. Shao, C. S. Xu, Y. X. Liu, L. Wang, B. B. Liu, and G. T. Zou, 2006, J. Appl. Phys. **99**, 066102.
Chen, X. J., and Z. K. Jiao, 1997, Phys. Rev. B **56**, 6302–6307.
Chen, X. J., H. Q. Lin, and C. D. Gong, 2000, Phys. Rev. Lett. **85**, 2180–2183.
Chen, X. J., V. V. Struzhkin, R. J. Hemley, and H. K. Mao, 2004, Phys. Rev. B **70**, 214502.
Chen, X. J., V. V. Struzhkin, Y. Song, A. F. Goncharov, M. Ahart, Z. Liu, H. K. Mao, and R. J. Hemley, 2008, Proc. Natl. Acad. Sci. U.S.A. **105**, 20–23.
Chen, X. J., V. V. Struzhkin, Z. Wu, R. J. Hemley, and H. K. Mao, 2007, Phys. Rev. B **75**, 134504.
Chen, X. J., V. V. Struzhkin, Y. Yu, A. F. Goncharov, C.-T. Lin, H. K. Mao, and R. J. Hemley, 2010, Nature (London) **466**, 950–953.
Chen, X. J., and H. Su, 2005, Phys. Rev. B **71**, 094512.
Chen, X. J., J. L. Wang, V. V. Struzhkin, H. K. Mao, R. J. Hemley, and H. Q. Lin, 2008, Phys. Rev. Lett. **101**, 077002.
Chen, X. J., C. Zhang, M. Yue, R. Q. Zhang, H. Q. Lin, V. V. Struzhkin, and H. K. Mao, 2011, Phys. Rev. Lett. **106**, 135502.
Chen, Y. L., *et al.*, 2009, Science **325**, 178–181.
Chen, Y. L., *et al.*, 2013, Nat. Phys. **9**, 704–708.
Cheng, J., *et al.*, 2015, Proc. Natl. Acad. Sci. U.S.A. **112**, 1670–1674.
Cheng, Y., C. Zhang, T. T. Wang, G. H. Zhong, C. L. Yang, X. J. Chen, and H. Q. Lin, 2015, Sci. Rep. **5**, 16475.
Cheong, S.-W., and H. Y. Hwang, 2000, in *Colossal Magnetoresistive Oxides*, edited by Y. Tokura (Gordon & Breach, Reading, UK).
Chervin, J. C., B. Canny, J. M. Besson, and P. Pruzan, 1995, Rev. Sci. Instrum. **66**, 2595–2598.
Chi, Z. H., X.-M. Zhao, H. Zhang, A. F. Goncharov, S. S. Lobanov, T. Kagayama, M. Sakata, and X. J. Chen, 2014, Phys. Rev. Lett. **113**, 036802.
Chijioke, A. D., W. J. Nellis, A. Soldatov, and I. F. Silvera, 2005, J. Appl. Phys. **98**, 114905–114909.

Chou, I. M., J. Blank, A. F. Goncharov, H. K. Mao, and R. J. Hemley, 1998, Science **281**, 809–812.
Chow, P., Y. M. Xiao, E. Rod, L. G. Bai, G. Y. Shen, S. Sinogeikin, N. Gao, Y. Ding, and H. K. Mao, 2015, Rev. Sci. Instrum. **86**, 072203.
Chu, C. W., and B. Lorenz, 2009, Physica C (Amsterdam) **469**, 385–395.
Collins, G. W., L. B. Da Silva, P. Celliers, D. M. Gold, M. E. Foord, R. J. Wallace, A. Ng, S. V. Weber, K. S. Budil, and R. Cauble, 1998, Science **281**, 1178–1181.
Csontos, M., G. Mihály, B. Jankó, T. Wojtowicz, X. Liu, and J. K. Furdyna, 2005, Nat. Mater. **4**, 447–449.
Cudazzo, P., G. Profeta, A. Sanna, A. Floris, A. Continenza, S. Massidda, and E. K. U. Gross, 2008, Phys. Rev. Lett. **100**, 257001.
Cui, H. B., H. Kobayashi, S. Ishibashi, M. Sasa, F. Iwase, R. Kato, and A. Kobayashi, 2014, J. Am. Chem. Soc. **136**, 7619–7622.
Cuk, T., V. V. Struzhkin, T. P. Devereaux, A. F. Goncharov, C. A. Kendziora, H. Eisaki, H. K. Mao, and Z.-X. Shen, 2008, Phys. Rev. Lett. **100**, 217003.
Cunsolo, A., *et al.*, 2015, Sci. Rep. **5**, 14996.
Dagotto, E., 2013, Rev. Mod. Phys. **85**, 849–867.
Dalladay-Simpson, P., R. T. Howie, and E. Gregoryanz, 2016, Nature (London) **529**, 63–67.
Dang, N. T., D. P. Kozlenko, S. E. Kichanov, L. S. Dubrovinsky, Z. Jirák, D. M. Levin, E. V. Lukin, and B. N. Savenko, 2013, JETP Lett. **97**, 540–545.
Datchi, F., A. Dewaele, P. Loubeyre, R. Letoullec, Y. L. Godec, and B. Canny, 2007, High Press. Res. **27**, 447–463.
Debessai, M., T. Matsuoka, J. J. Hamlin, J. S. Schilling, and K. Shimizu, 2009, Phys. Rev. Lett. **102**, 197002.
Decremps, F., D. Antonangeli, M. Gauthier, S. Ayrinhac, M. Morand, G. Le Marchand, F. Bergame, and J. Philippe, 2014, Geophys. Res. Lett. **41**, 1459–1464.
Deemyad, S., and J. S. Schilling, 2003, Phys. Rev. Lett. **91**, 167001.
Degtyareva, O., M. M. Canales, A. Bergara, X. J. Chen, Yang Song, V. V. Struzhkin, H. K. Mao, and R. J. Hemley, 2007, Phys. Rev. B **76**, 064123.
Delaplace, R., Ph. Molinie, and D. Jerome, 1994, J. Phys. Conf. Ser. **37**, L13–L16.
de' Medici, L., A. Georges, G. Kotliar, and S. Biermann, 2005, Phys. Rev. Lett. **95**, 066402.
Dewaele, A., and P. Loubeyre, 2007, High Press. Res. **27**, 419–429.
Dewaele, A., N. Worth, C. J. Pickard, R. J. Needs, S. Pascarelli, O. Mathon, M. Mezouar, and T. Irifune, 2016, Nat. Chem. **8**, 784–790.
Dhaka, R. S., *et al.*, 2011, Phys. Rev. Lett. **107**, 267002.
Dias, R., and I. F. Silvera, 2017, Science **355**, 715–718; **357**, eaao5843(E) (2017).
Ding, Y., R. Ahuja, J. Shu, P. Chow, W. Luo, and H. K. Mao, 2007, Phys. Rev. Lett. **98**, 085502.
Ding, Y., J. Fernandez-Rodriguez, J. Kim, F. Li, D. Casa, M. Upton, T. Gog, H. K. Mao, and M. van Veenendaal, 2012, Phys. Rev. B **86**, 094107.
Ding, Y., D. Haskel, S. G. Ovchinnikov, Y.-C. Tseng, Y. S. Orlov, J. C. Lang, and H. K. Mao, 2008, Phys. Rev. Lett. **100**, 045508.
Ding, Y., D. Haskel, Y. C. Tseng, E. Kaneshita, M. van Veenendaal, J. Mitchell, S. V. Sinogeikin, V. Prakapenka, and H. K. Mao, 2009, Phys. Rev. Lett. **102**, 237201.
Ding, Y., Y. Ren, P. Chow, J. Zhang, S. C. Vogel, B. Winkler, J. Xu, Y. Zhao, and H. K. Mao, 2006, Phys. Rev. B **74**, 144101.
Ding, Y., *et al.*, 2005, Appl. Phys. Lett. **86**, 052505.
Ding, Y., *et al.*, 2014, Phys. Rev. Lett. **112**, 056401.
Ding, Y., *et al.*, 2016, Phys. Rev. Lett. **116**, 216402.
Doniach, S., 1977, Physica B + C (Amsterdam) **91**, 231–234.
Dorogokupets, P. I., and A. R. Oganov, 2007, Phys. Rev. B **75**, 024115.
Drozdov, A. P., M. I. Eremets, I. A. Troyan, V. Ksenofontov, and S. I. Shylin, 2015, Nature (London) **525**, 73–76.
Du, C. H., W. J. Lin, Y. Su, B. K. Tanner, P. D. Hatton, D. Casa, B. Keimer, J. P. Hill, C. S. Oglesby, and H. Hohl, 2000, J. Phys. Condens. Matter **12**, 5361–5370.
Du, Z., L. Miyagi, G. Amulele, and K. K. M. Lee, 2013, Rev. Sci. Instrum. **84**, 024502.
Duan, D. F., Y. Liu, F. Tian, D. Li, X. Huang, Z. Zhao, H. Yu, B. Liu, W. Tian, and T. Cui, 2014, Sci. Rep. **4**, 6968.
Duband, P., G. R. Darling, Y. Dubitsky, A. Zaopo, and M. J. Rosseinsky, 2003, Nat. Mater. **2**, 605–610.
Dubrovinskaia, N., and L. Dubrovinsky, 2003, Rev. Sci. Instrum. **74**, 3433–3437.
Dubrovinskaia, N., L. Dubrovinsky, N. A. Solopova, A. Abakumov, S. Turner, M. Hanfland, E. Bykova, M. Bykov, C. Prescher, and V. B. Prakapenka, 2016, Sci. Adv. **2**, e1600341.
Dubrovinsky, L., N. Dubrovinskaia, V. B. Prakapenka, and A. M. Abakumov, 2012, Nat. Commun. **3**, 1163.
Dubrovinsky, L., *et al.*, 2015, Nature (London) **525**, 226–229.
Dubrovinsky, L. S., S. K. Saxena, and P. Lazor, 1997, Geophys. Res. Lett. **24**, 1835–1838.
Duffy, T. S., 2005, Rep. Prog. Phys. **68**, 1811–1859.
Dunn, K. J., and F. P. Bundy, 1981, Phys. Rev. B **24**, 1643–1650.
Dzero, M., M. R. Norman, I. Paul, C. Pépin, and J. Schmalian, 2006, Phys. Rev. Lett. **97**, 185701.
Einaga, M., M. Sakata, T. Ishikawa, K. Shimizu, M. I. Eremets, A. P. Drozdov, I. A. Troyan, N. Hirao, and Y. Ohishi, 2016, Nat. Phys. **12**, 835–838.
Eremets, M. I., E. Gregoryanz, V. V. Struzhkin, H. K. Mao, R. J. Hemley, N. Moulders, and N. M. Zimmerman, 2000, Phys. Rev. Lett. **85**, 2797–2800.
Eremets, M. I., V. V. Struzhkin, R. J. Hemley, and H. K. Mao, 2001, Science **293**, 272–274.
Eremets, M. I., I. A. Trojan, S. A. Medvedev, J. S. Tse, and Y. Yao, 2008, Science **319**, 1506–1509.
Eremets, M. I., and I. A. Troyan, 2011, Nat. Mater. **10**, 927–931.
Evans, W. J., C.-S. Yoo, G. W. Lee, H. Cynn, M. J. Lipp, and K. Visbeck, 2007, Rev. Sci. Instrum. **78**, 073904.
Farber, D. L., M. Krisch, D. Antonangeli, and A. Beraud, 2006, Phys. Rev. Lett. **96**, 115502.
Farrell, J. N., and R. D. Taylor, 1987, Phys. Rev. Lett. **58**, 2478.
Feng, Y., *et al.*, 2007, Phys. Rev. Lett. **99**, 137201.
Feng, Y. J., J. Y. Wang, R. Jaramillo, J. van Wezel, S. Haravifard, G. Srajer, Y. Liu, Z.-A. Xu, P. B. Littlewood, and T. F. Rosenbaum, 2012, Proc. Natl. Acad. Sci. U.S.A. **109**, 7224.
Finkelstein, G. J., P. K. Dera, S. Jahn, A. R. Oganov, C. M. Holl, Y. Meng, and T. S. Duffy, 2014, Am. Mineral. **99**, 35–43.
Fischer, R. A., A. J. Campbell, O. T. Lord, G. A. Shofner, P. Dera, and V. B. Prakapenka, 2011, Geophys. Res. Lett. **38**, L24301.
Forman, R. A., G. J. Piermarini, J. D. Barnett, and S. Block, 1972, Science **176**, 284–285.
Fu, L., and E. Berg, 2010, Phys. Rev. Lett. **105**, 097001.
Fujihisa, H., and K. Takemura, 1995, Phys. Rev. B **52**, 13257–13260.
Funamori, N., and T. Sato, 2008, Rev. Sci. Instrum. **79**, 053903.
Ganin, A. Y., Y. Takabayashi, Y. Z. Khimyak, S. Margadonna, A. Tamai, M. J. Rosseinsky, and K. Prassides, 2008, Nat. Mater. **7**, 367–371.
Gao, C., *et al.*, 2005, Rev. Sci. Instrum. **76**, 083912.

Gao, G. Y., A. R. Oganov, A. Bergara, M. Martinez-Canales, T. Cui, T. Iitaka, Y. M. Ma, and G. T. Zou, 2008, Phys. Rev. Lett. **101**, 107002.
Gao, L., Y. Y. Xue, F. Chen, Q. Xiong, R. L. Meng, D. Ramirez, C. W. Chu, J. H. Eggert, and H. K. Mao, 1994a, Phys. Rev. B **50**, 4260–4263.
Gavriliuk, A. G., I. A. Trojan, and V. V. Struzhkin, 2012, Phys. Rev. Lett. **109**, 086402.
Ge, J.-F., Z.-L. Liu, C. Liu, C.-L. Gao, D. Qian, Q.-K. Xue, Y. Liu, and J.-F. Jia, 2015, Nat. Mater. **14**, 285–289.
Gleason, A. E., and W. L. Mao, 2013, Nat. Geosci. **6**, 571–574.
Gleason, A. E. *et al.*, 2015, Nat. Commun. **6**, 8191.
Goettel, K. A., H. K. Mao, and P. M. Bell, 1985, Rev. Sci. Instrum. **56**, 1420–1427.
Goncharov, A. F., S. S. Lobanov, I. Kruglov, X. M. Zhao, X. J. Chen, A. R. Oganov, Z. Konôpková, and V. B. Prakapenka, 2016, Phys. Rev. B **93**, 174105.
Goncharov, A. F., and V. V. Struzhkin, 2003, J. Raman Spectrosc. **34**, 532–548.
Graf, D., R. Stillwell, T. P. Murphy, J.-H. Park, E. C. Palm, P. Schlottmann, R. D. McDonald, J. G. Analytis, I. R. Fisher, and S. W. Tozer, 2012, Phys. Rev. B **85**, 134503.
Gregoryanz, E., O. Degtyareva, M. Somayazulu, R. J. Hemley, and H. K. Mao, 2005, Phys. Rev. Lett. **94**, 185502.
Gregoryanz, E., L. F. Lundegaard, M. I. McMahon, C. Guillaume, R. J. Nelmes, and M. Mezouar, 2008, Science **320**, 1054–1057.
Gregoryanz, E., C. Sanloup, M. Somayazulu, J. Badro, G. Fiquet, R. J. Hemley, and H. K. Mao, 2004, Nat. Mater. **3**, 294–297.
Grimsditch, M., and A. Polian, 1989, in *Brillouin scattering at high pressures*, edited by A. Polian and P. Loubeyre (Plenum Press, New York).
Grzybowski, T. A., and A. L. Ruoff, 1984, Phys. Rev. Lett. **53**, 489–492.
Guguchia, Z., A. Maisuradze, G. Ghambashidze, R. Khasanov, A. Shengelaya, and H. Keller, 2013, New J. Phys. **15**, 093005.
Guillaume, C. L., E. Gregoryanz, O. Degtyareva, M. I. McMahon, S. Evans, M. Hanfland, M. Guthrie, S. V. Sinogeikin, and H. K. Mao, 2011, Nat. Phys. **7**, 211–214.
Guo, J., *et al.*, 2012, Phys. Rev. Lett. **108**, 197001.
Guo, Q., H. K. Mao, J. Hu, J. Shu, and R. J. Hemley, 2002, J. Phys. Condens. Matter **14**, 11369–11374.
Hagel, J., J. Wosnitza, C. Pfleiderer, J. A. Schlueter, J. Mohtasham, and G. L. Gard, 2003, Phys. Rev. B **68**, 104504.
Hanfland, M., K. Syassen, N. E. Christensen, and D. L. Novikov, 2000, Nature (London) **408**, 174–178.
Harrison, W. A., 1989, *Electronic Structure and the Properties of Solids: The Physics of the Chemical Bond* (Dover Publications, Inc., New York).
He, D., *et al.*, 2003, Rev. Sci. Instrum. **74**, 3012–3016.
He, S., *et al.*, 2013, Nat. Mater. **12**, 605–610.
Hegger, H., C. Petrovic, E. G. Moshopoulou, M. F. Hundley, J. L. Sarrao, Z. Fisk, and J. D. Thompson, 2000, Phys. Rev. Lett. **84**, 4986–4989.
Hemley, R. J., 2000, Annu. Rev. Phys. Chem. **51**, 763–800.
Hemley, R. J., M. Hanfland, and H. K. Mao, 1991, Nature (London) **350**, 488–491.
Hemley, R. J., A. P. Jephcoat, H. K. Mao, L. C. Ming, and M. Manghnani, 1988, Nature (London) **334**, 52–54.
Hemley, R. J., H. K. Mao, A. F. Goncharov, M. Hanfland, and V. V. Struzhkin, 1996, Phys. Rev. Lett. **76**, 1667–1670.
Hemley, R. J., H. K. Mao, G. Shen, J. Badro, P. Gillet, M. Hanfland, and D. Häusermann, 1997, Science **276**, 1242–1245.
Hemmes, H., A. Driessen, J. Kos, F. A. Mul, R. Griessen, and J. Caro, 1989, Rev. Sci. Instrum. **60**, 474–480.
Hill, J. P., C. C. Kao, W. A. C. Caliebe, D. Gibbs, and J. B. Hastings, 1996, Phys. Rev. Lett. **77**, 3665–3668.
Holzapfel, W. B., 2003, J. Appl. Phys. **93**, 1813–1818.
Hor, Y. S., A. J. Williams, J. G. Checkelsky, P. Roushan, J. Seo, Q. Xu, H. W. Zandbergen, A. Yazdani, N. P. Ong, and R. J. Cava, 2010, Phys. Rev. Lett. **104**, 057001.
Howie, R. T., P. Dalladay-Simpson, and E. Gregoryanz, 2015, Nat. Mater. **14**, 495–499.
Howie, R. T., C. L. Guillaume, T. Scheler, A. F. Goncharov, and E. Gregoryanz, 2012, Phys. Rev. Lett. **108**, 125501.
Howie, R. T., I. B. Magdău, A. F. Goncharov, G. J. Ackland, and E. Gregoryanz, 2014, Phys. Rev. Lett. **113**, 175501.
Hsieh, D., D. Qian, L. Wray, Y. Xia, Y. S. Hor, R. J. Cava, and M. Z. Hasan, 2008, Nature (London) **452**, 970–974.
Hsieh, D., *et al.*, 2009, Phys. Rev. Lett. **103**, 146401.
Hsu, F. C., *et al.*, 2008, Proc. Natl. Acad. Sci. U.S.A. **105**, 14262–14264.
Hu, Q. Y., D. Y. Kim, W. Yang, L. Yang, Y. Meng, L. Zhang, and H. K. Mao, 2016, Nature (London) **534**, 241–244.
Hu, Q. Y., J. F. Shu, A. Cadien, Y. Meng, W. G. Yang, H. W. Sheng, and H. K. Mao, 2015, Nat. Commun. **6**, 6630.
Huang, Q., Y. Qiu, W. Bao, M. A. Green, J. W. Lynn, Y. C. Gasparovic, T. Wu, G. Wu, and X. H. Chen, 2008, Phys. Rev. Lett. **101**, 257003.
Huang, Q., *et al.*, 2014, Nature (London) **510**, 250–253.
Hücker, M., M. v. Zimmermann, M. Debessai, J. S. Schilling, J. M. Tranquada, and G. D. Gu, 2010, Phys. Rev. Lett. **104**, 057004.
Hwang, H. Y., T. T. M. Palstra, S. W. Cheong, and B. Batlogg, 1995, Phys. Rev. B **52**, 15046–15049.
Imada, M., A. Fujimori, and Y. Tokura, 1998, Rev. Mod. Phys. **70**, 1039–1263.
Irifune, T., A. Kurio, S. Sakamoto, T. Inoue, and H. Sumiya, 2003, Nature (London) **421**, 599–600.
Ishizuka, M., 2005, Rev. Sci. Instrum. **76**, 123902.
Ishizuka, M., K. Amaya, and S. Endo, 1995, Rev. Sci. Instrum. **66**, 3307.
Jaccard, D., K. Behnia, and J. Sierro, 1992, Phys. Lett. A **163**, 475–480.
Jackson, J. M., W. Sturhahn, G. Y. Shen, J. Y. Zhao, M. Y. Hu, D. Errandonea, J. D. Bass, and Y. Fei, 2005, Am. Mineral. **90**, 199–205.
Jacobsen, S. D., H. J. Reichmann, H. A. Spetzler, S. J. Mackwell, J. R. Smyth, R. J. Angel, and C. A. McCammon, 2002, J. Geophys. Res. **107**, 2037–2041.
Jacobsen, S. D., H. Spetzler, H. J. Reichmann, and J. R. Smyth, 2004, Proc. Natl. Acad. Sci. U.S.A. **101**, 5867–5871.
Jaffe, J. E., and N. W. Ashcroft, 1981, Phys. Rev. B **23**, 6176–6179.
Jang, J.-I., M. J. Lance, S. Wen, and G. M. Pharr, 2005, Appl. Phys. Lett. **86**, 131907.
Jayaraman, A., 1983, Rev. Mod. Phys. **55**, 65–108.
Jérome, D., A. Mazaud, M. Ribault, and K. Bechgarrd, 1980, J. Phys. Lett. **41**, 95–98.
Ji, C., *et al.*, 2017, Proc. Natl. Acad. Sci. U.S.A. **114**, 3596–3600.
Jiang, H., *et al.*, 2013, Phys. Rev. Lett. **110**, 205501.
Joe, Y. I., *et al.*, 2014, Nat. Phys. **10**, 421–431.
Johansson, B., 1974, Philos. Mag. **30**, 469–482.
Johansson, B., and A. Rosengren, 1975, Phys. Rev. B **11**, 2836–2839.

Julian, S. R., *et al.*, 1998, J. Magn. Magn. Mater. **177–181**, 265–269.
Kambe, T., *et al.*, 2012, Phys. Rev. B **86**, 214507.
Kano, M., K. Uchiyama, H. Taniguchi, M. Hedo, K. Matsubayashi, and Y. Uwatoko, 2009, J. Phys. Conf. Ser. **150**, 052093.
Kantor, I., V. Prakapenka, A. Kantor, P. Dera, A. Kurnosov, S. Sinogeikin, N. Dubrovinskaia, and L. Dubrovinsky, 2012, Rev. Sci. Instrum. **83**, 125102.
Khomskii, D., 2010, *Basic Aspects of the Quantum Theory of Solids: Order and Elementary Excitations* (Cambridge University Press, New York).
Khomskii, D. I., 2014, *Transition Metal Compounds* (Cambridge, Cambridge, United Kingdom).
Kim, D. Y., R. H. Scheicher, C. J. Pickard, R. J. Needs, and R. Ahuja, 2011, Phys. Rev. Lett. **107**, 117002.
Kim, J., V. V. Struzhkin, S. G. Ovchinnikov, Y. Orlov, Y. Shvyd'ko, M. H. Upton, D. Casa, A. G. Gavriliuk, and S. V. Sinogeikin, 2014, Europhys. Lett. **108**, 37001.
Kim, M., M. Debessai, and C.-S. Yoo, 2010, Nat. Chem. **2**, 784–788.
Kimber, S. A. J., *et al.*, 2009, Nat. Mater. **8**, 471–475.
Kirshenbaum, K., P. S. Syers, A. P. Hope, N. P. Butch, J. R. Jeffries, S. T. Weir, J. J. Hamlin, M. B. Maple, Y. K. Vohra, and J. Paglione, 2013, Phys. Rev. Lett. **111**, 087001.
Kiss, T., T. Yokoya, A. Chainani, S. Shin, T. Hanaguri, M. Nohara, and H. Takagi, 2007, Nat. Phys. **3**, 720–726.
Klotz, S., 2001, Z. Kristallogr. **216**, 420–429.
Klotz, S., J. Chervin, P. Munsch, and G. Le Marchand, 2009, J. Phys. D **42**, 075413.
Knudson, M. D., M. P. Desjarlais, A. Becker, R. W. Lemke, K. R. Cochrane, M. E. Savage, D. E. Bliss, T. R. Mattsson, and R. Redmer, 2015, Science **348**, 1455–1459.
Kojima, N., and N. Matsushita, 2000, Coord. Chem. Rev. **198**, 251–263.
Kondo, J., 1964, Prog. Theor. Phys. **32**, 37–49.
Konôpková, Z., R. S. McWilliams, N. Gómez-Pérez, and A. F. Goncharov, 2016, Nature (London) **534**, 99–101.
Krisch, M., F. Sette, C. Masciovecchio, and R. Verbeni, 1997, Phys. Rev. Lett. **78**, 2843–2846.
Küchler, R., *et al.*, 2003, Phys. Rev. Lett. **91**, 066405.
Kumaresavanji, M., E. M. B. Saitovitch, J. P. Araujo, and M. B. Fontes, 2013, J. Mater. Sci. **48**, 1324–1329.
Kusmartseva, A., F. B. Sipos, H. Berger, L. Forro, and E. Tutis, 2009, Phys. Rev. Lett. **103**, 236401.
Landa, A., J. Klepeis, P. Söderlind, I. Naumov, L. Vitos, and A. Ruban, 2006, J. Phys. Condens. Matter **18**, 5079–5083.
Lazicki, A., A. F. Goncharov, V. V. Struzhkin, R. E. Cohen, Z. Liu, E. Gregoryanz, C. Guillaume, H. K. Mao, and R. J. Hemley, 2009, Proc. Natl. Acad. Sci. U.S.A. **106**, 6525–6528.
Lee, G. W., W. J. Evans, and C.-S. Yoo, 2007, Proc. Natl. Acad. Sci. U.S.A. **104**, 9178–9181.
Lee, K. K. M., B. O'Neill, and R. Jeanloz, 2004, Phys. Earth Planet. Inter. **143–144**, 241–253.
Lee, S. K., P. J. Eng, and H. K. Mao, 2014, in *Probing of pressure-induced bonding transitions in crystalline and amorphous Earth materials: Insights from X-ray Raman scattering at high pressure*, edited by J. J. Rosso (Mineralogical Society of America, Chantilly, VA), pp. 139–174.
Lee, S. K., P. J. Eng, H. K. Mao, Y. Meng, M. Newville, M. Y. Hu, and J. Shu, 2005, Nat. Mater. **4**, 851–854.
Lee, S. K., P. J. Eng, H. K. Mao, Y. Meng, and J. Shu, 2007, Phys. Rev. Lett. **98**, 105502.
Leroux, M., I. Errea, M. Le Tacon, S. M. Souliou, G. Garbarino, L. Cario, A. Bosak, F. Mauri, M. Calandra, and P. Rodiere, 2015, Phys. Rev. B **92**, 140303(R).
Letoullec, R., J. Pinceaux, and P. Loubeyre, 1988, Inter. J. High Press. Res. **1**, 77–90.
Li, B., Y. Ding, D. Kim, R. Ahuja, G. Zou, and H. K. Mao, 2011, Proc. Natl. Acad. Sci. U.S.A. **108**, 18618–18621.
Li, B., Y. Ding, W. Yang, L. Wang, B. Zou, J. Shu, S. Sinogeikin, C. Park, G. Zou, and H. K. Mao, 2012, Proc. Natl. Acad. Sci. U.S.A. **109**, 16459–16462.
Li, F., Q. Cui, Z. He, T. Cui, C. Gao, Q. Zhou, and G. Zou, 2006, Appl. Phys. Lett. **88**, 203507.
Li, H., X. Zhou, S. Parham, T. Nummy, J. Griffith, K. Gordon, E. L. Chronister, and D. S. Dessau, 2017, arXiv:1704.04230.
Li, Q., Y. Ma, A. R. Oganov, H. Wang, H. Wang, Y. Xu, T. Cui, H. K. Mao, and G. Zou, 2009, Phys. Rev. Lett. **102**, 175506.
Li, Y. W., G. Gao, Y. Xie, Y. M. Ma, T. Cui, and G. T. Zou, 2010, Proc. Natl. Acad. Sci. U.S.A. **107**, 15708–15712.
Li, Y. W., J. Hao, H. Liu, Y. Li, and Y. Ma, 2014, J. Chem. Phys. **140**, 174712.
Li, Y. W., J. Hao, H. Y. Liu, J. S. Tse, Y. C. Wang, and Y. M. Ma, 2015, Sci. Rep. **5**, 09948.
Li, Y. W., *et al.*, 2016, Phys. Rev. B **93**, 020103(R).
Lin, J.-F., M. Santoro, V. V. Struzhkin, H. K. Mao, and R. J. Hemley, 2004, Rev. Sci. Instrum. **75**, 3302–3306.
Lin, J. F., J. Shu, H. K. Mao, R. J. Hemley, and G. Shen, 2003, Rev. Sci. Instrum. **74**, 4732–4736.
Lin, J.-F., V. V. Struzhkin, S. D. Jacobsen, M. Y. Hu, P. Chow, J. Kung, H. Liu, H. K. Mao, and R. J. Hemley, 2005, Nature (London) **436**, 377–380.
Lin, Y., L. Zhang, H.-k. Mao, P. Chow, Y. Xiao, M. Baldini, J. Shu, and W. L. Mao, 2011, Phys. Rev. Lett. **107**, 175504.
Liu, L. G., and W. A. Bassett, 1975, J. Geophys. Res. **80**, 3777–3782.
Liu, X.-D., P. Dalladay-Simpson, R. T. Howie, B. Li, and E. Gregoryanz, 2017a, Science **357**, eaan2286.
Liu, Y., J. Wang, M. Azuma, W. L. Mao, and W. Yang, 2014, Appl. Phys. Lett. **104**, 043108.
Loa, I., P. Adler, A. Grzechni, K. Syassen, U. Schwarz, M. Hanfland, G. K. Rozenberg, P. Gorodetsky, and M. P. Pasternak, 2001, Phys. Rev. Lett. **87**, 125501.
Loa, I., E. I. Isaev, M. I. McMahon, D. Y. Kim, B. Johansson, A. Bosak, and M. Krisch, 2012, Phys. Rev. Lett. **108**, 045502.
Lobanov, S. S., P.-N. Chen, X. J. Chen, C. S. Zha, K. D. Litasov, H. K. Mao, and A. F. Goncharov, 2013, Nat. Commun. **4**, 2446.
Lokshin, K. A., Y. Zhao, D. He, W. L. Mao, H. K. Mao, R. J. Hemley, M. V. Lobanov, and M. Greenblatt, 2004, Phys. Rev. Lett. **93**, 125503.
Loubeyre, P., S. Brygoo, J. Eggert, P. M. Celliers, D. K. Spaulding, J. R. Rygg, T. R. Boehly, G. W. Collins, and R. Jeanloz, 2012, Phys. Rev. B **86**, 144115.
Loubeyre, P., R. LeToullec, D. Häusermann, M. Hanfland, R. J. Hemley, H. K. Mao, and L. W. Finger, 1996, Nature (London) **383**, 702–704.
Loubeyre, P., F. Occelli, and P. Dumas, 2013, Phys. Rev. B **87**, 134101.
Loubeyre, P., F. Occelli, and R. LeToullec, 2002, Nature (London) **416**, 613–617.
Lv, X., Q. Hu, W. Yang, L. Bai, H. Sheng, L. Wang, F. Huang, J. Wen, D. J. Miller, and Y. Zhao, 2013, J. Am. Chem. Soc. **135**, 13947–13953.
Lyons, T. W., C. T. Reinhard, and N. J. Planavsky, 2014, Nature (London) **506**, 307–315.

Lyubutin, I. S., S. G. Ovchinnikov, A. G. Gavriliuk, and V. V. Struzhkin, 2009, Phys. Rev. B **79**, 085125.
Ma, Y. M., M. Eremets, A. R. Oganov, Y. Xie, I. Trojan, S. Medvedev, A. O. Lyakhov, M. Valle, and V. Prakapenka, 2009, Nature (London) **458**, 182–185.
Ma, Y. M., E. Selvi, V. I. Levitas, and J. Hashemi, 2006, J. Phys. Condens. Matter **18**, S1075–S1082.
Maisuradze, A., A. Shengelaya, A. Amato, E. Pomjakushina, and H. Keller, 2011, Phys. Rev. B **84**, 184523.
Maiti, S., M. M. Korshunov, T. A. Maier, P. J. Hirschfeld, and A. V. Chubukov, 2011, Phys. Rev. Lett. **107**, 147002.
Mann, A. B., D. V. Heerden, J. B. Pethica, and T. P. Weihs, 2000, J. Mater. Res. **15**, 1754–1759.
Mao, H. K., and P. M. Bell, 1976, Science **191**, 851–852.
Mao, H. K., and P. M. Bell, 1978, Science **200**, 1145–1147.
Mao, H. K., and P. M. Bell, 1981, Rev. Sci. Instrum. **52**, 615–616.
Mao, H. K., Y. Ding, Y. Xiao, P. Chow, J. Shu, S. Lebègue, A. Lazicki, and R. Ahuja, 2011, Proc. Natl. Acad. Sci. U.S.A. **108**, 20434–20437.
Mao, H. K., and R. J. Hemley, 1989, Science **244**, 1462–1465.
Mao, H. K., and R. J. Hemley, 1994, Rev. Mod. Phys. **66**, 671–692.
Mao, H. K., J. Shu, G. Shen, R. J. Hemley, B. Li, and A. K. Singh, 1998, Nature (London) **396**, 741–743.
Mao, H. K., Y. Wu, L. C. Chen, J. F. Shu, and A. P. Jephcoat, 1990, J. Geophys. Res. **95**, 21737–21742.
Mao, H. K., Y. Wu, R. J. Hemley, L. C. Chen, J. F. Shu, and L. W. Finger, 1989, Science **246**, 649–651.
Mao, H. K., Y. Wu, R. J. Hemley, L. C. Chen, J. F. Shu, L. W. Finger, and D. E. Cox, 1990, Phys. Rev. Lett. **64**, 1749–1752.
Mao, H. K., J. Xu, and P. M. Bell, 1986, J. Geophys. Res. **91**, 4673–4676.
Mao, H. K., *et al.*, 2001, Science **292**, 914–916.
Mao, H. K., *et al.*, 2010, Phys. Rev. Lett. **105**, 186404.
Mao, W. L., H. K. Mao, P. Eng, T. Trainor, M. Newville, C. C. Kao, D. L. Heinz, J. Shu, Y. Meng, and R. J. Hemley, 2003, Science **302**, 425–427.
Mao, W. L., H. K. Mao, A. F. Goncharov, V. V. Struzhkin, Q. Guo, J. Hu, J. Shu, R. J. Hemley, M. Somayazulu, and Y. Zhao, 2002, Science **297**, 2247–2249.
Mao, W. L., H. K. Mao, Y. Meng, P. Eng, M. Y. Hu, P. Chow, Y. Q. Cai, J. Shu, and R. J. Hemley, 2006, Science **314**, 636–638.
Mao, W. L., *et al.*, 2010, Proc. Natl. Acad. Sci. U.S.A. **107**, 9965–9968.
Maple, B., W. Fertig, A. Mota, L. DeLong, D. Wohlleben, and R. Fitzgerald, 1972, Solid State Commun. **11**, 829–829.
Markopoulos, G., P. Kroll, and R. Hoffmann, 2010, J. Am. Chem. Soc. **132**, 748–755.
Marty, K., *et al.*, 2012, Phys. Rev. B **86**, 220509(R).
Mathur, N. D., F. M. Grosche, S. R. Julian, I. R. Walker, D. M. Freye, R. K. W. Haselwimmer, and G. G. Lonzarich, 1998, Nature (London) **394**, 39–43.
Matsubayashi, K., T. Terai, J. S. Zhou, and Y. Uwatoko, 2014, Phys. Rev. B **90**, 125126.
Matsuishi, K., E. Gregoryanz, H. K. Mao, and R. J. Hemley, 2003, J. Chem. Phys. **118**, 10683–10695.
Matsuoka, T., M. Sakata, Y. Nakamoto, K. Takahama, K. Ichimaru, K. Mukai, K. Ohta, N. Hirao, Y. Ohishi, and K. Shimizu, 2014, Phys. Rev. B **89**, 144103.
Matsuoka, T., and K. Shimizu, 2009, Nature (London) **458**, 186–189.
Mattila, A., J.-P. Rueff, J. Badro, G. Vankó, and A. Shukla, 2007, Phys. Rev. Lett. **98**, 196404.
McMahan, A. K., K. Held, and R. T. Scalettar, 2003, Phys. Rev. B **67**, 075108.
McMahan, A. K., C. Huscroft, R. T. Scalettar, and E. L. Pollock, 1998, J. Comput.-Aided Mater. Des. **5**, 131–162.
McMahon, J. M., and D. M. Ceperley, 2011, Phys. Rev. B **84**, 144515.
McMahon, J. M., M. A. Morales, C. Pierleoni, and D. M. Ceperley, 2012, Rev. Mod. Phys. **84**, 1607–1653.
McMahon, M. I., and G. J. Ackland, 2010, Nat. Mater. **9**, 607–608.
McWilliams, R. S., D. A. Dalton, Z. Konopkova, M. F. Mahmood, and A. F. Goncharov, 2015, Proc. Natl. Acad. Sci. U.S.A. **112**, 7925–7930.
McWilliams, R. S., D. A. Dalton, M. F. Mahmood, and A. F. Goncharov, 2016, Phys. Rev. Lett. **116**, 255501.
Medvedev, S., *et al.*, 2009, Nat. Mater. **8**, 630–633.
Meng, Y., P. J. Eng, J. S. Tse, D. M. Shaw, M. Y. Hu, J. Shu, S. A. Gramsch, C. Kao, R. J. Hemley, and H. K. Mao, 2008, Proc. Natl. Acad. Sci. U.S.A. **105**, 11640–11644.
Meng, Y., H. K. Mao, P. Eng, T. Trainor, M. Newville, M. Y. Hu, C. C. Kao, D. Häusermann, and R. J. Hemley, 2004, Nat. Mater. **3**, 111–114.
Merkel, S., A. Kubo, L. Miyagi, S. Speziale, T. S. Duffy, H. K. Mao, and H.-R. Wenk, 2006, Science **311**, 644–646.
Merkel, S., and T. Yagi, 2005, Rev. Sci. Instrum. **76**, 046109.
Merrill, L., and W. A. Bassett, 1974, Rev. Sci. Instrum. **45**, 290–294.
Miletich, R., D. Cinato, and S. Johänntgen, 2009, High Press. Res. **29**, 290–305.
Mills, R. L., D. H. Liebenberg, J. C. Bronson, and L. C. Schmidt, 1980, Rev. Sci. Instrum. **51**, 891–895.
Min, B. I., H. J. F. Jansen, T. Oguchi, and A. J. Freeman, 1986, J. Magn. Magn. Mater. **59**, 277.
Ming, L. C., and W. A. Bassett, 1974, Rev. Sci. Instrum. **45**, 1115–1118.
Miranda, E., and V. Dobrosavljevic, 2005, Rep. Prog. Phys. **68**, 2337–2341.
Mishima, O., L. D. Calvert, and E. Whalley, 1984, Nature (London) **310**, 393–395.
Miyagi, L., W. Kanitpanyacharoen, S. V. Raju, P. Kaercher, J. Knight, A. MacDowell, H.-R. Wenk, Q. Williams, and E. Z. Alarcon, 2013, Rev. Sci. Instrum. **84**, 025118.
Moliniè, P., D. Jérome, and A. J. Grant, 1974, Philos. Mag. **30**, 1091–1097.
Moncton, D. E., J. D. Axe, and F. J. Di Salvo, 1975, Phys. Rev. Lett. **34**, 734–737.
Morard, G., J. Siebert, D. Andrault, N. Guignot, G. Garbarino, F. Guyot, and D. Antonangeli, 2013, Earth Planet. Sci. Lett. **373**, 169–173.
Mori, H., S. Tanaka, and T. Mori, 1998, Phys. Rev. B **57**, 12023–12026.
Morosan, E., H. W. Zandbergen, B. S. Dennis, J. W. G. Bos, Y. Onose, T. Klimczuk, A. P. Ramirez, N. P. Ong, and R. J. Cava, 2006, Nat. Phys. **2**, 544–549.
Moshary, F., N. H. Chen, and I. F. Silvera, 1992, Phys. Rev. Lett. **69**, 466–469.
Mujica, A., A. Rubio, A. Muñoz, and R. J. Needs, 2003, Rev. Mod. Phys. **75**, 863–912.
Murakami, M., Y. Ohishi, N. Hirao, and K. Hirose, 2012, Nature (London) **485**, 90–94.
Murakami, M., S. V. Sinogeikin, H. Hellwig, J. D. Bass, and J. Li, 2007, Earth Planet. Sci. Lett. **256**, 47–50.
Muramatsu, T., D. Pham, and C. W. Chu, 2011, Appl. Phys. Lett. **99**, 052508.
Nakajima, Y., Renxiong Wang, r. Metz, X. Wang, L. Wang, H. Cynn, S. T. Weir, J. R. Jeffries, and J. Paglione, 2015, Phys. Rev. B **91**, 060508(R).

Nakamoto, T. K., M. Sakata, K. Shimizu, H. Fujihisa, T. Matsuoka, Y. Ohishi, and T. Kikegawa, 2010, Phys. Rev. B **81**, 140106(R).
Nakayama, A., *et al.*, 2014, J. Phys. Soc. Jpn. **83**, 093601.
Nayak, A. P., S. Bhattacharyya, J. Zhu, J. Liu, X. Wu, T. Pandey, C. Q. Jin, A. K. Singh, D. Akinwande, and J. F. Lin, 2014, Nat. Commun. **5**, 373.
Neaton, J. B., and N. W. Ashcroft, 1999, Nature (London) **400**, 141–144.
Neumeier, J. J., M. F. Hundley, J. D. Thompson, and R. H. Heffner, 1995, Phys. Rev. B **52**, R7006–R7009.
Niu, H., X. Q. Chen, S. Wang, D. Li, W. L. Mao, and Y. Li, 2012, Phys. Rev. Lett. **108**, 135501.
Nyrow, A., J. S. Tse, N. Hiraoka, S. Desgreniers, T. Büning, K. Mende, M. Tolan, M. Wilke, and C. Sternemann, 2014, Appl. Phys. Lett. **104**, 262408.
Occelli, F., P. Loubeyre, and R. LeToullec, 2003, Nat. Mater. **2**, 151–154.
Ohta, K., R. E. Cohen, K. Hirose, K. Haule, K. Shimizu, and Y. Ohishi, 2012, Phys. Rev. Lett. **108**, 026403.
Ohta, K., Y. Kuwayama, K. Hirose, K. Shimizu, and Y. Ohishi, 2016, Nature (London) **534**, 95–98.
Okabe, H., N. Takeshita, K. Horigane, T. Muranaka, and J. Akimitsu, 2010, Phys. Rev. B **81**, 205119.
Okada, K., and S. Yamada, 2012, Phys. Rev. B **86**, 064430.
Okada, S., K. Shimizu, T. C. Kobayashi, K. Amaya, and S. Endo, 1996, J. Phys. Soc. Jpn. **65**, 1924–1926.
Orloff, J., C. Narayana, and A. L. Ruoff, 2000, Rev. Sci. Instrum. **71**, 216–219.
Palmer, A., D. M. Silevitch, Y. Feng, Y. Wang, R. Jaramillo, A. Banerjee, Y. Ren, and T. F. Rosenbaum, 2015, Rev. Sci. Instrum. **86**, 093901.
Palstra, T. T. M., O. Zhou, Y. Iwasa, P. E. Sulewski, R. M. Fleming, and B. R. Zegarski, 1995, Solid State Commun. **93**, 327–330.
Pasternak, M. P., G. K. Rozenberg, G. Y. Machavariani, O. Naaman, R. D. Taylor, and R. Jeanloz, 1999, Phys. Rev. Lett. **82**, 4663–4666.
Pepin, C. M., G. Geneste, A. Dewaele, M. Mezouar, and P. Loubeyre, 2017, Science **357**, 382–385.
Phuoc, V. T., *et al.*, 2013, Phys. Rev. Lett. **110**, 037401.
Pickard, C. J., M. Martinez-Canales, and R. J. Needs, 2012, Phys. Rev. B **85**, 214114.
Pickard, C. J., and R. J. Needs, 2007, Nat. Phys. **3**, 473–476.
Piermarini, G. J., and S. Block, 1975, Rev. Sci. Instrum. **46**, 973–979.
Pigott, J. S., D. M. Reaman, and W. R. Panero, 2011, Rev. Sci. Instrum. **82**, 115106.
Postorino, P., A. Congeduti, P. Dore, A. Sacchetti, F. Gorelli, L. Ulivi, A. Kumar, and D. D. Sarma, 2003, Phys. Rev. Lett. **91**, 175501.
Potapkin, V., A. Chumakov, G. Smirnov, J. P. Celse, R. Rűffer, C. McCammonb, and L. Dubrovinsky, 2012, J. Synchrotron Radiat. **19**, 559.
Pratt, D. K., *et al.*, 2009, Phys. Rev. B **79**, 060510(R).
Qi, Q., J. Qian, X. Tan, J. Zhang, L. Wang, B. Xu, B. Zou, and W. Tian, 2015, Adv. Funct. Mater. **25**, 4005–4010.
Qi, X. L., and S. C. Zhang, 2011, Rev. Mod. Phys. **83**, 1057–1110.
Ramirez, R., and L. M. Falicov, 1971, Phys. Rev. B **3**, 2425–2430.
Ramos, A. Y., H. C. N. Tolentino, N. M. Souza-Neto, A. Caneiro, Y. Joly, J. P. Itié, A. M. Flank, and P. Lagarde, 2009, J. Phys. Conf. Ser. **190**, 012096.
Raphael, M. P., M. E. Reeves, and E. F. Skelton, 1998, Rev. Sci. Instrum. **69**, 1451–1455.
Ren, Z., L. V. Pourovskii, G. Lapertot, A. Georges, and D. Jaccard, 2014, Phys. Rev. X **4**, 031055.
Röhler, J., 1986, Physica B + C (Amsterdam) **144**, 27–32.
Roth, A., C. Brüne, H. Buhmann, L. W. Molenkamp, J. Maciejko, X. L. Qi, and S. C. Zhang, 2009, Science **325**, 294–297.
Rotter, M., M. Tegel, and D. Johrendt, 2008, Phys. Rev. Lett. **101**, 107006.
Rotundu, C. R., T. Ćuk, R. L. Greene, Z. X. Shen, R. J. Hemley, and V. V. Struzhkin, 2013, Rev. Sci. Instrum. **84**, 063903.
Rozenberg, G. K., L. S. Dubrovinsky, M. P. Pasternak, O. Naaman, T. Le Bihan, and R. Ahuja, 2002, Phys. Rev. B **65**, 064112.
Ruderman, M. A., and C. Kittel, 1954, Phys. Rev. **96**, 99–102.
Rueff, J. P., J. P. Itié, M. Taguchi, C. F. Hague, J. M. Mariot, R. Delaunay, J. P. Kappler, and N. Jaouen, 2006, Phys. Rev. Lett. **96**, 237403.
Rueff, J. P., C. C. Kao, V. V. Struzhkin, J. Badro, J. Shu, R. J. Hemley, and H. K. Mao, 1999, Phys. Rev. Lett. **82**, 3284–3287.
Rueff, J. P., S. Raymond, M. Taguchi, M. Sikora, J.-P. Itié, F. Baudelet, D. Braithwaite, G. Knebel, and D. Jaccard, 2011, Phys. Rev. Lett. **106**, 186405.
Rueff, J. P., and A. Shukla, 2010, Rev. Mod. Phys. **82**, 847–896.
Ruffell, S., J. E. Bradby, and J. S. Williams, 2006, Appl. Phys. Lett. **89**, 091919.
Ruoff, A. L., and C. A. Vanderborgh, 1991, Phys. Rev. Lett. **66**, 754–757.
Ruoff, A. L., H. Xia, H. Luo, and Y. K. Vohra, 1990, Rev. Sci. Instrum. **61**, 3830–3833.
Sakai, T., T. Yagi, H. Ohfuji, T. Irifune, Y. Ohishi, N. Hirao, Y. Suzuki, Y. Kuroda, T. Asakawa, and T. Kanemura, 2015, Rev. Sci. Instrum. **86**, 033905.
Sakano, M., *et al.*, 2013, Phys. Rev. Lett. **110**, 107204.
Sakata, M., Y. Nakamoto, K. Shimizu, T. Matsuoka, and Y. Ohishi, 2011, Phys. Rev B **83**, 220512.
Santoro, M., J.-F. Lin, H. K. Mao, and R. J. Hemley, 2004, J. Chem. Phys. **121**, 2780–2787.
Sarrao, J. L., L. A. Morales, J. D. Thompson, B. L. Scott, G. R. Stewart, F. Wastin, J. Rebizant, P. Boulet, E. Colineau, and G. H. Lander, 2002, Nature (London) **420**, 297–299.
Schilling, J. S., 2006, in *High-Temperature Superconductivity: A Treatise on Theory and Applications*, edited by J. R. Schrieffer (Springer-Verlag, Berlin).
Schülke, W., 2007, *Electron Dynamics by Inelastic X-Ray Scattering* (Oxford University Press, New York).
Sefat, A. S., 2011, Rep. Prog. Phys. **74**, 124502.
Seo, S., V. A. Sidorov, H. Lee, D. Jang, Z. Fisk, J. D. Thompson, and T. Park, 2012, Phys. Rev. B **85**, 205145.
Seo, S., *et al.*, 2014, Nat. Phys. **10**, 120–125.
Shahar, A., E. A. Schauble, R. Caracas, A. E. Gleason, M. M. Reagan, Y. Xiao, J. Shu, and W. Mao, 2016, Science **352**, 580–582.
Sharma, S. K., H. K. Mao, and P. M. Bell, 1980, Phys. Rev. Lett. **44**, 886–888.
Shen, G., and H. K. Mao, 2017, Rep. Prog. Phys. **80**, 016101.
Shen, G., M. L. Rivers, Y. Wang, and S. R. Sutton, 2001, Rev. Sci. Instrum. **72**, 1273–1282.
Shen, G., L. Wang, R. Ferry, H. K. Mao, and R. J. Hemley, 2010, J. Phys. Conf. Ser. **215**, 012191.
Shen, Y. R., T. Gregorian, and W. B. Holzapfel, 1991, High Press. Res. **7**, 73–75.
Sheng, H. W., H. Z. Liu, Y. Q. Cheng, J. Wen, P. L. Lee, W. K. Luo, S. D. Shastri, and E. Ma, 2007, Nat. Mater. **6**, 192–197.
Shi, C. Y., L. Zhang, W. Yang, Y. Liu, J. Wang, Y. Meng, J. C. Andrews, and W. L. Mao, 2013, Nat. Geosci. **6**, 971–975.
Shimizu, H., and S. Sasaki, 1992, Science **257**, 514–516.
Shimizu, K., H. Ishikawa, D. Takao, T. Yagi, and K. Amaya, 2002, Nature (London) **419**, 597–599.

Shimizu, K., T. Kimura, S. Furomoto, K. Takeda, K. Kontani, and K. Amaya, 2001, Nature (London) **412**, 316–318.
Shimizu, K., K. Suhara, M. Ikumo, M. I. Eremets, and K. Amaya, 1998, Nature (London) **393**, 767–769.
Shimizu, Y., M. Maesato, and G. Saito, 2011, J. Phys. Soc. Jpn. **80**, 074702.
Shishido, H., R. Settai, H. Harima, and Y. Onuki, 2005, J. Phys. Soc. Jpn. **74**, 1103–1106.
Shishido, H., *et al.*, 2010, Phys. Rev. Lett. **104**, 057008.
Sieburger, R., P. Müller, and J. S. Schilling, 1991, Physica C (Amsterdam) **181**, 335–339.
Silvera, I. and R. Dias, 2017, Science **357**, eaan2671.
Sinogeikin, S. V., J. S. Smith, E. Rod, C. Lin, C. Kenney-Benson, and G. Shen, 2015, Rev. Sci. Instrum. **86**, 072209.
Sipos, B., A. F. Kusmartseva, A. Akrap, H. Berger, L. Forro, and E. Tutis, 2008, Nat. Mater. **7**, 960–965.
Smith, J. S., S. V. Sinogeikin, C. Lin, E. Rod, L. Bai, and G. Shen, 2015, Rev. Sci. Instrum. **86**, 072208.
Soignard, E., C. J. Benmore, and J. L. Yarger, 2010, Rev. Sci. Instrum. **81**, 035110.
Solli, D., and R. Jeanloz, 2001, Rev. Sci. Instrum. **72**, 2110–2113.
Somayazulu, M., P. Dera, A. F. Goncharov, S. A. Gramsch, P. Liermann, W. Yang, Z. Liu, H. K. Mao, and R. J. Hemley, 2010, Nat. Chem. **2**, 50–53.
Somayazulu, M. S., L. W. Finger, R. J. Hemley, and H. K. Mao, 1996, Science **271**, 1400–1402.
Somoano, R. B., and A. Rembaum, 1971, Phys. Rev. Lett. **27**, 402–404.
Sørensen, H. O., *et al.*, 2012, Z. Kristallogr. **227**, 63–78.
Sparn, G., J. D. Thompson, S.-M. Huang, R. B. Kaner, F. Diederich, R. L. Whetten, G. Gruner, and K. Holezer, 1991, Science **252**, 1829.
Spetzler, H., A. Shen, G. Chen, G. Herrmannsdoerfer, H. Schulze, and R. Weigel, 1996, Phys. Earth Planet. Inter. **98**, 93–97.
Speziale, S., H. Marquardt, and T. S. Duffy, 2014, in *Brillouin Scattering and its Application in Geosciences*, edited by G. S. Henderson, D. R. Neuville, and R. T. Downs (Mineralogical Society of America, Chantilly, VA), pp. 543–603.
Steglich, F., J. Aarts, C. D. Bredl, W. Lieke, D. Meschede, W. Franz, and H. Schäfer, 1979, Phys. Rev. Lett. **43**, 1892–1896.
Stewart, G., 2001, Rev. Mod. Phys. **73**, 797–885.
Stewart, G., 2006, Rev. Mod. Phys. **78**, 743–746.
Stewart, G. R., 2011, Rev. Mod. Phys. **83**, 1589–1596.
Stixrude, L., and R. Jeanloz, 2008, Proc. Natl. Acad. Sci. U.S.A. **105**, 11071–11075.
Strobel, T. A., X. J. Chen, M. Somayazulu, and R. J. Hemley, 2010, J. Chem. Phys. **133**, 164512.
Strobel, T. A., M. Somayazulu, and R. J. Hemley, 2009, Phys. Rev. Lett. **103**, 065701.
Struzhkin, V. V., M. I. Eremets, W. Gan, H. K. Mao, and R. J. Hemley, 2002, Science **298**, 1213–1215.
Struzhkin, V. V., A. F. Goncharov, R. J. Hemley, and H. K. Mao, 1997, Phys. Rev. Lett. **78**, 4446–4449.
Struzhkin, V. V., R. J. Hemley, H. K. Mao, and Y. A. Timofeev, 1997, Nature (London) **390**, 382–384.
Struzhkin, V. V., D. Y. Kim, E. Stavrou, T. Muramatsu, Ho Kwang Mao, C. J. Pickard, R. J. Needs, V. B. Prakapenka, and A. F. Goncharov, 2016, Nat. Commun. **7**, 12267.
Struzhkin, V. V., H. K. Mao, J.-F. Lin, R. J. Hemley, J. S. Tse, Y. Ma, M. Y. Hu, P. Chow, and C.-C. Kao, 2006, Phys. Rev. Lett. **96**, 137402.
Suderow, H., V. G. Tissen, J. P. Brison, J. L. Martınez, and S. Vieira, 2005, Phys. Rev. Lett. **95**, 117006.
Sun, L., *et al.*, 2012, Nature (London) **483**, 67–69.
Sundqvist, B., 1999, Adv. Phys. **48**, 1–134.
Swamy, V., A. Kuznetsov, L. S. Dubrovinsky, P. F. McMillan, V. B. Prakapenka, G. Shen, and B. C. Muddle, 2006, Phys. Rev. Lett. **96**, 135702.
Syassen, K., 2008, High Press. Res. **28**, 75–126.
Tafti, F. F., A. Juneau-Fectea, M. E. Delage, S. R. d. Cotret, J. P. Reid, A. F. Wang, X. G. Luo, X. H. Chen, N. Doiron-Leyraud, and L. Taillefer, 2013, Nat. Phys. **9**, 349–352.
Takabayashi, Y., *et al.*, 2009, Science **323**, 1585–1590.
Takahashi, H., K. Igawa, K. Arii, Y. Kamihara, M. Hirano, and H. Hosono, 2008, Nature (London) **453**, 376–378.
Taniguchi, H., M. Miyashita, K. Uchiyama, K. Satoh, N. Mori, H. Okamoto, K. Miyagawa, K. Kanoda, M. Hedo, and Y. Uwatoko, 2003, J. Phys. Soc. Jpn. **72**, 468–471.
Tanino, H., 1986, Rev. Sci. Instrum. **57**, 2992–2994.
Tateiwa, N., and Y. Haga, 2009, Rev. Sci. Instrum. **80**, 123901.
Tateno, S., K. Hirose, Y. Ohishi, and Y. Tatsumi, 2010, Science **330**, 359–361.
Taufour, V., *et al.*, 2014, Phys. Rev. B **89**, 220509(R).
Tian, Y., *et al.*, 2013, Nature (London) **493**, 385–388.
Timofeev, Y. A., V. V. Struzhkin, R. J. Hemley, H. K. Mao, and E. A. Gregoyanz, 2002, Rev. Sci. Instrum. **73**, 371–377.
Tissen, V. G., M. R. Osorio, J. P. Brison, N. M. Nemes, M. Garcıa-Hernandez, L. Cario, P. Rodiere, S. Vieira, and H. Suderow, 2013, Phys. Rev. B **87**, 134502.
Tkachev, S. N., M. H. Manghnani, and Q. Williams, 2005, Phys. Rev. Lett. **95**, 057402.
Troyan, I., A. Gavriliuk, R. Rüffer, A. Chumakov, A. Mironovich, I. Lyubutin, D. Perekalin, A. P. Drozdov, and M. I. Eremets, 2016, Science **351**, 1303–1306.
Tse, J. S., Y. Yao, and K. Tanaka, 2007, Phys. Rev. Lett. **98**, 117004.
Uwatoko, Y., S. Todo, K. Ueda, A. Uchida, M. Kosaka, Nobuo Mori, and T. Matsumoto, 2002, J. Phys. Condens. Matter **14**, 11291–11296.
Vankó, G., J. P. Rueff, A. Mattila, Z. Németh, and A. Shukla, 2006, Phys. Rev. B **73**, 024424.
van Veenendaal, M., 2015, *The Theory of Inelastic Scattering and Absorption of X-rays* (Cambridge University Press, Cambridge, United Kingdom).
Vilaplana, R., *et al.*, 2011, Phys. Rev. B **84**, 184110.
Vogt, T., J. A. Hriljac, N. C. Hyatt, and P. Woodward, 2003, Phys. Rev. B **67**, 140401(R).
von Löhneysen, H., T. Pietrus, G. Portisch, H. G. Schlager, A. Schroeder, M. Sieck, and T. Trappmann, 1994, Phys. Rev. Lett. **72**, 3262–3266.
von Löhneysen, H., A. Rosch, M. Vojta, and P. Wolfe, 2007, Rev. Mod. Phys. **79**, 1015–1075.
Vos, W. L., and J. A. Schouten, 1991, J. Appl. Phys. **69**, 6744–6746.
Wang, D., and A. Fernandez-Martinez, 2012, Science **337**, 812–813.
Wang, K., *et al.*, 2009, Langmuir **25**, 4787–4791.
Wang, L., Y. Ding, W. Yang, W. Liu, Z. Cai, J. Kung, J. Shu, R. J. Hemley, W. L. Mao, and H. K. Mao, 2010, Proc. Natl. Acad. Sci. U.S.A. **107**, 6140–6145.
Wang, L., B. Liu, H. Li, W. Yang, Y. Ding, S. V. Sinogeikin, Y. Meng, Z. Liu, X. C. Zeng, and W. L. Mao, 2012, Science **337**, 825–828.
Wang, L. *et al.*, 2010, Phys. Rev. Lett. **105**, 095701.
Wang, Q. S. *et al.*, 2016, Nat. Mater. **15**, 159–163.
Wang, R. S., Y. Gao, Z. B. Huang, and X. J. Chen, 2017, arXiv:1703.05803, arXiv:1703.05804, arXiv:1703.06641.
Wang, S. B., *et al.*, 2014, Phys. Rev. B **89**, 024515.
Wang, X. F., R. H. Liu, Z. Gui, Y. L. Xie, Y. J. Yan, J. J. Ying, X. G. Luo, and X. H. Chen, 2011, Nat. Commun. **2**, 507.

Wang, Y., H. Liu, J. Lv, L. Zhu, H. Wang, and Y. Ma, 2011, Nat. Commun. **2**, 563.
Weir, S. T., D. D. Jackson, S. Falabella, G. Samudrala, and Y. K. Vohra, 2009, Rev. Sci. Instrum. **80**, 013905.
Weir, S. T., A. C. Mitchaell, and W. J. Nellis, 1996, Phys. Rev. Lett. **76**, 1860–1870.
Wenk, H. R., S. Matthies, R. J. Hemley, H. K. Mao, and J. Shu, 2000, Nature (London) **405**, 1044–1047.
Wigner, E., and H. B. Huntington, 1935, J. Chem. Phys. **3**, 764–770.
Willers, T., *et al.*, 2015, Proc. Natl. Acad. Sci. U.S.A. **112**, 2384–2388.
Wilson, J. A., F. J. Di Salvo, and S. Mahajan, 1975, Adv. Phys. **24**, 117–120.
Wortmann, G., U. Ponkratz, B. Bielemeier, and K. Rupprecht, 2008, High Press. Res. **28**, 545.
Wu, J., and P. R. Buseck, 2013, Nat. Geosci. **6**, 875–878.
Wu, J. J., J. F. Lin, X. C. Wang, Q. Q. Liu, J. L. Zhu, Y. M. Xiao, P. Chow, and C. Jin, 2013, Proc. Natl. Acad. Sci. U.S.A. **110**, 17263–17266.
Xia, Y., *et al.*, 2009, Nat. Phys. **5**, 398–402.
Yagi, T., T. Suzuki, and S. Akimoto, 1985, J. Geophys. Res. **90**, 8784–8788.
Yang, W., X. Huang, R. Harder, J. N. Clark, I. K. Robinson, and H. K. Mao, 2013, Nat. Commun. **4**, 1680.
Ye, J. T., Y. J. Zhang, R. Akashi, M. S. Bahramy, R. Arita, and Y. Iwasa, 2012, Science **338**, 1193.
Ying, J. J., V. V. Struzhkin, Z. Y. Cao, A. F. Goncharov, H. K. Mao, F. Chen, X. H. Chen, A. G. Gavriliuk, and X. J. Chen, 2016, Phys. Rev. B **93**, 100504(R).
Yoo, C. S., *et al.*, 2005, Phys. Rev. Lett. **94**, 115502.
Young, A. F., C. Sanloup, E. Gregoryanz, S. Scandolo, R. J. Hemley, and H. K. Mao, 2006, Phys. Rev. Lett. **96**, 155501.
Yu, Z., L. Wang, Q. Hu, J. Zhao, S. Yan, K. Yang, S. Sinogeikin, G. Gu, and H. K. Mao, 2015, Sci. Rep. **5**, 15939.
Yuan, H. Q., F. M. Grosche, M. Deppe, C. Geibel, G. Sparn, and F. Steglich, 2003, Science **302**, 2104–2107.
Yuan, H. Q., F. M. Grosche, M. Deppe, G. Sparn, C. Geibel, and F. Steglich, 2006, Phys. Rev. Lett. **96**, 047008.
Zaghoo, M., A. Salamat, and I. F. Silvera, 2016, Phys. Rev. B **93**, 155128.
Zaleski-Ejgierd, P., R. Hoffmann, and N. W. Ashcroft, 2011, Phys. Rev. Lett. **107**, 037002.
Zeidler, A., *et al.*, 2014, Phys. Rev. Lett. **113**, 135501.
Zeng, Q., Y. Ding, W. L. Mao, W. Yang, S. V. Sinogeikin, J. Shu, H. K. Mao, and J. Z. Jiang, 2010, Phys. Rev. Lett. **104**, 105702.
Zeng, Q., H. Sheng, Y. Ding, L. Wang, W. Yang, J. Z. Jiang, W. L. Mao, and H. K. Mao, 2011, Science **332**, 1404–1406.
Zeng, Q., *et al.*, 2009, Proc. Natl. Acad. Sci. U.S.A. **106**, 2515–2518.
Zeng, Q., *et al.*, 2014, Phys. Rev. Lett. **112**, 185502.
Zeng, Q., *et al.*, 2016, Proc. Natl. Acad. Sci. U.S.A. **113**, 1714–1718.
Zha, C. S., and W. A. Bassett, 2003, Rev. Sci. Instrum. **74**, 1255–1262.
Zha, C. S., R. E. Cohen, H. K. Mao, and R. J. Hemley, 2014, Proc. Natl. Acad. Sci. U.S.A. **111**, 4792–4797.
Zha, C. S., H. Y. Liu, J. Tse, and R. J. Hemley, 2017, Phys. Rev. Lett. **119**, 075302.
Zha, C. S., Z. Liu, and R. J. Hemley, 2012, Phys. Rev. Lett. **108**, 146402.
Zha, C. S., H. K. Mao, and R. J. Hemley, 2000, Proc. Natl. Acad. Sci. U.S.A. **97**, 13494–13499.
Zha, C. S., K. Mibe, W. A. Bassett, O. Tschauner, H.-K. Mao, and R. J. Hemley, 2008, J. Appl. Phys. **103**, 054908.
Zhang, J. B., V. V. Struzhkin, W. G. Yang, H. K. Mao, H. Q. Lin, Y. C. Ma, N. L. Wang, and X. J. Chen, 2015, J. Phys. Condens. Matter **27**, 445701.
Zhang, J. L., *et al.*, 2011, Proc. Natl. Acad. Sci. U.S.A. **108**, 24–28.
Zhang, L., Y. Meng, P. Dera, W. Yang, W. L. Mao, and H. K. Mao, 2013, Proc. Natl. Acad. Sci. U.S.A. **110**, 6292–6295.
Zhang, L., *et al.*, 2014, Science **344**, 877–882.
Zhang, W., A. R. Oganov, A. F. Goncharov, Q. Zhu, S. E. Boulfelfel, A. O. Lyakhov, E. Stavrou, M. Somayazulu, V. B. Prakapenka, and Z. Konôpková, 2013, Science **342**, 1502–1505.
Zhao, Z. Y., O. Khosravani, M. Lee, L. Balicas, X. F. Sun, J. G. Cheng, J. Brooks, H. D. Zhou, and E. S. Choi, 2015, Phys. Rev. B **91**, 161106.
Zhong, G. H., C. Zhang, X. J. Chen, Y. L. Li, R. Q. Zhang, and H. Q. Lin, 2012, J. Phys. Chem. C **116**, 5225–5234.
Zhou, J. S., J. A. Alonso, A. Muoñz, M. T. Fernández-Díaz, and J. B. Goodenough, 2011, Phys. Rev. Lett. **106**, 057201.
Zhu, J., *et al.*, 2013, Sci. Rep. **3**, 2016.
Zhuravlev, K. K., A. F. Goncharov, S. N. Tkachev, P. Dera, and V. B. Prakapenka, 2013, J. Appl. Phys. **113**, 113503.
Zou, G. T., Y. Z. Ma, H. K. Mao, R. J. Hemley, and S. Gramsch, 2001, Rev. Sci. Instrum. **72**, 1298–1301.
Zurek, J., R. Hoffmann, N. W. Ashcroft, A. R. Oganov, and A. O. Lyakhov, 2009, Proc. Natl. Acad. Sci. U.S.A. **106**, 17640–17643.